Universitat Autònoma de Barcelona

UAB

Universitat Autònoma de Barcelona

PhD Thesis

Intracellular Silicon Chips

Rodrigo Gómez Martínez

_____

Under the supervision of:

Dr. José Antonio Plaza Plaza

with Co-supervision of:

Dr. Jaume Esteve Tinto

University Tutor:

Dr. Francesc Serra Graells

PhD Program in Electrical and Telecommunication Engineering

Department of Microelectronics and Electronic Systems - School of Engineering

2016

CONSEJO SUPERIOR DE INVESTIGACIONES CIENTÍFICAS

Report submitted to aspire to the Doctor degree by:

Rodrigo Gómez Martínez

Checked and accepted by:

Dr. Jaume Esteve Tinto   Dr. Francesc Serra Graells

Thesis Co-Supervisor   University Tutor

Dr. José Antonio Plaza Plaza

Thesis Supervisor

Intracellular Silicon Chips

PhD Thesis

Doctorat en Enginyeria Electrònica i de Telecomunicació

Departament de Microelectrònica i Sistemes Electrònics

Universitat Autònoma de Barcelona

Barcelona, Cerdanyola del Vallès. September 13, 2016

A mis padres, hermanos, tías, tíos, abuelas y abuelos

A Pau, Martina y Carme

"Der Tod ist kein Ereignis des Lebens. Den Tod erlebt man nicht.
Wenn man unter Ewigkeit nicht unendliche Zeitdauer, sondern Urzeitlichkeit versteht, dann lebt der ewig,
der in der Gegenwart lebt.
Unser Leben ist ebenso endlos, wie unser Gesichtsfeld grenzenlos ist."
Ludwig Wittgenstein
(Logisch-Philosophische Abhandlung, 1921)

"Qué bueno sentarse en uno de estos cafés de verano, al aire libre, en calles y plazas! Mesitas colocadas
en un espacio separado por arbustos. Pedir un café y encender un cigarrillo colombiano. Pero es preciso
sentarse solo o con un amigo o amiga que no hable sino de vez en cuando. No es que la soledad sea lo
mejor, pues somos sociables, sino que hay poca gente digna de que por ella se cambie la soledad. Se
necesita una persona cuya corriente nerviosa fluya sin vibraciones, continua e igual. Casi todos son
enervantes, casi todos somos desarreglados."
Fernando González
(El hermafrodita dormido, 1933)

Acknowledgements

List of Acronyms

1D	One dimension
2D	Two dimensions
3D	Three dimensions
ACT	Atomic camera tamer
AFM	Atomic force microscopy
ANOVA	Analysis of variance
AOBS	Acousto-optical beam splitter
AOTF	Acousto-optical tunable filter
APO	Apochromatic
BFOM	Bright field optical microscope
Bit	Binary digit
CCD	Charge-coupled device
CFDA	Fluorescein Diacetate
CLSM	Confocal laser scanning microscopy
CVD	Chemical vapor deposition
D	Rigidity of the plate
DAPI	4, 6-diamidino-2-phenylindole
DiOC	Dihexyloxacarbocyanine iodide
Displ $_{memb}$	Displacement of the membrane
DMEM	Dulbecco´s modified eagle medium
DMF	Dimethylformamide
DNA	Deoxyribonucleic acid
DRIE	Deep reactive ion etching
E	Young´s modulus
EAA1	Anti-Early endosome antigen
ECACC	European collection of cell cultures
EEA	Early endosome antigen
ELWD	Extra-long working distance
F	Force
FBS	Fetal bovine serum
FEA	Finite element analysis
FEM	Finite element method
FIB	Focused ion beam
FP	Fabry-Pérot
FS	Full scale
GFP	Green fluorescent protein
GMbH	Gesellschaft mit beschränkter Haftung
HF	Hydrofluoric acid
H-KSOM	Hepes Potassium-supplemented simplex optimized medium
ICC	Intracellular silicon chips
ICP	Inductively coupled plasma

$I_{r\ Border}$	Intensity of the reflected light at the border of the membrane
$I_{r\ Centre}$	Intensity of reflected light at the centre of the membrane
$I_{r\ Ref}$	Intensity of reflected light from the reference area at the chip
$I_{r\ Sensor}$	Intensity of the reflected light at sensor after the mathematical process
LAS AF	Leica application suite advanced fluorescence
LPCVD	Low-pressure chemical vapor deposition
LU	Luminous Universal
MEMS	MicroElectroMechanical Systems
MPs	Microparticles
MTT	Dimethyl Thiazolyl Diphenyl Tetrazolium salt
NEMS	NanoElectroMechanical Systems
NOMS	NanoOptoMechanical Systems
P	Pressure
PBS	Phosphate-buffered saline
PECVD	Plasma enhanced chemical vapor deposition
PI	Propidium iodide
PMA	Phorbol 12-myristate 13-acetate
polySi	Polysilicon
PTFE	Polytetrafluoroethylene
PVDF	Polyvinylidene fluoride
RIE	Reactive ion etching
ROI	Region of interest
rpm	Revolutions per minute
RT	Room temperature
SCCM	Standard cubic centimeters per minute
SEM	Scanning electron microscopy
Si	Silicon
SOI	Silicon on insulator
t_{gap}	Gap distance
t_{memb}	Membrane thickness
TCS	True confocal scanning
TEM	Transmission electron microscopy
UV	Ultraviolet
WGA	Wheat Germ Agglutinin
λ	Wavelength
ν	Poisson's ratio

Contents

Abstract

Intracellular silicon chips are defined as devices small enough to be internalized inside single living cells for future applications in life science, where silicon based micro- and nanotechnologies have been used to achieve this purpose. This thesis is focused in the development of four different challenges, from passive chips (microparticles and barcodes) to biochemical and pressure sensors, as a proof of concept. All these prototypes present different shapes, sizes, and materials. Standard photolithographic and silicon based technologies, which allow the obtaining of devices with lateral dimensions within the micro- and nanoscale, to be internalized easily by one cell or ever by a population of cells, are tuned up.

This work addresses specific objectives where the design, technological development, characterization and biological validation as intracellular chips inside living cells are described. The first demonstrators show dummy intracellular chips and intracellular barcodes for single cell labeling and tracking, a passive device, where the design, technological development, characterization and biological validation are described. Technological capabilities of the definition of patterned chips are applied to obtain the Intracellular Barcodes code design. Furthermore, the chemical functionalization concept is applied to our intracellular devices, enabling a new line of applications for biochemical recognition. Finally, and going one step forward, and with the main objective of achieving even more functional Intracellular chips, the design, technological development, characterization and validation of an intracellular pressure sensor inside a single cell is described. Being this device the first silicon-based NanoOptoMechanical System (NOMS) inside a living cell. Summarizing, the extensive capabilities of the presented Intracellular Silicon Chips imply a broad number of applications in cell biology, such as cell labeling and tracking, and sophisticated intracellular cell sensing.

Objectives

<u>Main objective</u>

> The main objective of this PhD thesis has been to develop intracellular chips small enough to be internalized inside single living cells for future applications in life science, where silicon based micro- and nanotechnologies have been used to achieve this objective.

With this purpose four different devices, from passive chips (microparticles and barcodes) to biochemical sensors and pressure sensors, were proposed as a proof of concept. All these prototypes were based on standard photolithographic and silicon based technologies, which allow the obtaining of devices with lateral dimensions within the micro- and nanoscale.

<u>Specific objectives</u>

The specific objectives of this work include:

1. To design of Intracellular Chips below the typical cell scales with several patterns, dimensions and materials.

2. To develop technological processes for the fabrication of Intracellular Chips at wafer level combining different silicon-based technologies.

3. To develop the releasing and collecting techniques for the obtaining of Intracellular Chips.

4. To physically characterize of the Intracellular Chips through several techniques.

5. To validate of the Intracellular Chips for advanced applications in cell biology.

A list of the proposed devices is shown:

1. Dummy Intracellular chips for living cell applications.

2. Intracellular Polysilicon Barcodes for single cell labeling.

3. Intracellular Polysilicon Chips for biomolecular recognition.

4. Intracellular NanoOptoMechanical Systems

Structure of the thesis

This doctoral thesis has been organized in three main parts:

The first one includes the **Thesis Presentation** and **Chapter 1: General Introduction** describing the state of the art in advances related to micro- and nanodevices for cell biology applications.

The second one, the heart of this work, is divided into 4 chapters each one for each of the specific devices developed in the frame of this thesis. The structure of these four main chapters is an extended version of the following scientific publications of the author [1] [2] [3] [4] [5].

- **Chapter 2** presents the first Intracellular Chip, a dummy chip, developed by our Micro- and NanoTools group for applications in cell biology, where the design, technological development, characterization and biological validation as an intracellular chip inside living cells are described. [1]

- With the main objective of applying the preliminary results of the Intracellular Chips described in chapter 2 and taking advantage of the technological capabilities related to the definition of patterned chips, **Chapter 3** describes the design, technological development, characterization and biological validation of Intracellular Barcodes (as passive devices) for single cell labelling and tracking. [2] [3]

• The incorporation of the chemical functionalization concept to our intracellular devices, allowed us to open a new line of applications, for instance biochemical recognition. The proof of concept of these devices is presented in **Chapter 4**, where the design, technological development, and validation of polySilicon devices, as biochemically functionalized Intracellular ensors for future biomolecular sensing and actuation, are described. [4]

• Furthermore, and going one step forward, and with the main objective of achieving even more sophisticated and functional Intracellular Chips, **Chapter 5** describes the design, technological development, characterization and validation of a intracellular pressure sensor (IPS) inside a single cell, being the first silicon-based NanoOptoMechanical sensor (NOMS) inside a living cell. [5]

Finally, the third main part includes the **General Conclusions** and the **Future Work**.

Bibliography

[1] Elisabet Fernández-Rosas, Rodrigo Gómez-Martínez, Elena Ibañez, Leonardo Barrios, Marta Duch, Jaume Esteve, José Antonio Plaza, Carme Nogués. *Internalization and cytotoxicity analysis of silicon-based microparticles in macrophages and embryos*. Biomedical Microdevices, 12, 3, 371 (2010). DOI: 10.1007/s10544-009-9393-6.

[2] Rodrigo Gómez-Martínez, Ana Sánchez, Marta Duch, José Antonio Plaza. *DRIE based technology for 3D silicon barcodes fabrication*. Sensor and Actuators B, 1, 1, 800 (2011).

[3] Elisabet Fernández-Rosas, Rodrigo Gómez-Martínez, Elena Ibáñez, Leonardo Barrios, Marta Duch, Jaume Esteve, Carme Nogués, José Antonio Plaza, *Intracellular polysilicon barcodes for cell tracking*. Small, 5, 21, 2433 (2009).

[4] Rodrigo Gómez-Martínez, Patricia Vázquez, Marta Duch, Alejandro Muriano, Daniel Pinacho, Nuria Sanvicens, Francisco Sánchez-Baeza, Patricia Boya, Enrique J. de la Rosa,

Jaume Esteve, Teresa Suarez, José Antonio Plaza. *Intracellular silicon chips in living cells*. Small, 6, 4, 499 (2010).

[5] Rodrigo Gómez-Martínez, Alberto M. Hernández-Pinto, Marta Duch, Patricia Vázquez; Kirill Zinoviev, Enrique J. de la Rosa, Jaume Esteve, Teresa Suarez, José Antonio Plaza. *Silicon chips detect intracellular pressure changes in living cells*. Nature Nanotechnology, 8, 517 (2013).

Chapter 1

General Introduction:

Microfabricated technologies for Cell Biology

1. 1. Introduction

1.2. Emerging tools for intracellular measurements

 1.2.1 Emerging tools with physical connections to extracellular instruments

 1.2.2 Emerging tools without physical connections to extracellular instruments

1.3. Scope of the thesis

 1.3.1 Preliminary works with Intracellular Chips for living cell applications

 1.3.2 Intracellular polySilicon Barcodes for single cell labeling

 1.3.3 Intracellular polySilicon Chips for biomolecular recognition

 1.3.4 NanoOptoMechanical Systems inside living cells

Bibliography

1.1 Introduction

Due to the aim of this thesis, the applications of intracellular chips explained along all sections will be focused on how microtechnology meets cell biology. The interest for the small world has been a constant in physics, biology and engineering, as the cell, as the smallest alive unit is the core of all of them. Interpreted in a reductionist way, a cell is a compartment in which a collection of chemical reactions occur, and it is those reactions that we call life [1]. The area of cell biology explains numerous biological processes and biochemical reactions within a living cell, an those are often compartmentalized and can dynamically change physical and chemical properties, for instance, temperature [2-3], pressure [4], cell mechanics [5], intracell electrical characteristics [6], pH [7], and concentrations of ions and other molecules [8]. The field of microfabrication technology originated from the semiconductor industry has a great impact on life sciences. Monitoring intracellular environments and quantitatively measuring intracellular properties will achieve future advanced applications and open new research lines. In addition, miniaturization technologies and the material science in the micro- and nanometer range [9-10] are of great interest to the electronic engineers in particular and the scientific community in general. Recently, microfabrication technology has gained popularity in the biology field due to the real need of small devices with a precise geometry or topography. The miniature device structure (the definition of 'miniature' depends on the application, but can range from 1 nm to 1 mm) is well matched to the physical dimension of most organisms at cellular dimension. Many of these devices are based on silicon technologies, as these technologies are constantly growing, they allow to achieve high reproducibility of the devices, high versatility features, and can also offer biocompatibility. Several studies are focused on micron-scales tools, which make possible to manipulate individual cells, their shape, internal organization and their extracellular and

intracellular environment. Intrinsic electrical, mechanical and chemical properties of silicon and silicon-based materials make them highly suitable to be used in microsensors. The capability of intracellular devices to sense or operate in living cells resides in the fact that they can be internalized easily by one cell or ever by a population of cells (Figure. 1.1)
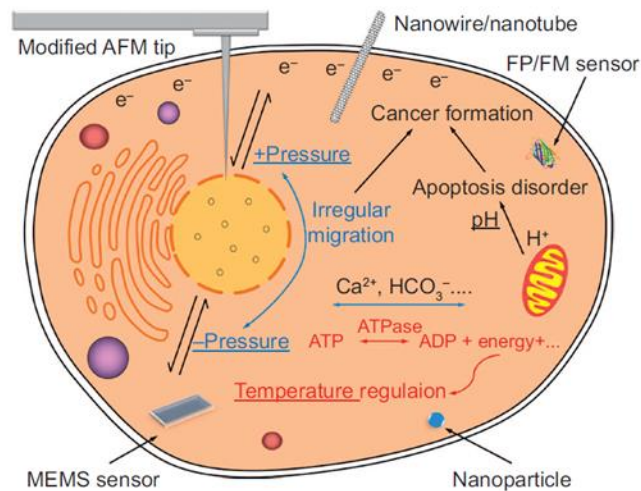
Figure 1.1: Microfabricated technologies meet Cell Biology. Schematic showing representative intracellular properties and the miniature devices for intracellular measurements (Reproduced with permission from Reference [10]).

Since the potential of this field, the following section gives a brief overview of several emerging tools for intracellular measurements.

1.2 Emerging tools for intracellular measurements

Microsystems technology is an attractive and exciting field that has played and very important role in building a bridge between sciences and nowadays society. In the past century, several technologies were developed to study cell biology parameters such as chemical, physics and biological properties. The field continues evolving towards the development of more sophisticated methods and tools to measure intracellular properties and manipulate subcellular structures. In addition, due to the even smaller dimensions of intracellular targets (from nano- to microdimensions), the development of suitable tools for intracellular measurements and manipulation is a challenging idea (Figure. 1.2).
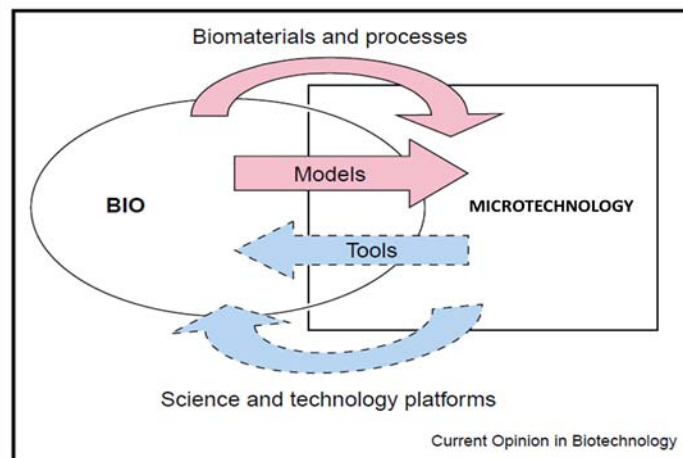
Figure 1.2: Schematic of the interactions between a biology and microtechnology fields (Adapted and reproduced with permission from Reference [11]).

Within their environment, cells are subjected to multiple cues that vary in time and space, and depend on organisms' health and vital state. Microfabricated systems can give these cells the

same cues but in a controllable and reproducible way and can be used to integrate cells to analytical tools that can help to understand the biochemical processes that govern cell behavior.

From the point of view of intracellular manipulation techniques, emerging tools can be classified in two groups, devices that perform intracellular measurements a) with and b) without physical connections to extracellular instruments.

1.2.1 Emerging tools with physical connections to extracellular instruments

The first group refers to, for instance electrical characterizations devices, which include chip-based patch clamping devices.

It consists of planar insulating diaphragms made of silicon and have the objective of replace traditional patch electrodes for a planar array of miniaturized recording interfaces on the surface of either silicon, polymer or glass substrate. Chips with multiple recording sites can be produced and integrated in large quantity with well-defined geometry and material properties due to the standard silicon technology [12]. A microsystem with de capability to perform a whole-cell patch clamping, is also reported (Figure 1.3a) [13]. Cell electrical properties can also be measured using carbon nanotubes (CNT). CTN present intrinsic advantages in the measurement of electrical properties since they are made with silicon based materials and their size is small enough to directly sense properties like intracellular potential and pH (Figure 1.3b-c) [14-15]. Similarly, arrays of vertical nanowires for parallel intracellular recording have been gaining attention and interest, due to their high throughput for electrical measurements in long-term cell cultures (Figure 1.3d) [16].

a   b

c   d
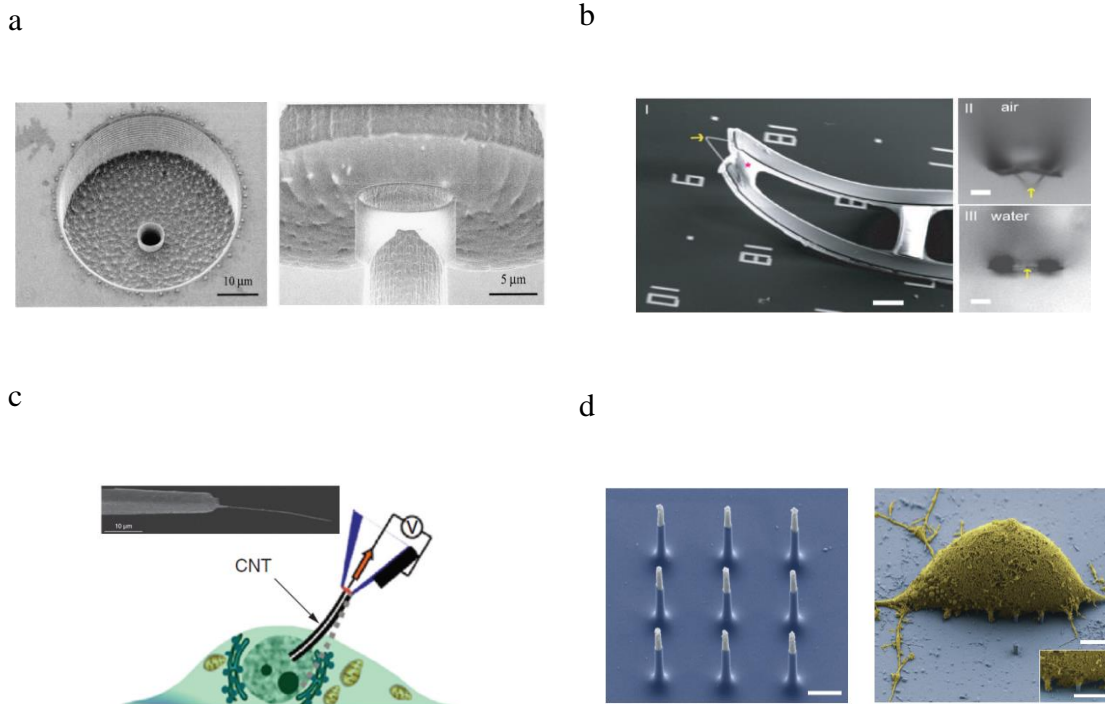
Figure 1.3: Chip-base patch clamp, carbon nanotubes and nanowires for intracellular measurements. a) Micronozzles for electrical measurements (Reproduced with permission from Reference [13]). b) A silicon nanowire forms a 3D FET device for direct measurements of intracellular potentials (Reproduced with permission from Reference [14]). c) Carbon nanotube endoscope (Reproduced with permission from Reference [15]). d) Vertical electrode arrays based on silicon nanowires for electrical measurements (Reproduced with permission from reference [16]).

Nowadays, more systematic studies of deformation, structural dynamics and mechanochemical transduction in living cells and biomolecules are needed to gauge the different cellular conditions. The different states of cells (normal and diseased) are dependent on or are regulated by their mechanical environment, thus the deformation characteristics can provide important

information about its biological and structural functions. Cells in viable tissues respond to mechanical stimuli under physiological and pathophysiological conditions, changing cell geometry and configuration. These changes are caused by alterations in the activity of ion channels, and the concentrations of signaling molecules, which ultimately lead to modifications of the cytoskeleton and extracellular structures [17-18].

Microsystems technology offers the ability to fabricate devices of a comparable size to a single cell (25 μm – 250 μm), that will allow the application of both static and dynamic mechanical stimulus [19]. It is well known that many MEMS (MicroElecroMechanical Systems) consist of mechanical and electrical parts, the first one can be deformed or is able to move when a force is applied, and the second one transduces this deformation or movement into an electrical signal. MEMS devices are mainly fabricated with silicon-based materials, and have been widely applied for measuring the mechanical properties of a single cell or a whole population of cells (Figure 1.4) [20].

a
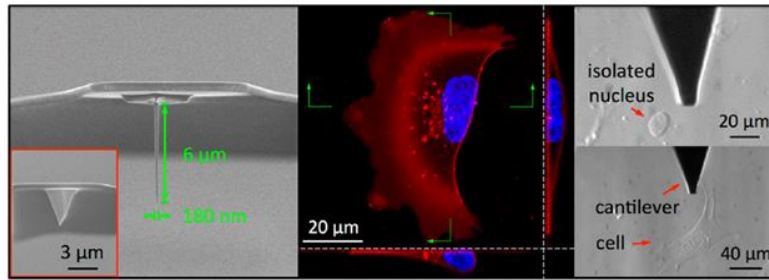
b
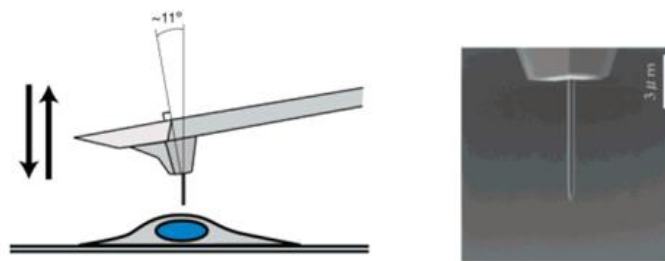
Figure 1.4: Modified standard Atomic force Microscopy (AFM) cantilever for intracellular applications. a) AFM tip for penetrations inside a single cell to measure the mechanical properties of a cell nucleus (Adapted with permission from Reference [25] Copyright 2014). b) Schematic and a scanning electronic image of a nanoneedle structure on the AFM tip for living cells applications (Adapted with permission from Reference [27]).

Their small size and fine force/displacement resolution enable us to use MEMS to measure both force and displacement within cells. Typical MEMS are fabricated with several individual devices, used to simultaneously monitoring the behavior of many cells [21], to apply specific forces [22], or to monitor *in vivo* small forces [23]. Similarly, microsystems technology enables the modification of standard AFM cantilever probes, where the conical or pyramidal tip can be

applied against a cell surface allowing the observation of elastic and viscoelastic properties of a

single cell (Figure 1.5) [26-31].

a   b   c
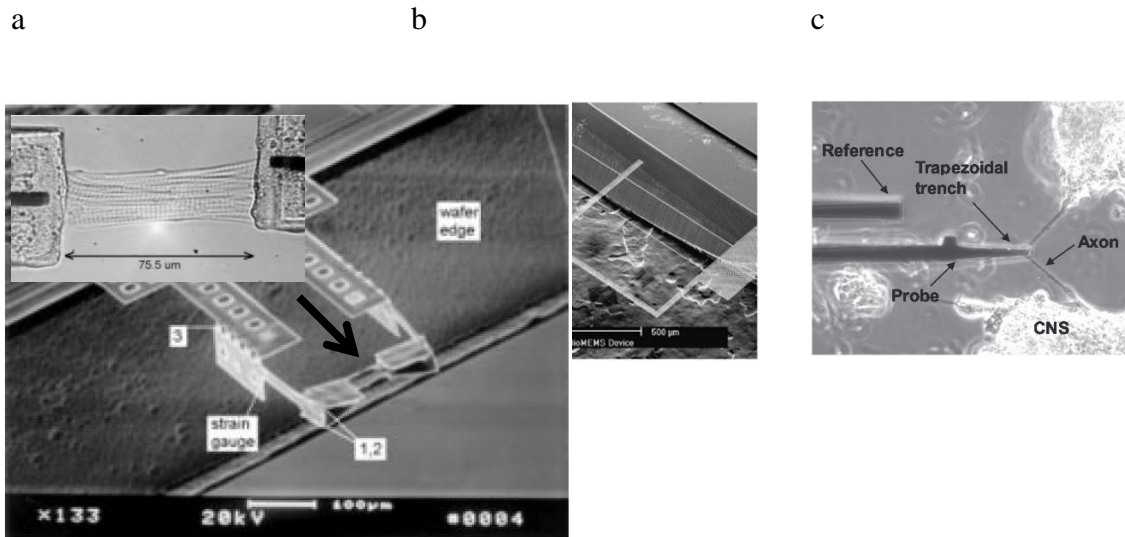
IEEE copyright line © 2001 IEEE

c
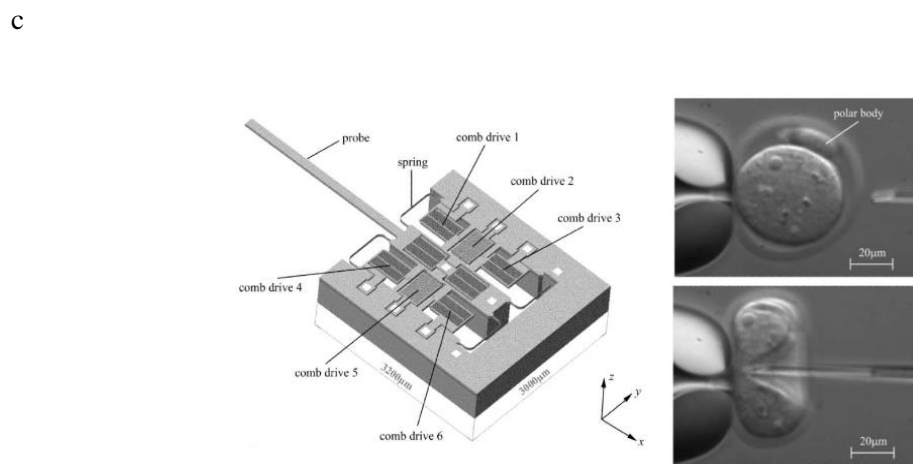
**Figure 1.5: Miniature transducers (MEMs) for intracellular force measurement
applications**. a) Miniature heart cell force transducer system (Reproduced with
permission from reference [19]). b) MEMS force sensors designed to study the
indentation response of single living cells (Reproduced with permission from Reference
[22]). c) MEMS to study regular axonal tension *in vivo* (Reproduced with permission

from Reference [23]). d) Comb-drive actuator used for mechanical characterization (Reproduced with permission from Reference [24], IEEE copyright line © 2003 IEEE).

In the same way, devices to external an internal single cell communication, such as silicon-based nanochannels at submicrometer dimensions, have been reported. Hence, those channels could be used, for example, to perform useful single-molecule experiments or to withdraw samples from the cells [32]. Similarly, microscopic networks of phospholipid bilayer CNTs and containers are reported [33]. This type of networks enables model systems to study confined biochemical reactions, intracellular transport phenomena and chemical computations. For instance, nanopipette microsystems enable the localized injection of different kind of chemicals compounds into the different areas inside the cells. The combination of nanochannels with an electrochemical actuation allow researchers to control flow rates down to the subpicoliter per second range, which in turn would allow precise drug dosing into a single cell (Figure 1.6) [34-35].

a   b
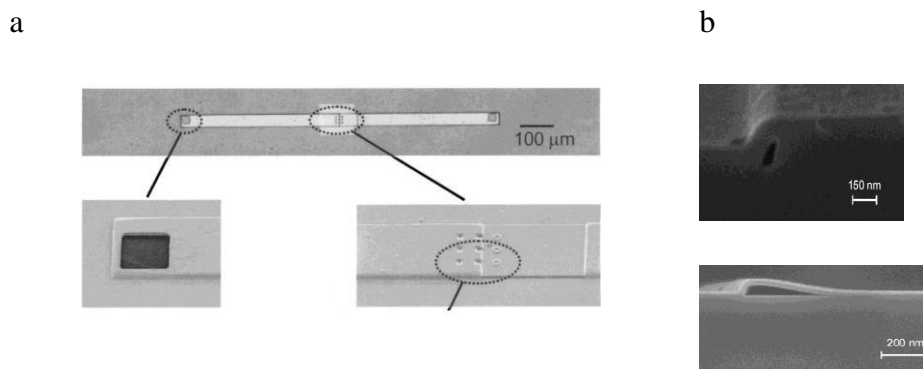
Figure 1.6: Nanopipettes and nanochannels for intracellular applications. a) Optical microscope image of a fabricated pump (Reproduced with permission from Reference [34], Copyright (2002) American Chemical Society). b) Two-dimensional confined nanochannels (Reproduced with permission from Reference [35]).

1.2.2 Emerging tools without physical connections to extracellular instruments

The second group of emerging tools includes devices for intracellular measurements without any kind of physical connection to an extracellular instrument [36]. These tools are reported as nanoparticles. Their minimally disturbance at intracellular activities make them high suitable for long-term intracellular measurements. Recently, the application of nanoparticles has been significantly extended, as they can be easily coupled to sensitive fluorophores. Nanoparticle intracellular sensors include polymeric nanoparticles [37], silica nanoparticles [38], nanodiamonds [39], gold nanoparticles [40], silicon nanoparticles [41] and quantum dots [42]. Nowadays, intracellular nanoparticle sensing is mainly based on fluorescence spectroscopy and in addition, nanoparticles fluorescence can be either intrinsically or conjugated with sensitive fluorescent dyes for sensing [43]. Furthermore, the use of several kinds of nanoparticles (such as polymeric and gold nanoparticles, nanodiamons and quantum dots) has been applied to measure the intracellular temperature [44-49]. Similarly, the combined of these nanoparticles, with different types of fluorophores has also been extended to chemically sense intracellular chemical properties, such as pH, oxygen concentration, and ion concentration [50-55].

b
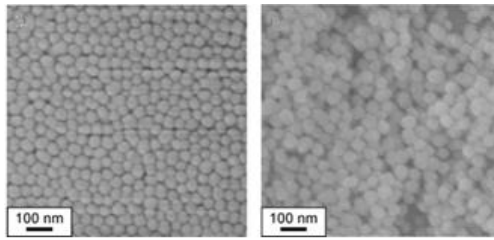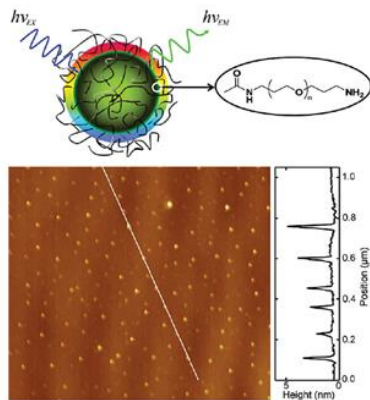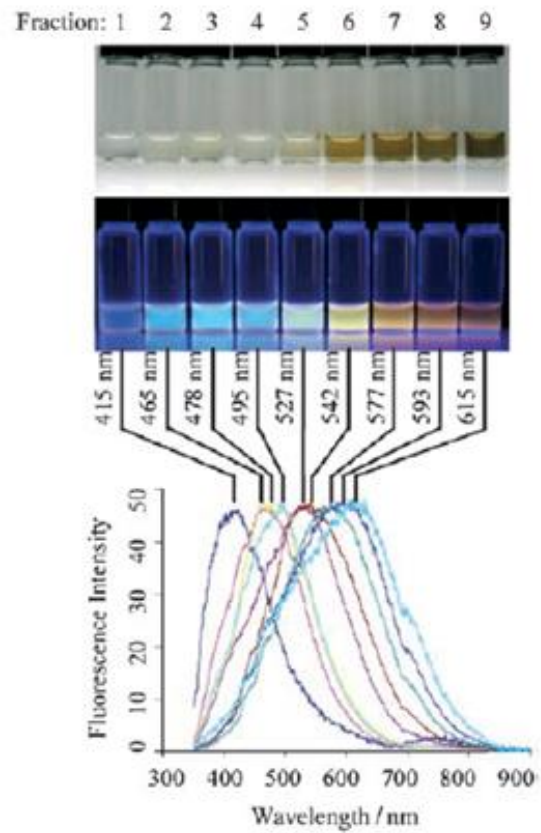
Figure 1.7: Nanoparticles for intracellular measurements. a) Core/shell fluorescent silica nanoparticles for intracellular chemical sensing (Reproduced with permission from Reference [44]). b) Fluorescent carbon nanoparticles (Reproduced with permission from Reference [48]). c) Fluorescents carbon dots (Reproduced with permission from Reference [49]).

1.3 Scope of the thesis

Along this chapter a summary of several applications of micro- and nanoparticles and micro- and nanosystems, at cell scale, for intracellular applications have been presented. The overall goal of this thesis has been to push the forefront of the field by designing and fine tuning the technological fabrication process, to develop and open new lines of Micro- and NanoTools to perform measurements inside single cells. The steps forward are listed below and will be further developed in the upcoming chapters.

1.3.1 Preliminary works with Intracellular Chips for living cell applications

Silicon-based Intracellular Chips (ICCs), produced taking advantage of the MEMS fabrication technologies, are presented at Chapter 2. These devices with a high controlled shape and size, high versatility and mass production are small enough to be internalized inside living cells. The design and the fabrication process of these intracellular chips, completely manufactured using silicon (Si) or polysilicon (polySi) materials, are presented. Once they are manufactured, the steps to reach an efficient release and manipulation are also reported. Finally, to determine whether these ICCs can be successfully internalized inside living cells, without affecting their viability, biological techniques to analyze cell viability and cytotoxicity in Human Macrophages are studied.

1.3.2 Intracellular Polysilicon Barcodes for single cell labeling

Emerging 2D and 3D barcodes, using silicon-based material, are reported. In addition, a fabrication technology based on photolithographic processes and deep reactive ion etching (DRIE) techniques are fine-tuned at Chapter 3. These techniques allow us to obtain micrometer-size 2D rectangular cuboid structures and 3D cylindrical-like barcode structures with binary codifications as readout technique method. Although these technologies could achieve several bits representations, only 4-8 bits are proposed. Finally, the high versatility of photolithographic and DRIE processes to produce biocompatible silicon-based barcode structures for living cell applications are demonstrated.

1.3.3 Intracellular Polysilicon Chips for biomolecular recognition

In order to open new perspectives on biomolecular recognition, the ability to produce bio-functionalized silicon-based intracellular chips (ICCs) with dimensions under the 3 μm is explored in Chapter 4. Once they are manufactured, the different steps to reach an efficient chip collection, manipulation and cell internalization, are shown. The capability of these intracellular chips to be used as biomolecular sensors is demonstrated by their application in the detection of intracellular esterases. In order to illustrate the biomolecular potential of ICC, *Dictyostelium Discoideum* (Dicty) and Human *HeLa* cellular models, are chosen to be tested with these newly developed techniques. Furthermore, chapter 4 also demonstrates that small chips can be produced with a range of materials. Additionally, they can be nanostructured through the integration of electronic and mechanical parts at ICC-scale level.

1.3.4 NanoOptoMechanical Systems inside living cells

In Chapter 5 an intracellular device for measuring mechanical properties inside a single cell, is reported. The main purpose of this developed device is to go one step forward and propose a new emerging tool to perform a mechanical pressure measurement inside single cells. Silicon-base devices are fabricated with two membranes separated by a vacuum gap and an optical reference area. Once they are internalized into a cell, the intracellular pressure change deflects the device membrane, which changes the gap size and alters the intensity of reflected light at the center of the membrane. The optical reference area is used for focusing purposes. The experimental data measured by this NanoOptoMechanical pressure sensor confirm that extracellular pressure is transmitted through the cytosol to the inner compartments, proving that the intracellular transmission of fluid pressure follows the Pascal's law. In conclusion, it is shown that MEMS can be internalized into a single cell to perform intracellular pressure measurements.

Bibliography

[1] A. Eschenmoser, M. V. Kisakurek. Chemistry and the origin of life. Helv. Chim. Acta 79, 1249 (1996)

[2] D. Patel, K. A. Franklin. Plant Signaling & Behavior 4, 577 (2009)

[3] B. B. Lowell, B. M. Spiegelman. Nature 404, 652 (2000)

[4] H. Jiang, S. X. Sun. Biophysical Journal 105, 609 (2013)

[5] D-H Kim, P. K. Wong, J. Park. Annual Review of Biomedical Engineering 11, 203 (2009)

[6] W. Moody. Annual Review of Neuroscience 7, 257 (1984)

[7] W. J. Waddell, R. G. Bates. Physiological Reviews 49, 285 (1969)

[8] T. Kinashi. Nature Reviews Immunology 5, 546 (2005)

[9] G. M. Whitesides. Nature Biotechnology 21, 1161 (2003)

[10] J. Liu, J. Wen, Z. Zhang, H. Liu, Y. Sun. Microsystems & Nanoengineering 1, 15020 (2015)

[11] M. C. Roco. Current Opinion in Biotechnology 14, 337 (2003)

[12] C. Schmidt, M. Mayer, H. Vogel. Angew. Chem. Int. 39, 3137 (2000)

[13] T. Lehnert, M. A. M Gijs, R. Netzer, U. Bischoff. Appl. Phys. Lett. 81, 24 (2002)

[14] B. Tian, T. Cohen-Karni, Q. Qing. Science 329, 830 (2010)

[15] Y. Gao, T. Longenbach, E. A. Vitol, Z. Orynbayeva, G. Friedman, Y. Gogotsi. Nanomedicine 9, 153 (2014)

[16] J. T. Robinson, M. Jorgolli, A. K. Shalek, M-H Yoon, R. S. Gertner, H. Park. Nature Nanotechnology 7, 180 (2012)

[17] T. Brown. J. Biomech. 33, 3 (2000)

[18] G. Bao, S. Suresh. Nature Materials 2, 715 (2003)

[19] G. Lin, R. Palmer, K. Pister, K. Roos. IEEE Trans Biomed. Eng. 48, 996 (2001)

[20] J. Rajagopalan, M. Taher A. Saif. J. Micromech. Microeng. 21 5, 054002 (2011)

[21] D. Kim, K. W. Pak, J. Park, A. Levchenko, Y. Sun. Annu. Rev. Biomed. Eng. 11, 203 (2009)

[22] S. Yang, M. T. A. Saif. Sens. Actuators, A. 135 1, 16 (2007)

[23] J. Rajagopalan, A. Tofangchi, M. T. A. Saif. Biophysical Journal. 99, 3208 (2010)

[24] Y. Sun, K. T. Wan, K. P. Roberts, J. C. Bischof, B. J. Nelson. IEEE Trans. Nanobiosci. 2 4, 279 (2003)

[25] H. Liu, J. Wen, Y. Xiao, J. Liu, S. Hopyan, M. Radisic, C. A. Simmons, Y. Sun. ACS Nano 8, 3821 (2014)

[26] K. Yum, N. Wang, M-F Yu. Nanoscale 2, 363 (2010)

[27] I. Obataya, C. Nakamura, S. Woong, N. Nakamura, J. Miyake. Nano Letters 5 1, 27 (2005)

[28] A. B. Mathur, A. M. Collinsworth, W. M. Reichert, W. E. Kraus, G. A. Truskey. Journal of Biomechanics 34, 1545 (2001)

[29] D. Desmaële, M. Boukallel, S. Régnier. Journal of Biomechanics 44, 1433 (2011)

[30] T. G. Kuznetsova, M. N. Starodubtseva, N. I. Yegorenkov, S. A. Chizhik, R. I. Zhdanov. Micron 38, 824 (2007)

[31] A. Alessandrini, P. Facci. Meas. Sci. Technol. 16, R65 (2005)

[32] N. R. Tas, J. W. Berenschot, P. Mela, H.V. Jansen, M. Elwenspoek, A. van den Berg. Nano Lett., 2, 1031 (2002)

[33] A. Karlsson, R. Karlsson, M. Karlsson, A. Cans, A. Strömberg, F. Ryttsen, O. Orwar. Nature 409, 150 (2001)

[34] H. Andersson, A. van den Berg. Current Opinion in Biotechnology 15, 44 (2004)

[35] N. Tas, J. Berenschot, T. Lammerink, M. Elwenspoek, A. van den Berg. Anal. Chem. 74, 2224 (2002)

[36] J. Liu, J. Wen, Z. Zhang, H. Liu, Y. Sun. Microsystems & Nanoengineering 1, 15020 (2015)

[37] E. Schmälzlin, J. T. van Dongen, I. Klimant, B. Marmodée, M. Steup, J. Fisahn, P. Geigenberger, H-G. Löhmannsröben. Biophys. J. 89, 1339 (2005)

[38] H. Shi, X. He, K. Wang, Y. Yuan, K. Deng, J. Chen, W. Tan. Nanomed. Nanotechnol. Biol. Med. 3, 266 (2007)

[39] S. N. Baker, G. A. Baker. Angew. Chem. Int. Ed. Engl.49, 6726 (2010)

[40] H. Y. Lee, H. Son, J. M. Lim, J. Oh, D. Kang, W. S. Han, J. H. Jung. Analyst 135 8, 20227 (2010)

[41] J. H. Warner, A. Hoshino, K. Yamamoto, R. D. Tilley. Angew. Chem. Int. Ed. 44, 4550 (2005)

[42] Y-S. Liu, Y. Sun, P. T. Vernier, C-H. Liang, S. Y. C. Chong, M. A. Gundersen. J. Phys. Chem. C 111, 2872 (2007)

[43] M. J. Ruedas-Rama, J. D. Walters, Angel Ort, E. A. H. Hall. Analytica Chimica Acta 751, 1 (2012)

[44] A. Schulza, C. McDonagh. Soft Matter. 8, 2579 (2012)

[45] C. Gota, S. Uchiyama, T. Ohwada. . Analyst 132, 121 (2007)

[46] L. Haipeng, T. Ye, C. Mao. Angew. Chem. Int. Ed., 46, 6473 (2007)

[47] L. Martínez-Maestro, E. Martín-Rodríguez, F. Sanz-Rodríguez, M. C. Iglesias-de la Cruz, A. Juarranz, R. Naccache, F. Vetrone, D. Jaque, J. A. Capobianco, and J. García S. Nano Lett., 10, 5109 (2010)

[48] S. Wang, S. Westcott, W. Chen, J. Phys. Chem. B, 106, 11203 (2002)

[49] G. Kucsko, P. C. Maurer, N. Y. Yao, M. Kubo, H. J. Noh, P. K. Lo, H. Park, M. D. Lukin. Nature, 500 1 54 (2013)

[50] A. Burns, P. Sengupta, T. Zedayko, B. Baird, U. Wiesner. Small, 2 6 723 (2006)

[51] D. Si, T. Epstein, Y-EK Lee. Analytical Chemistry, 84 978 (2012)

[52] S. Seo, H. Y. Lee, M. Park, J. M. Lim, D. Kang, J. Yoon, J. H. Jung. European Journal of Inorganic Chemistry, 843 (2010)

[53] K. Sarkar, K. Dhara, M. Nandi, P. Roy, A. Bhaumik. Advanced Functional Materials 19, 223 (2009)

[54] S-T Yang, X. Wang, H. Wang, F. Lu, P. G. Luo, L. Cao, M. J. Meziani, J-H Liu, Y. Liu, M. Chen, Y. Huang, Y-P Sun, J. Phys. Chem. 113, 18110 (2009)

[55] H. Liu, T. Ye, and C. Mao. Angew. Chem. Int. Ed., 46, 6473 (2007)

Chapter 2

Preliminary works with Intracellular Chips for living cell applications

2.1 Abstract

2.2 Introduction

2.3 Concept

2.4 Preliminary design of Intracellular Chips

      2.4.1 PolySilicon-based Chips

      2.4.2 Silicon-based Chips

2.5 Wafer layout for the fabrication of dummy Intracellular Chips

2.6 Technology development for the fabrication of dummy Intracellular Chips at wafer level

      2.6.1 Fabrication technology of polySilicon-based Chips

      2.6.2 Fabrication technology of Silicon-based Chips

2.7 Technology development for the release and collection of dummy Intracellular Chips

      2.7.1 Release of Intracellular Chips

      2.7.2 Collection of Intracellular Chips

2.8 Physical characterization of dummy Intracellular Chips

2.9 Intracellular Chips in living Human Macrophages

    2.9.1 Cellular uptake by phagocytosis

    2.9.2 Cell viability and cytotoxicity assays

2.10 Discussion and Conclusions

Bibliography

2.1 Abstract

In the near future, microtechnology will be able to produce microchips small enough to be introduced inside living cells and sense or modify specific intracellular parameters at a single cell level. Although such microchips are not yet available, the technology necessary to produce them is already developed; in fact, nowadays micron- and submicron scale sophisticated structures can be precisely mass-produced through the semiconductor technologies.

In this chapter, silicon-based Intracellular Chips (ICCs), produced taking advantage of the MicroElectroMechanical Systems fabrication technologies, are developed. These devices present controlled shape and size, high versatility and mass production, in addition, they are small enough to be internalized inside living cells. The design and the fabrication process of these intracellular chips, completely manufacture using silicon (Si) or polySilicon (polySi) material, is also developed. Once they are manufactured, the steps to reach an efficient release and manipulation are carried out. Finally, to determine whether these ICCs can be successfully internalized by living cells, without affecting their viability, biological techniques to analyze cell viability and cytotoxicity in Human Macrophages are tested.

The results of this work show a well-controlled fabrication and collection procedures and the potential capabilities of the presented Intracellular Chips for future applications in cell biology.

2.2 Introduction

A range of strategies and technologies has been used to analyze the morphology, biochemistry, genetics and physiology of specific cells or tissues [1-9]. Nevertheless, MEMS have been also used to study living cells [10, 11], the weighing of a single cell [12], cell manipulation and positioning [13, 14] or molecular recognition [15, 16].

On the other hand, nano- and microparticles present huge opportunities for developing new strategies to many scientific challenges. For instance, micrometer-sized biocompatible and biodegradable mesoporous silicon devices have been used as multi-stage delivery systems for endothelial cells, where the devices, for instance, can release their cargo [17, 18]. So far, particles on both nano- and microsize ranges, and made of different materials have been successfully introduced into various cell types. In most studies, cells with an inherent phagocytic capacity, such as macrophages and dendritic cells [19, 20] are analyzed, but in many others, cells that are not specialized in phagocytosis, such as *HeLa* cells, have also demonstrated that they are able to internalize different kind of particles [21, 22]. It is also worth mentioning that the presence of gold [21], polystyrene [23-26], poly(lactic-co-glycolic acid (PLGA) [27, 28] or mesoporous silica [19] particles did not affect cell viability. In addition, the size of the particles must also be taken into consideration, as nanoparticles (NPs) seem to be more toxic than microparticles (MPs) [29].

The methods used for obtaining chemical particles, for instance the bottom up techniques, come from small components to obtain a high number of particles of mainly of spherical shape [31]. Except some concrete examples, for instance polyhedralor rod shapes have been obtained [31-33]. This chemical technique allows defining the final size of the particles, restricting to fabricate more sophisticated shapes. These particles are typically composed of a single material, limiting

their surface chemistry [34-37] (Figure 2.1a) and thus limiting the possibility to allow multiple functionalizations in the same particle.

Conversely, an ICC is a silicon-based chip completely manufactured using silicon (Si) or polySilicon (polySi) as structural material (Figure 2.1b). The big difference of the ICCs from particles chemically synthetized is that the ICCs employ techniques of microelectronics fabrication, taking advantage of the versatility of the photolithographic techniques, that enable the control of their dimensions and shapes. Accordingly, microelectronics technologies are highly suitable candidates for the fabrication of the ICCs, as they provide the possibility of growing or depositing many different materials, as semiconductors, insulations and metals with high precision, well-known surface chemistry and most of them biocompatible, in a single device. All these features enable a robust technology background, which can be used to produce devices for cell biology applications. Finally, for their use *in vivo*, ICCs should be effectively internalized into living cells and they should not compromise cell viability.
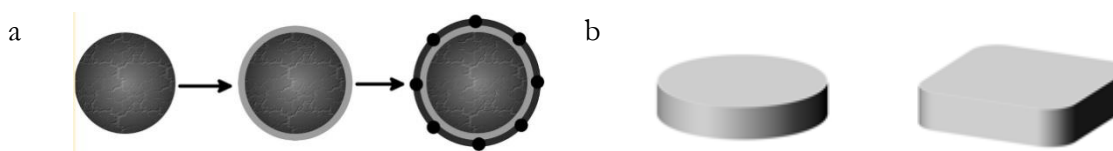

Figure 2.1: Particles chemically synthetized versus silicon-based Intracellular Chips. Schematic diagram of a) particles chemically synthetized typically with spherical shape (Reproduced with permission from Reference [29] Copyright 2011 American Chemical Society) and b) Intracellular Chips (ICCs) which shape can be defined by the designer.

2.3 Concept

In this chapter the technology for the fabrication and manipulation of silicon and polySilicon Intracellular Chips is reported. The vertical dimensions of these chips are defined with nanometric precision by the thickness of the device layer. Meanwhile, the photolithographic techniques define the micrometric or even sub-micrometric lateral dimensions. Silicon and polySilicon, common materials in MEMS industry, are selected as device materials because of their well-known physical, chemical and biocompatibility properties [38-42]. In addition, a silicon dioxide layer is selected as sacrificial layer to release the ICCs from the wafer, as this material is often used during the fabrication processes of microsensors and microactuators made of polycrystalline silicon as structural material [43]. Furthermore, in order to manipulate these ICCs the developed release and collection methods are described. Finally, the perspective of cell viability of these intracellular chips is also analyzed. Human macrophages are selected as a suitable cell line because of their natural capacity to engulf microparticles. This work has been done in partnership with the group of Dr. Carme Nogués of the *Department de Biologia Cel·lular, Fisiologia i Immunologia, Universitat Autònoma de Barcelona*.

2.4 Preliminary design of Intracellular Chips

2.4.1 PolySilicon-based Chips

First of all, a cylindrical polySilicon intracellular chip was developed in order to test if the fabrication process of small polySilicon devices was possible. The external dimensions were fixed to 3 µm-diameter and a 0.5 µm-thickness (Figure 2.2). These dimensions were chosen because the final ICCs should be small enough to be introduced into living cells but being still big to be easily visualized under an optical microscope.
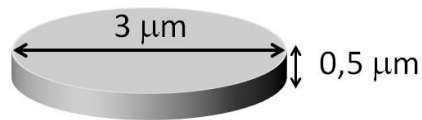
Figure 2.2: Conceptual representation of a polySilicon Intracellular Chip. Design and dimensions of a PolySilicon ICC.

2.4.2 Silicon-based Chips

Subsequently, rectangular cuboid and cylindrical silicon Intracellular Chips were design in order to test if the fabrication process of a small silicon device was possible. The external dimensions were fixed to 3 µm x 3 µm for the rectangular cuboid design and 3 µm of diameter for the cylindrical one, both with a 1.5 µm of thickness (Figure 2.3). These dimensions were chosen because the final ICCs should be small enough to be introduced into living cells.
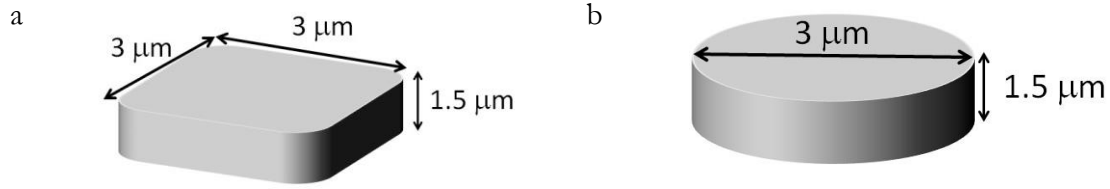
Figure 2.3: Conceptual representation of a silicon Intracellular Chip. Design and dimensions of a silicon ICC with a) rectangular cuboid shape and with b) cylindrical shape.

2.5 Wafer layout for the fabrication of dummy Intracellular Chips

Into the silicon microelectronic techniques, wafers are the initial substrates for the device fabrication and their dimensions limit the maximum number of devices that can be manufactured. For instance, for a 3 μm x 3 μm lateral-dimension device on pitch 3 μm distributed in a 10 cm-diameter wafer, more than 170 million of devices can be obtained with a chips/wafer density of 2.7 x 10^6 Chips/cm^2 (Figure 2.4).
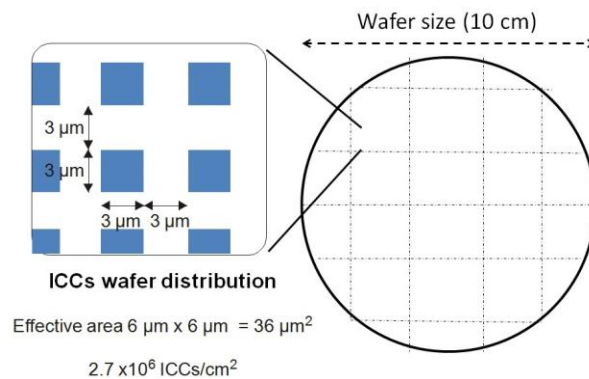

Figure 2.4: Distribution of Intracellular Chips at wafer level. Schematic representation of ICCs distribution on the wafer.

2.6 Technology development for the fabrication of the dummy Intracellular Chips at wafer level

2.6.1 Fabrication technology of polySilicon-based Chips

The fabrication technology of the polySilicon chips was based on the combination of two deposited layers, the device layer (polySilicon) and the sacrificial layer (silicon dioxide), on a silicon wafer. The polySilicon devices were obtained using a combination of a photolithographic process and a vertical dry etching to pattern the device layers.

Firstly, a 1 µm-thick silicon dioxide was deposited as a sacrificial layer by plasma enhanced chemical vapor deposition (PECVD) on a 100 mm-diameter silicon wafer (Figure 2.5a, b). Subsequently, a 500 nm-thick polySilicon layer was deposited (580 °C, 350 mTorr and a SiH_4 flow rate of 40 sccm) (Figure 2.5c). Next, a photolithographic step defined the photoresist pattern, fixing the area of the device (Figure 2.5d). Lastly, a polysilicon dry etching, using the photoresist as a mask, defined the chips (Figure 2.5e). As a result, an array of 3 µm x 3 µm devices on a pitch 3 µm was obtained. This approach yielded more than 170 million of controlled and reproducible devices per processed 100 mm-diameter silicon wafer.

Figure 2.5: Fabrication process of polySilicon-based Chips. a) Silicon substrate as starting material. b) A 1 µm-thick silicon dioxide is deposited as sacrificial layer. c) A 0.5 µm-thick LPCVD polySilicon layer is deposited as device layer. d) A 2 µm-thick photoresist layer was spun and exposed to fix the device area. e) The polySilicon layer was patterned by a dry etching process to define the chips and f) a 49% HF vapor etching was applied to release the chips from the wafer.

2.6.2 Fabrication technology of silicon-based Chips

The fabrication technology of the silicon Intracellular Chips was based on the combination of a device layer (silicon) and a sacrificial layer (silicon dioxide) on a Silicon-on-Insulator (SOI) wafer substrate. The term SOI refers to a silicon substrate with a single crystalline silicon device layer lying on a buried silicon oxide layer, which is set on top of a bulk silicon substrate. This structure is widely used in MEMS because it provides reliable electrical insulation, excellent etching stop and sacrificial layer functions. In addition, it increases the fabrication accuracy, process simplicity and device performance [44].

Thus, using a SOI wafer as a substrate (Figure 2.6a), a photolithographic step created a photoresist pattern, that fix the area of the device (Figure 2.6b). Subsequently, a polySilicon dry etching, using the photoresist as a mask, defined the devices (Figure 2.6c). As a result, an array of 3 μm x 3 μm chips on a pitch 3 μm was obtained. This approach yielded more than 170 million controlled and reproducible devices per processed 100 mm-diameter silicon wafer.
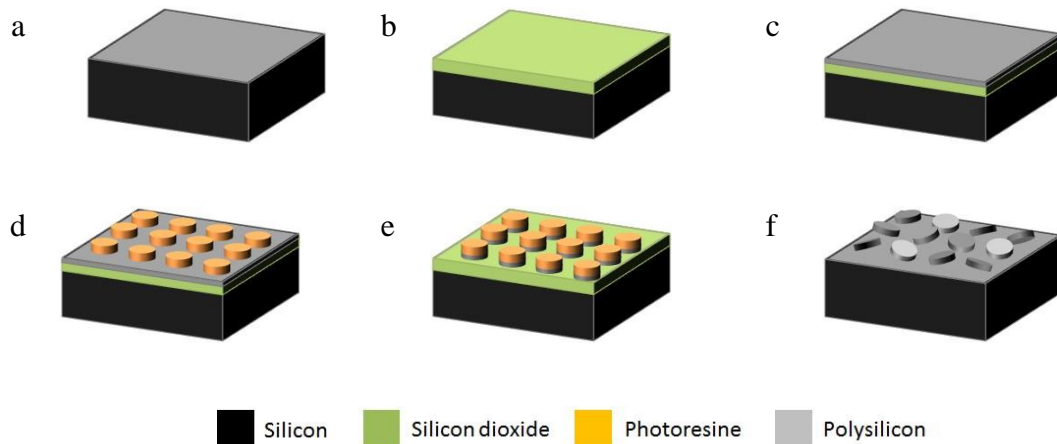

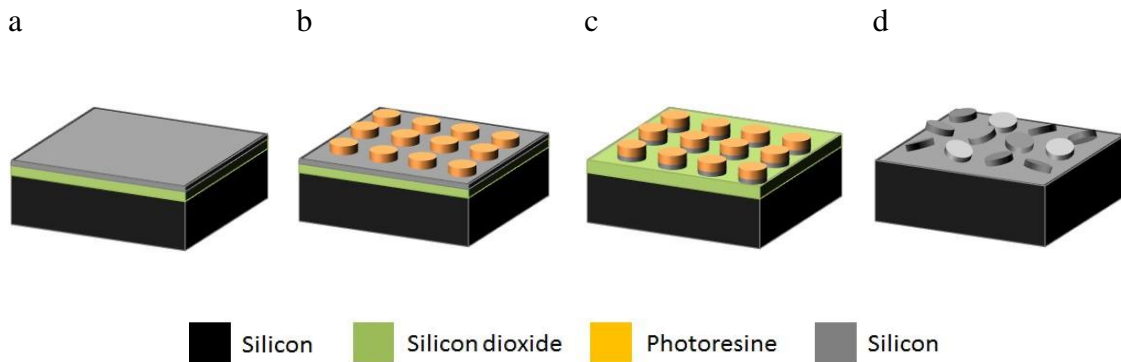**Figure 2.6: Fabrication process of silicon-based Chips**. a) Silicon-on-Insulator (SOI) substrate as starting material. b) A 2 μm-thick photoresist layer was spun and exposed to fix the device area. c) The silicon layer was patterned by a dry etching process to define the chips and, d) a 49% HF vapor etching was applied to release the chips from the wafer.

The used of SOI wafers avoid the deposition of a silicon oxide sacrificial layer and the deposition of the polySilicon layer. The main advantages are that the device layer is made of crystalline silicon, and the deposition of the sacrificial silicon oxide and polySilicon layers are avoided. The main disadvantages are that devices with different thickness required the acquisition of SOI wafer with different device layer thicknesses. In addition, SOI wafers are at less one order of

magnitude more expensive that standard silicon wafers used in the previous technologies, and in addition, it is hard to find a provider for 100 mm-diameter substrates.

2.7 Technology development for the release and collection of dummy Intracellular Chips

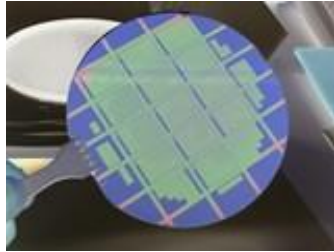## 2.7.1 Release of Intracellular Chips

It is widely known the use of sacrificial layers in microelectronics, as their etching mechanisms and their selectivity are common strategies in semiconductor fabrication processes [43]. In this regard, the use of different types of silicon dioxide layers as sacrificial material during the manufacture of MEMS devices is widely known. These types of SiO_2 can be divided into two main different alternatives, thermally grown silicon oxides (dry or wet) and deposited silicon oxides. In the case of thermal oxides, the bulk silicon is oxidized and in the case of deposited oxides, the layer is deposited on the wafer surface by a chemical reaction, for instance chemical vapor deposition (CVD).

The physical and chemical properties of silicon dioxide layers depend on the fabrication process. Long-term stability and chemical purity are crucial for dielectric layers used in integrated circuits, while high etch selectivity and high etching rates dominates the choice for sacrificial layer purposes. Etch selectivity against substrates, mechanical structure, high etch rate, high solubility of etch products to avoid residues, among others, are properties of SiO_2 for a suitable sacrificial layers when polySilicon is used as structural layer. Adsorption of reaction species on the surface, chemical and desorption of the reaction products, are also key steps related with the etch rate.

Silicon dioxide layers are usually dissolved by bases or acids. However, in our case, the bases are avoided because they also can etch the silicon substrates. Nevertheless, solutions containing hydrofluoric species are commonly used, due to their ability to break the bond Si-O [45]. The overall reaction is developed by the diffusion of the reactant concentration at the bulk surface, while the chemical reaction itself is taking place at the etch front. The selectivity of the etching solution is crucial for the physical properties of the structure, as it should be unaffected by the sacrificial layer etching. Currently, depending on the desired device, both wet etch solutions and sacrificial dioxide layers, are frequently used. The main disadvantage of these techniques lies in the sticking phenomenon occurring during rinse-drying step.

Sticking is produced due to capillary forces between two surfaces, unless the structure is stiff enough. A suitable solution to avoid the sticking phenomenon is using 49% HF vapors at a controlled temperature, instead of immersing the devices into the chemical solution [46]. This technique allows to reduce the formation of etch residues and water condensation, avoiding also the sticking phenomena while maintaining the advantages of wet etching techniques. Once the manufacturing process of the intracellular chips at wafer level was finished (Figures 2.5e, 2.6c and 2.7a), the wafer was divided into small pieces (1 cm x 1 cm) using a diamond tip (Figure 2.7b). Then, each wafer piece was placed in a Teflon holder, where it was subjected to 49% HF vapors for 40 minutes (Figure 2.7c). This vapor acid bath enabled the release of the ICCs from the wafer substrate, due to the wet etching of the silicon oxide layer (Figure 2.7d). At this stage, the released devices were attached to the silicon surface through surface tension forces.
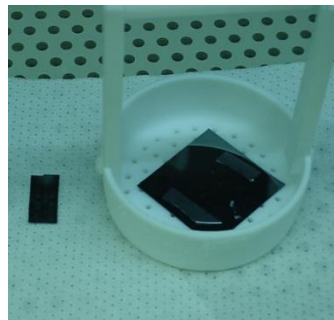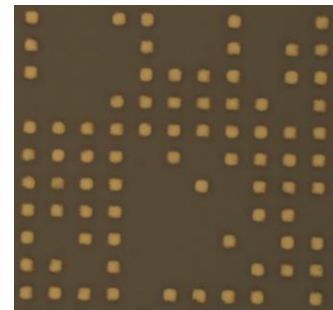
a b

c d

Figure 2.7: Release process of the Intracellular Chips from the silicon substrate. a) Intracellular chips on the wafer substrate. b) A cut of the wafer by a diamond tip. c) A piece of wafer and the Teflon holder allowing the vapor etching process. d) Optical image of the wafer piece with partially released chips.

2.7.2 Collection of Intracellular Chips

After the ICC 49% HF etching, the devices still laid attached to the silicon substrate. So, the next step was oriented to collect the ICCs in suspension. Firstly, the piece of wafer was immersed in a glass beaker, which contained a few milliliters of phosphate buffer solution (PBS). PBS was chosen due to its biocompatibility in biological applications. Then, the beaker was sonicated

(Figure 2.8a). After inspecting the sample on a dry surface, it was observed that the devices were attached to PBS residues and similarly, a large amount of ICCs were attached to the beaker.

A second attempt consisted in changing the glass beaker by a plastic one, and the PBS solution by a 96% ethanol solution. In this case, ethanol is not biocompatible, but allows maintaining the ICCs in a sterile environment. With this method, and after the sonicated step, the problems regarding the ICC aggregations and ICC remains inside the beaker were minimized.

Hence, the ICCs were suspended in ethanol, distributed in different Eppendorf's, which contained a filter to prevent silicon residues, and collected by centrifugation at 14000 rpm for 5 min. (Figure 2.8b). It is worth mentioning that ICCs collected in Eppendorf's can be stored until needed (Figure 2.8c). Nevertheless, before handling the ICCs the Eppendorf should be centrifuged again and the supernatant extracted, allowing the manipulation of the devices in microliter quantities using micropipettes.
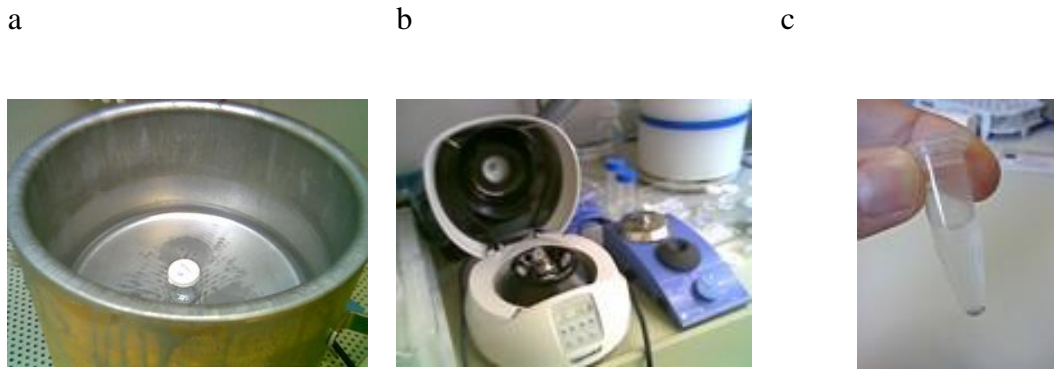
a   b   c

Figure 2.8: Setup for Intracellular Chips collection process. a) Sonication step to achieve the release of the ICCs from the silicon substrate. b) Centrifugation step which allows the obtaining of the ICC pellet. c) Millions of intracellular chips contained in a single Eppendorf's.

2.8 Physical characterization of dummy Intracellular Chips

SEM was chosen in order to physically characterize the obtained intracellular chips. In figure 2.9 can be observed the silicon and the polySilicon intracellular chips after the release method. The devices were perfectly performed and showed well-defined shapes and a perfectly vertical profile. After testing different shapes and dimensions, rectangular cuboid polySilicon ICCs with 3 µm x 3 µm dimensions and 0.5 µm thickness (4.5 µm^3) and cylindrical ICCs with 3 µm diameter and 1.5 µm thickness (10.60 µm^3) were selected for further studies (Figure 2.9 a, d). These dimensions were chosen because the obtained ICCs were small enough to be introduced into living cells but still big to be easily visualized under an optical microscope.
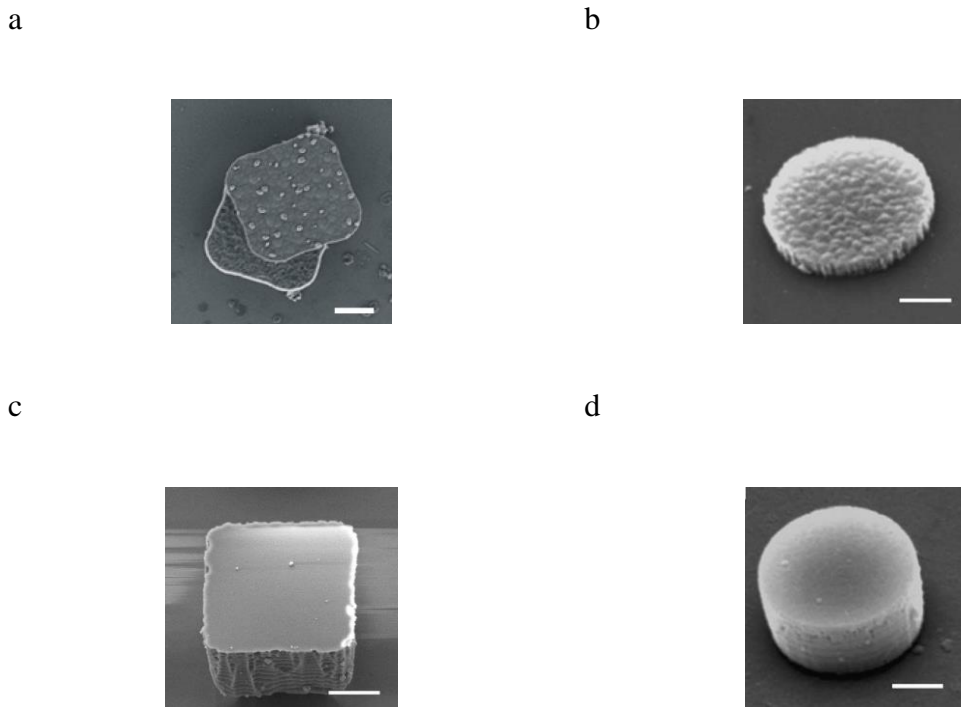
a   b

c   d

Figure 2.9: Fabrication results of Intracellular Chips. a) Rectangular cuboid polySilicon chips (3 µm x 3 µm x 0.5 µm). b) Cylindrical polySilicon chips (3 µm-diameter, 0.5 µm-thickness). c) Rectangular cuboid silicon chips (3 µm x 3 µm x 1.5 µm). d) Cylindrical silicon chips (3 µm-diameter, 1.5 µm-thickness). Scale bar = 1 µm.

2.9 Intracellular Chips in living Human Macrophages

The term of cell internalization or cell uptake can be defined as the process, technique or biological procedure used to introduce solid or liquid substances inside cells [47, 48].

Among the biological methods for introducing external material into cells, processes such as endocytosis, and procedures as micro-injection are found. *Endocytosis* is a cellular process by which cells internalize large molecules or particles, engulfing them into the plasma membrane forming a vesicle that is incorporated into the cytoplasm [49]. One of the endocytosis pathways are *phagocytosis*, and is the process by which, some cells - often phagocytes - have the ability to detect and engulf solid particles forming an internal vesicle known as a phagosome. *Microinjection* refers to the procedure, of using a glass micropipette to inject a liquid substance [50]. Another technique commonly used during cell internalization processes is *lipofection*, this is a technique used to internalize genetic material into a cell by liposomes, which are vesicles that can easily merge with the cell membrane since they are both made of a phospholipid bilayer [51].

As a proof of concept and with the main objective to determine whether silicon and polySilicon intracellular chips could be introduced inside the cells, the phagocytic capacity of Human Macrophages is shown along this chapter. Experiments were performed in partnership with the group of Dr. Carme Nogués of the *Department de Biologia Cel·lular, Fisiologia i Immunologia, Universitat Autònoma de Barcelona)*

2.9.1 Cellular uptake by phagocytosis

As it is mentioned in the last section, macrophages have an inherent phagocytic capacity and can engulf large pathogens and microparticles up to 20 μm [23]. However, not all types of materials can be phagocyted by these cells, and in some cases, it is needed to coat the microparticle surface with specific compounds before. In these studies bare polySilicon chips were added to the macrophage cultures at a ratio of 0.5 ICCs/cell. To visualize ICC internalization, different microscopy techniques after 24 h of the device addition were used.

Microscopy techniques provide the necessary tools to observe the studied cells. Techniques such as bright field inverted microscopy, scanning electron microscopy (SEM) or confocal laser scanning microscopy (CLSM) were used to analyze the internalization of different ICCs inside the cells. The inverted microscopy allows observing the biological condition of the cells, being able to identify if cells apparently interact with the devices. Nevertheless, with this technique it is not possible to discern whether the ICCs are, in fact, inside the cell. Scanning electron microscopy techniques offer the possibility of observing the outer structure of the cell, but not to analyze inside the cells. Currently, the confocal laser scanning microscopy techniques offer the possibility to analyze in detail the cell dynamics and structure, as this technique uses a kind of specific vital biomarkers linked to their corresponding fluorochromes to obtain information about the morphology, biochemistry, organelles or biomolecules of a specific cell. This technique not only gives biological cell information (depending on the biomarker type), but also it helps to discern any element of interest that could be present inside the cell, in addition, confirming whether the devices are outside or inside the cell.

Nowadays, techniques used in nanotechnology for material manufacturing or characterizations have expanded their scope to be used also in cell biology [52, 53]. For instance, modern focused ion beam equipments (FIB) can include a SEM in the same vacuum chamber, obtaining a two-column FIB-SEM. The use of a SEM during this kind of experiments allows the cell observation after cutting. In addition, FIB equipment can be used to perform different cross-sections on the cell for an internal view by SEM. Using the combination of these two techniques not only provides valuable biological information, but also confirms the ICCs internalization.

Initially, the cultured cells were analyzed under an inverted microscope in order to identify the macrophages carrying an internalized silicon or polySilicon intracellular chip (Figure 2.10).
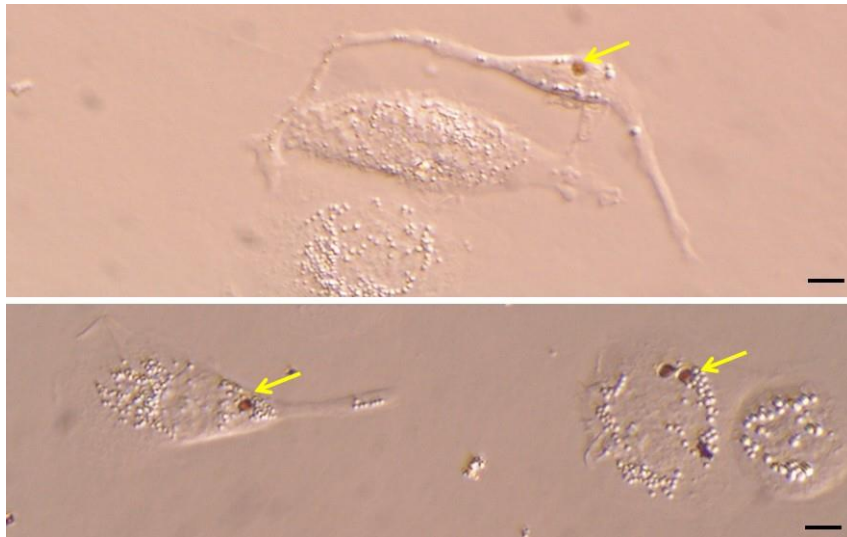
a
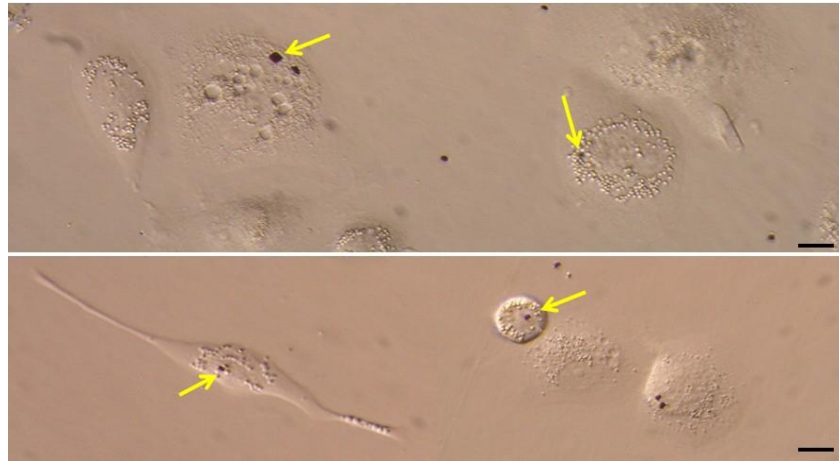
b

Figure 2.10: Bright field microscopy images of phagocyted Intracellular Chips by Human Macrophages. Bright field microscopy images of several cell-internalized a) polySilicon intracellular chips and, b) silicon intracellular chips. Yellow arrows indicate the chip location. Scale bar = 10 μm.

Then, to confirm the presence of the ICCs inside the cells, afterwards selected macrophages were analyzed under a scanning electron microscope. SEM images allowed distinguish ICCs lying on the cell surface or in the process of being phagocyted (Figure 2.11).
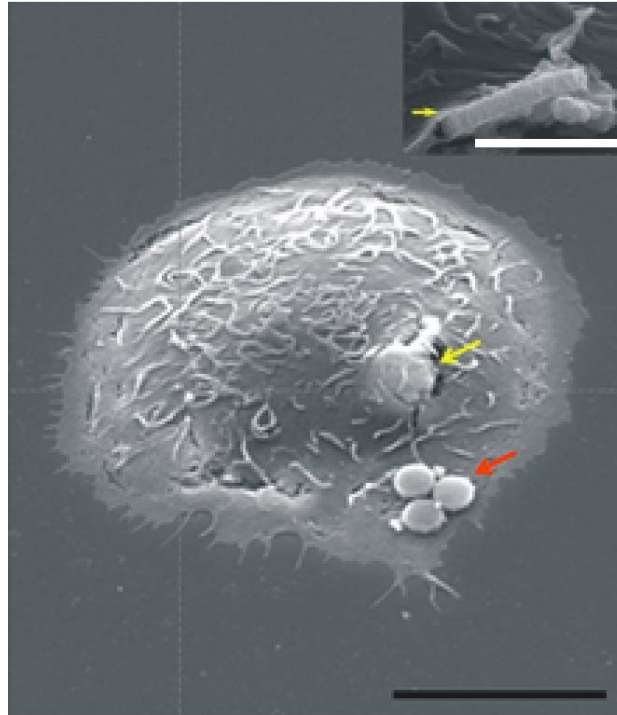

Figure 2.11: Scanning electron microscopy images of internalized Intracellular Chips by Human Macrophages. The red arrow indicates several polySilicon ICCs lying on the cell surface and the yellow arrow indicates a specific ICC in the process of being phagocyted. Scale bar = 10 µm. Inset: Zoom image. Scale bar = 3 µm.

Finally, some cells were chosen to be milled using a combination of FIB-SEM techniques. The images through this microscopy technique show with any doubt the ICCs inside the cell membrane (Figure 2.12).

Conclusively, a confocal laser scanning microscopy (CLSM) technique can be used to analyze the cell uptakes of the ICCs. To carry out this test, some macrophages were treated with wheat germ agglutinin (WGA), a plasma membrane dye (see Annexes of this chapter for further information), where ICCs were detected by reflected light. The obtained focal planes and orthogonal projections were used to validate the internalized ICCs (Figure 2.13). Likewise, SEM-FIB microscopy combination technique, also confirmed the ICC internalization (Figure 2.12).
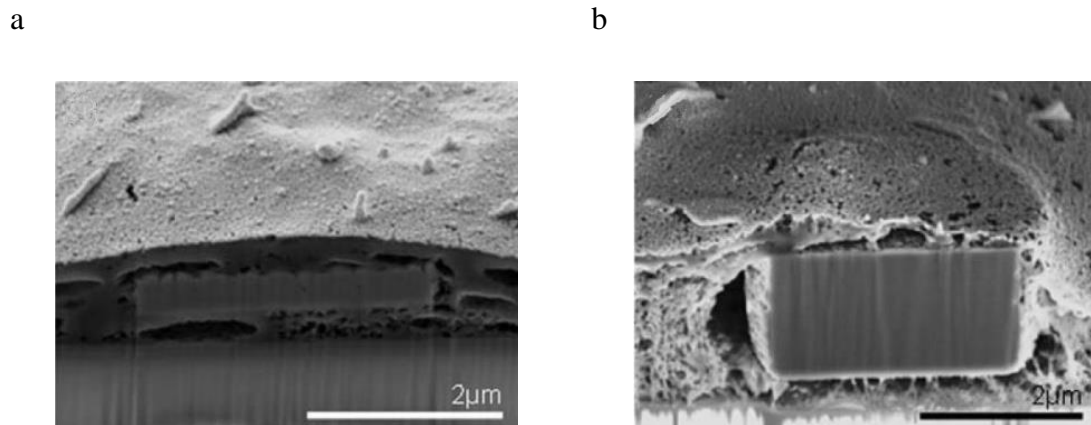
a   b

Figure 2.12: Scanning electron microscopy images of the studied Human Macrophages after the FIB nanomachining. a) A cross section of a phagocytized polySilicon intracellular chip. b) A cross section of a phagocytized silicon intracellular chip. Scale bar = 2 µm.
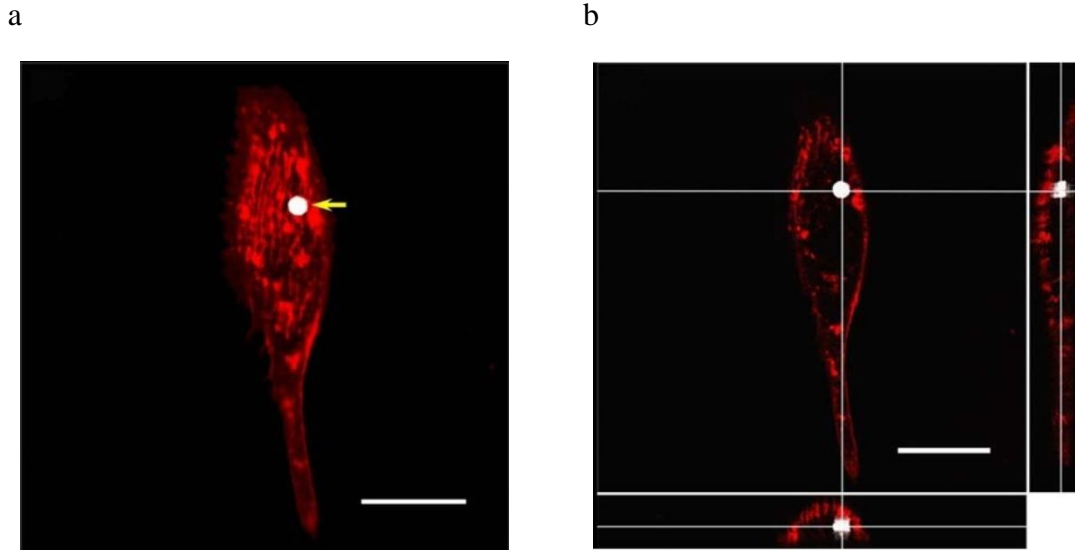
Figure 2.13: Confocal laser scanning microscopy images of a polySilicon Intracellular Chip phagocyted by a Human Macrophage. a) CLSM average projection image and b) orthogonal projections of the z-stack reconstructions of consecutive focal planes (0.2 µm each one) of a Human Macrophage with an internalized polySilicon ICC. The plasma membrane was labeled with WGA (red color). Scale bars = 20 µm.

### 2.9.2 Cell viability and cytotoxicity assays

In a physiological phagocytosis process, pathogens and particles are engulfed by macrophages forming a phagosome, which eventually matures into a lysosome, where the pathogen or particle is degraded. However, some pathogens have the capability to break away the early endosome and release themselves into the cytoplasm avoiding degradation [54]. Therefore, it is essential to determine the intracellular fate of phagocyted ICCs, for instance, whether they are trapped inside the endosomal/lysosomal compartment or they are at some point released into the cytosol. It is worth to mentioning that when the ICCs are tightly surrounded by the phagosomal membrane and the phagosome maturation is inhibited, the fusion with the lysosome does not occur [26, 56].

67

However, when the phagosome membrane is not so tight around the phagocyted ICCs, the phagosomes are able to mature and can fusion with lysosomes [26]. For this purpose, two biological-material characterization techniques can be used, Transmission electron microscopy (TEM) and Confocal laser scanning microscopy (CLMS). In this chapter the CLSM study will be summarized. The TEM analysis is described in our reference [57].

i. Intracellular Chip localization in Human Macrophages

To analyze the nature of the intracellular compartments in which the phagocyted intracellular chips were trapped, macrophages were fixed at different intervals after the addition to the cell cultures and immune labelled with EEA1 antibody or lysotracker. EEA1 is a tethering protein used to label early endocytic structures [58], where a lysotracker is a fluorescent probe for labeling and tracking acidic organelles like late endosomes and lysosomes [59]. The results showed that the number of ICCs with EEA1 protein (Figure 2.14a) increased overtime (36%, 41% and 71% for 1 h, 3 h or 6 h post ICC addition, respectively), where the number of ICCs localized in an acidic compartment (Figure 2.14b) did not change (36%, 30% and 36% for 6 h, 12 h or 24 h post ICC addition, respectively). Thus, after 6 h of ICC addition, about two thirds of the ICCs would be located inside an early endocytic compartment and about one third inside a late endosome or lysosome.
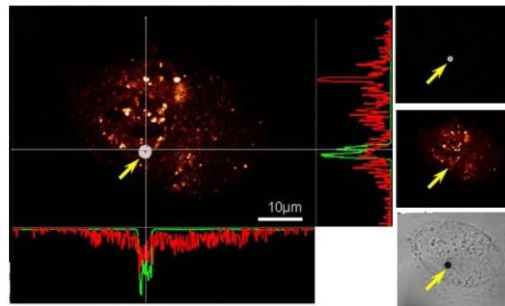
a
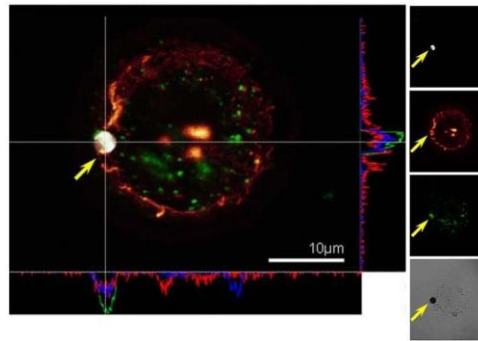
b

Figure 2.14: Intracellular localization of Intracellular Chips in Human Macrophages. a, left) CLSM cross-section image of a macrophage incubated during 3 h with polySilicon chips, and showing an internalized ICC inside an endosome. a, right) Small images show reflection light (white), plasma membrane (red), endosomes (green) and the whole cell (transmitted light). b, left) CLSM cross-section image of a macrophage incubated during 24 h with polySilicon chips, and showing an internalized ICC inside an acidic compartment. b, right) Small images right show reflection light (white), acidic compartment (red) and the whole cell (transmited light).

ii. Intracellular Chip citotoxicity in Human Macrophages

To analyze possible cytotoxic effects of the ICCs, Human Macrophages with phagocyted Si or polySi chips (n = 25) or without phagocyted chips (n = 70) were individually followed under an inverted microscope for 10 days. Cells were cultured over reticulated cover slips to enable tracing of individual cells. The initial macrophage population decreased over time, but this decrease is inherent for these differentiated cells as showed by the progressive reduction in the viability of the control group without ICCs. No significant differences in cell survival were observed between macrophages with or without phagocyted ICCs after 10 days (Figure 2.15). Cytotoxicity was also analyzed using the MTT assay (dimethyl thiazolyl diphenyl tetrazolium salt) and the results confirmed that no significant differences were present among the different groups.
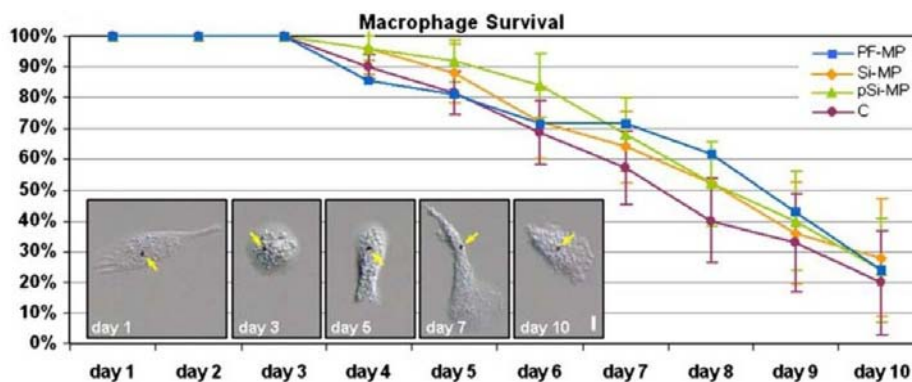

Figure 2.15: Percentage of surviving macrophages along time. Phagocyted Intracellular Chips individually followed for 10 days. Possible cytotoxic effects of the MPs, Human Macrophages with phagocyted Si- or pSi-MPs (n = 25 each), and control macrophages with phagocyted PF-MPs (n = 21) or without phagocyted MPs (n=70), individually followed under 10 days. Scale bar = 10 µm. [57]

2.10 Discussion and Conclusions

The technology developed to fabricate silicon and polySilicon Intracellular Chips was shown in this chapter. The chips were designed small enough to allow their posterior introduction inside living cells. The fabrication process is based on standard techniques used in semiconductor and MEMS industries. Two types of intracellular chips were designed, tested and fabricated, one made of silicon and the other fabricated in polySilicon, both 3 µm in diameter, but with different thickness, 0.5 µm and 1.5 µm respectively. Technology allowed the manufacture of more than 170 million of chips on a 100 mm-diameter both for a Si or a SOI wafer. One of the main challenges was to establish a method to release the intracellular chips out of the substrate. A commonly used method for manufacturing MEMS, based on the use of HF vapors for silicon oxide sacrificial-layer etching, was optimized and adapted to the release of the obtained devices. This method allowed an easy and safe procedure. An efficient collection process was also, developed, this process was composed of three steps; sonication, centrifugation and concentration, which allowed an easy handling and storage of ICCs.

From the biological point of view, by using laser confocal microscopy (commonly used in biology), we could demonstrated the internalization of the chips inside Human Macrophages. The majority of cells, initially identified by bright field microscopy as having internalized chips were indeed carrying a chip inside. Only in a very few cases the intracellular chips were found on the cell surface, and these were usually in the process of being phagocyted. These results clearly indicate that Human Macrophages are capable of phagocyting the designed Si and polySi intracellular chips. These results are in good agreement with those of two reported studies using mesoporous silica microparticles (2.5 µm-diameter) [20] and silicon micro- and nanoparticles (3 µm-diameter) [10]. The fact that the number of intracellular chips inside an acidic compartment

was not increased within 24 hours post chip addition, suggests that phagosomes containing the polySilicon chips might not be able to mature, indicating that internalized chips would be phagocyted surrounded by the phagosomal membrane not maturing into lysosomes. Cytotoxicity, was not observe when Si or polySi intracellular chips were located inside. However, it is important to note that intracellular chip concentration in this study was very low (0.5 µg/ml and to 1,3 µg/ml for Si and polySi chips, respectively) and the chips were homogeneous in size and shape.

This line of research involves the design, technological development and characterization of silicon and polySilicon intracellular chips, opening the possibility from now on to develop more complex devices, such as sensors and actuators, combining different materials, which may be useful for future multifunctional analysis *in situ* cell biology. In the future, intracellular chips could be designed to record or modify intracellular parameters inside the cells, and they should be able to interact directly with a specific target inside the intracellular cell environment.

Annexes

i Cell types, culture and manipulations

The human monocyticcelllineTHP-1(ECACCNo.88081201) was maintained in RPMI1640 medium (Gibco) with 20% FBS (Gibco) in standard conditions. THP-1cells were plated in 24-well dishes (20,000 cells/well) on reticulated glass cover slips, in presence of a final concentration of 0.16 MPMA (Sigma) during 3 days for macrophage differentiation. Fabricated silicon and polySilicon intracellular chips were added at a rate of 0.5/cell. Cumulus cells were dispersed by 5 min incubation in 156 U/ml of hyaluronidase (Sigma) inH-KSOM medium at 37 °C.

ii *Immunofluorescence*

To label early endosomes, macrophages were fixed with 4% paraformaldehyde in PBS (15 min), permeabilized in 0.25% TritonX-100 in PBS (15min), and blocked with 5% BSA in PBS (40 min) at RT. Permeabilized cells were incubated with primary EEA1 antibody (610456,BD Biosciences) at a 1:100 dilution in PBS with 5% BSA for 1h at 37 °C, followed by three washes with PBS, and then with an AlexaFluor 488 goat anti-mouse secondary antibody (A11017,Invitrogen) at a 1:500 dilution in PBS with 5% BSA together with 1.5U/ml Texas-Redphalloidin (T-7471,MolecularProbes) for 1h at 37 °C. To label acidic compartments, macrophages were incubated in LysoTrackerred DND-99 (L-7528, Invitrogen) at 1M for 1h at 37 °C, and then fixed with 4% paraformaldehyde in PBS for 10 min at RT.

iii Cell imaging

Macrophage viability was followed under an IX71 inverted microscope (Olympus) with differential interference contrast. To localize internalized ICCs, macrophages were fixed 24 h after device addition in Karnovskys solution (2% paraformaldehyde and 2.5% glutaraldehyde) at RT, dehydrated in an ethanol series, critical point-dried using CO_2 (K850 critical point drier Emitech), mounted on the specimen holder, coated with gold, and observed in aJEOLJSM-6300SEM, equipped with an energy dispersive X ray spectrometer (Link ISIS-200, Oxford). Using a combined Strata 235 Dual Beam FIB-SEM workstation (FEI), cells were sectioned by the FIB beam to visualize the intracellular chips. To identify internalized ICCs a TCSSP2AOBS CLSM with 63X oilimmersion optics (Leica) was used. Macrophage plasma membrane was labeled with WGA Texas Red conjugated (Molecular Probes) according to the manufacturer's protocol. Cells processed for the immune fluorescence detection of endosomal and lysosomal compartments were also analyzed under the CLSM. In both cases, processing and 3D reconstructions were performed with LCS Lite software (Leica).

Bibliography

[1] C. Chen, M. Mrksich, S. Huang, G. Whitesides, D. Ingber. Science 276 (5317), 1425 (1997)

[2] D. Figeys, D. Pinto. Analytical Chemistry 72 (9), 330A (2000)

[3] R. E. Oosterbroek, A. van den Berg. Lab Chip. Elsevier Ltd. (2003)

[4] R. Daw, J, Finkelstein. Nature 442 (7101), 367 (2006)

[5] C. R. Kesse, I. Giaever. IEEE Eng. Med. Bio. Mag. 13 (3), 402 (1994)

[6] T. Park, M. Shuler. Biotechnol. Prog. 19, 243 (2003)

[7] R. Singhvi, A. Kumar, GP. Lopez, Gn. Stephanopoulos, Di. Wnag, G. M. Withesides, DE. Ingber. Science 264 (5159), 696 (1994)

[8] C. Chen, M. Mrksich, S. Huang, G. Whitesides, D. Ingber. Biotechnol. Prog. 14, 356 (1998)

[9] S. Sia, G. Whitesides. Electrophoresis 24, 3563 (2003)

[10] G. Bao, S. Suresh. Nat. Mater. 2 (11), 715 (2003)

[11] S. E. Cross, Y. S. Jin, J. Rao, J. K. Gimzewski. Nat. Nanotechnol. 2 (12), 780 (2007)

[12] T. P. Burg, M. Godin, S. M. Knudsen, W. Shen, G. Carlson, J. S. Foster, K. Babcock, S. R. Manalis. Nature 446 (7139), 1066 (2007)

[13] D. S. Gray, J. L. Tan, J. Voldman, C. S. Chen. Biosens. Bioelectron. 19 (12), 1763 (2004)

[14] H. Lee, Y. Liu, D. Ham, R. M. Westervelt. Lab Chip 7 (3), 331 (2007)

[15] J. Fritz, M. K. Baller, H. P. Lang, H. Rothuizen, P. Vettiger, E. Meyer, H. J. Guntherodt, C. Gerber, J. K. Gimzewski. Science 288 (5464), 316 (2000)

[16] G. Shekhawat, S. H. Tark, V. P. Dravid. Science 311 (5767), 1592 (2006)

[17] J. Lu, M. Liong, J. I. Zink, F. Tamanoi. Small 3 (8), 1341 (2007)

[18] E. Tasciotti, X. W. Liu, R. Bhavane, K. Plant, A. D. Leonard, B. K. Price, M. M. C. Cheng, P. Decuzzi, J. M. Tour, F. Robertson, M. Ferrari. Nat. Nanotechnol. 3 (3), 151 (2008)

[19] H. Vallhov, S. Gabrielsson, M. Stromme, A. Scheynius, A. E. Garcia-Bennett. Nano Lett. 7 (12), 3576 (2007)

[20] A. Verma, O. Uzun, Y. H. Hu, Y. Hu, H. S. Han, N. Watson, S. L. Chen, D. J. Irvine, F. Stellacci. Nat. Mater. 7 (7), 588 (2008)

21] Y. Pan, S. Neuss, A. Leifert, M. Fischler, F. Wen, U. Simon, G. Schmid, W. Brandau, W. Jahnen-Dechent. Small 3, 1941 (2007)

[22] I. Slowing, B. G. Trewyn, V. S. Y. Lin. J. Am. Chem. Soc. 128 (46), 14792 (2006)

[23] P. B. Kang, A. K. Azad, J. B. Torrelles, T. M. Kaufman, A. Beharka, E. Tibesar, L. E. DesJardin, L. S. Schlesinger. J. Exp. Med. 202 (7), 987 (2005)

[24] C. Foged, B. Brodin, S. Frokjaer, A. Sundblad. Int. J. Pharm. 298 (2), 315 (2005)

[25] L. Thiele, B. Rothen-Rutishauser, S. Jilek, H. Wunderli-Allenspach, H.P. Merkle, Walter. J. Control. Release 76 (12), 59 (2001)

[26] L. Thiele, H. P. Merkle, E. Walter. Pharm. Res. 20 (2), 221 (2003)

[27] S. Faraasen, J. Voros, G. Csucs, M. Textor, H. P. Merkle, E. Walter. Pharm. Res. 20 (2), 237 (2003)

[28] A. J. Gomes, A. S. Faustino, A. E. H. Machado, M. E. D. Zaniquelli, T. D. Rigoletto, C. N. Lunardi, L. O. Lunardi. Drug Deliv. 13 (6), 447 (2006)

[29] J. Choi, Q. Zhang, V. Reipa, N. S. Wang, M. E. Stratmeyer, V. M. Hitchins, P. L. Goering. J. Appl. Toxicol. 29 (1), 52 (2009)

[30] S. St. John, I. Dutta, A. P. Angelopoulos. Langmuir 27, 5781 (2011)

[31] C. J. Murphy, T. K. Sau, A. M. Goles, C. J. Orendorf, J. Gao, L. Gou, S. E. Hunyadi, T. Li. J. Phys. Chem. B 109 (29), 12857 (2005)

[32] J. A. Chang, M. Vithal, I. C. Baek, S. I. Seok. J. Nanosci. Nanotech 10 (1), 163 (2010)

[33] J. Stone, S. Jackson, D. Wright. Nanomed. Nanotech. 3 (1), 100 (2011)

[34] M. Bendayan. Biotech. Histochem. 75 (5), 203 (2000)

[35] T. Hiura, H. Koseko, K. Shiraishi, T. Ashara, T. Tsurumoto, H. Sindo, K. Baba, H. Taoda, N. Terasaki. Biomed. Res. 31 (2), 151 (2010)

[36] J. Fan, P. Chu. Small 6 (19), 2080 (2010)

[37] A. M. Smith, H. Duan, A. M. Mohs, S. Nie. Adv. Drug. D. Reviews 60 (11), 1226 (2008)

[38] M. Madou. Fundamentals of Microfabrication, CRC Press (1997)

[39] S. E. Lyshevski. Nano- and Microelectromechanical Systems, CRC Press (2000)

[40] M. Gad-el-Hak. The MEMS Handbook, CRC Press (2001)

[41] N. Maluf. An Introduction to Microelectromechanical Systems Engineering, Artech House (1999)

[42] T-R Hsu. MEMS and Microsystems: Design and Manufacture, McGraw-Hill (2001)

[43] J. Bhler, F-P. Steiner, H. Blates. J. Micromech. Microeng. 7, R1 (1997)

[44] D. Viet-Dao, K. Nakamura, T. Thanh-Buiand, S. Sugiyama. Adv. Nat. Sci.: Nanosci. Nanotechnol. 11 (2010)

[45] W.E. Kline, H. Fogler. Ind. Eng. Chem. Fundam. 20155 (1981)

[46] T. A. Lober, R. T. Howe. Digest Tech. Papers, Solid-State Sensor and Actuator Workshop 59 (1988)

[47] M. Marsh, H. T. McMahon. Science 285 (5425), 215 (1999)

[48] M. Marsh. Endocytosis, Oxford University Press (2001)

[49] S. D. Conner, S. L. Schmid. Nature 422 (6927), 37 (2003)

[50] R. King. Methods in Molecular Biology 245,167 (2004)

[51] P. l. Felgner, T. R. Gadek, M. Holm, R. Roman, H. W. Chan, M. Wenz, J. P. Northrop, G. M. Ringoldand, M. Danilesen. PNAS 84 (21) 74137417 (1987)

[52] S. Ryntjens, R. Puers. J. Micromech. Microeng. 11, 287 (2001)

[53] K. Grandfield. Hakan Engvsit. Adv. Mat. Sci. Eng. 1 (2012)

[54] N. van der Wel, D. Hava, D. Houben, D. Fluitsma, M. van Zon, J. Pierson, M. Brenner, P. J. Peters. Cell 129 (7), 1287 (2007)

[55] A. M. Javier, O. Kreft, M. Semmling, S. Kempter, A. G. Skirtach, O. T. Bruns, P. del Pino, M. F. Bedard, J. Raedler, J. Kaes, C. Plank, G. B. Sukhorukov, W. J. Parak. Adv. Mater. 20 (22), 4281 (2008)

[56] C. de Chastellier, L. Thilo. Cell. Microbiol. 8 (2), 242 (2006)

[57] E. Fernández-Rosas, R. Gómez, E. Ibañez, L. Barrios, M. Duch, J. Esteve, J. A. Plaza, C. Nogués. Biome. Micro. 12, 371 (2010)

[58] S. C. W. Richardson, K. L. Wallom, E. L. Ferguson, S. P. E. Deacon, M. W. Davies, A. J. Powell, R. C. Piper, R. Duncan. J. Control. Release 127 (1), 1 (2008)

[59] K. K. Huynh, E. L. Eskelinen, C. C. Scott, A. Malevanets, P. Saftig, S. Grinstein. Emboj. 26 (2), 313 (2007)

Chapter 3

Intracellular polySilicon Barcodes for single cell labeling

3.1 Abstract

3.2 Introduction

3.3 Concept

3.4 2D PolySilicon-based Barcodes

      3.4.1 Design of 2D polySilicon Barcodes

      3.4.2 Wafer layout for the fabrication of 2D polySilicon Barcodes

      3.4.3 Technology development for the fabrication of 2D polySilicon Barcodes at wafer level

      3.4.4 Release of 2D polySilicon Barcodes

      3.4.5 Collection of 2D polySilicon Barcodes

      3.4.6 Physical characterization of 2D polySilicon Barcodes

3.5 3D Silicon-based Barcodes

      3.5.1 Design of 3D Silicon Barcodes

      3.5.2 Wafer layout for the fabrication of 3D Silicon Barcodes

      3.5.3 Technology development for the fabrication of 3D Silicon Barcodes at wafer level

3.1 Abstract

Microworld barcoding has become a promising tool for cell biology, as population cell labeling or tracking is becoming a great interest in order to evaluate cell behavior. During the past decade diverse types of barcodes have been designed with the main objective of tracking living cells *in vivo* or *in vitro*, but none of them offer the possibility to label an individual cell up to ten or more days.

On the other hand, nowadays, many micrometer and even nanometer size silicon structures can be fabricated using microelectronics techniques. These techniques allow us to fabricate barcodes small enough to be introduced into a living cell and continue being visible and easily identifiable under an optical microscope. Additionally, silicon microtechnologies could also allow the production of a mass of reproducible codes, with a numerical representation, completely into the micrometer range, and even using biocompatible materials.

In this chapter, 2D and 3D barcodes (of an approximately volume dimensions of 30 μm^3 and 127 μm^3, respectively), using silicon as starting material, are designed. In addition, a fabrication technology based on photolithographic and deep reactive ion etching (DRIE) techniques processes are proposed. These techniques will allow us to obtain micrometer-size 2D rectangular cuboid and 3D cylindrical barcode structures with binary codifications. Although these technologies could achieve several bits representations, only 4-8 bits will be necessary for our initial purpose. The results of this work will show that photolithographic and DRIE processes are high versatile techniques to produce biocompatible Silicon-based Barcode structures for intracellular cell applications.

3.2 Introduction

An increasing demand for tracking even smaller items has driven the exploration for novel methods of barcoding at much smaller scales [1]. In the last decade, individual and sub-population cell tracking, in order to evaluate cell behavior under different conditions, has become a crucial area in life sciences [2]. Conversely, based on micro- and nanotechnologies, several encoded particles have been proposed to follow up cells in culture, such as quantum-dot-tagged microbeads [3] (Table 3.1.1a), metallic barcodes [4, 5] (Table 3.1.1b-c), porous-silicon photonic crystals [6] (Table 3.1.2d), and diamond nanoparticles [7] (Table 3.1.2e). While some of these particles act as a kind of barcodes because of their own nature, many of them are required to be read by fluorescence microscopes [3, 8] or by confocal scanning laser microscope to visualize them. However UV light and laser beams have been reported to be extremely harmful for living cells [9]. In any case, non-florescence light microscopes are the most well-used characterization tool in cell biology.

Now, from a biological point of view, codes must be designed into the micrometer size, as they should be small enough to be introduced into a living cell and, additionally, be made of a biocompatible material in order to ensure cell viability. Furthermore, from an optical point of view, the codes should be simple and visible under light microscopes. For this reason, the minimum features that represent every single *bit* have to be larger than 1 μm, the practical resolution limit of these microscopes. Finally, the fabrication technology of the codes has to be able to mass-produce reproducible codes at low cost with small features (*bits*) into the micrometer range, as these *bits* will allow the barcode use.

Nowadays, Silicon-based technologies, applied to obtain microelectromechanical systems (MEMS) and nanoelectromechanical systems (NEMS), can fulfill these requirements and

produce this kind of devices. For instance, silicon structures are already mass-produced by semiconductor industries at the micrometer and submicrometer scale. As complex silicon structures should be precisely micronanomachined, and they can offer high performance, versatility [8] and biocompatibility [9].

In this chapter the technology fabrication and manipulation of 2D and 3D barcodes, trough common microelectronics techniques is reported. Silicon and polySilicon, common materials in MEMS industry, are selected as device materials because of their well-known physical, chemical and biocompatibility properties [10-13]. While 2D barcodes are defined with vertical dimensions by the thickness of device layer and the use of photolithographic techniques to define the lateral dimensions, the 3D barcodes are defined with several deep reactive ion etching (DRIE) processes.

Finally, the perspective of cell viability of these barcodes is analyzed, and a short overview of the biological applications developed during this work will be shown (this part has been done in partnership with the group of *Dr. Carme Nogués - Department of Cellular Biology, Physiology and Immunology, Universitat Autònoma de Barcelona*). Cellular Human Macrophages will be used as cell line, because of their natural capacity to engulf easily large particles.

This study addresses the barcode concept and the barcode fabrication technology as silicon and polySilicon labels for single living cell labeling and tracking.

b. **Metallic barcodes**. Optical properties of cylindrical striped particles. Reflectance optical microscopy images and line profiles for a particle of composition Au-Ag-Ni-Pd-Pt with illumination at 430 nm, 520 nm, and 600 nm, respectively (Reproduced with permission from Reference [4]. Copyright®2001).

a. **Dot-tagged microbead.** Schematic illustration of optical coding based on wavelength and intensity multiplexing. Large spheres represent polymer microbeads in which small colored spheres (multicolor quantum dots) are embedded according to predetermined intensity ratios (Reproduced with permission from Reference [3]. Copyright®2001).
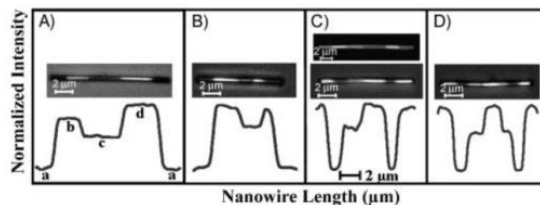
c. **Metallic barcodes.** Reflectance images (top) and intensity lines (bottom) for different multisegment alloy nanowire barcodes (Reproduced with permission from Reference [5]. Copyright®2002).

Table 3.1.1: Examples of encoded microparticles used for several applications.
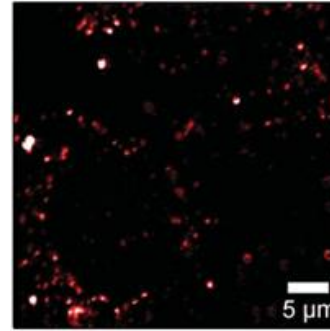
d. **Porous-silicon photonic crystals.** Optical microscope image of rugate-encoded porous-silicon particles, photolithographically defined into 94 mm-square, 5 mm-thick, on a silicon wafer. Inset, a square particle after removal from the substrate. The color of the particles derives from the periodicity defined in the photonic crystal during the etch (Reproduced with permission from Reference [6]. Copyright®2008).

e. **Diamond nanoparticles**. Photoluminescence of nanodiamonds (PNDs) localized with endosomes (Reproduced with permission from Reference [7]. Copyright®2008).

Table 3.1.2: Examples of encoded microparticles used for several applications.

3.3 Concept

A barcode is an optical readable numerical representation used to uniquely identify an item or object. The most known barcodes use parallel lines (wide and narrow bars), and are designed to be used in only one dimension (1D). However, in this thesis, two types of Silicon-based Barcodes, named two-dimensional (2D) and three-dimensional (3D) barcode representations, are proposed.

3.4 2D PolySilicon-based Barcodes

3.4.1 Design of 2D polySilicon Barcodes

The first design, named 2D barcodes, consists of a matrix code composed of several pentagonal digits arranged on an array pattern. The matrix is divided into a regular 4 x 2 grid (Figure 3.1a) which contains a total of 8 bits (1 or 0) (Figure 3.1b). Barcodes should be asymmetric in order to allow the correct reading of data, for this reason, the barcodes have been designed with a start marker to help the user to read the message in its correct orientation (Figure 3.1c). The data capacity, that is, the number of possible different codes, depends on the number of bits of each barcode. The proposed design has 8 bits, which means 256 different binary combinations, from 0 to 255. Figure 3.2a shows three different codes. For instance, if every pentagon is present the binary code is *1111 1111$_b$*[1], which in decimal representation corresponds to the number *255$_d$*[2]; In the case of the pentagon Bit 8 is left the binary code would be *0111 1111$_b$*[1], which in decimal representation corresponds to the number 127$_d$[2]; and if every pentagon is left the binary code would be *0000 0000$_b$*[1], which corresponds to the number *0$_d$*[2]. A schematic view of the 256 different codes is shown in Figure 3.2b ([1]$_b$ = Binary code; [2]$_d$ = Decimal code).
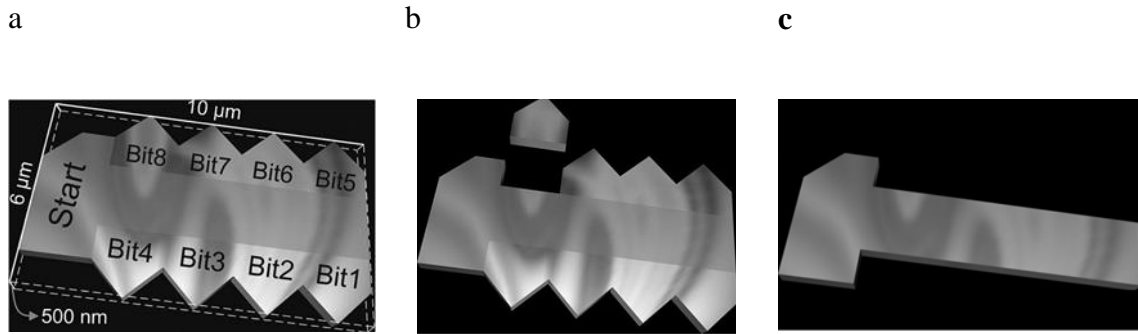
Figure 3.1: Conceptual representation of a 2D polySilicon Barcode. a) A 2D barcode showing its dimensions and the complete array of bits. b) A code with one bit left (bit number 8). c) The asymmetric structure indicating the starting point to the barcode reader (top left).

The barcode dimensions should accomplish some requirements in terms of cell biology and identifiability, for instance, the devices should be small enough to be introduced into different cell types. Typical cells have volumes in the range from 500 to 15 000 μm^3 and considering that most cell studies are performed using light and confocal microscopes, features smaller than 1 μm could be difficult to identify, for this reason the lateral dimensions of the barcodes were fixed to 10 μm x 6 μm.

In contrast, the thickness of a single barcode is fixed to submicrometer dimensions (500 nm), according to the small volume criteria. Due to the submicrometer range of the thickness of the barcode, the maximum volume of an individual barcode was only 30 μm^3, thus, the volume of the barcode is approximately 20 to 500 times smaller than many typical cells.
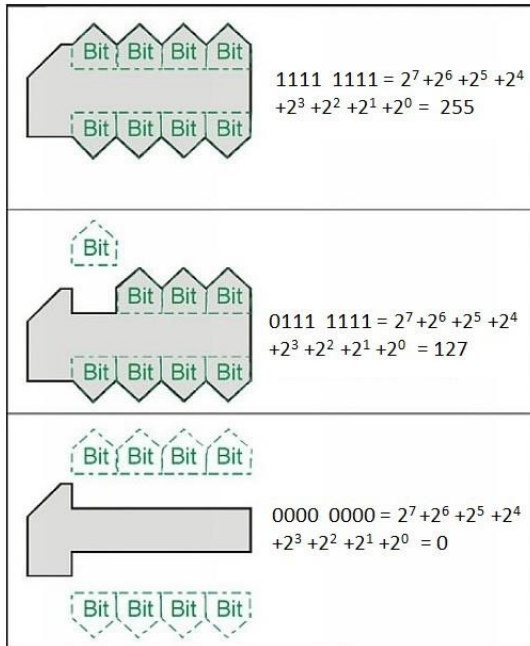
a   b
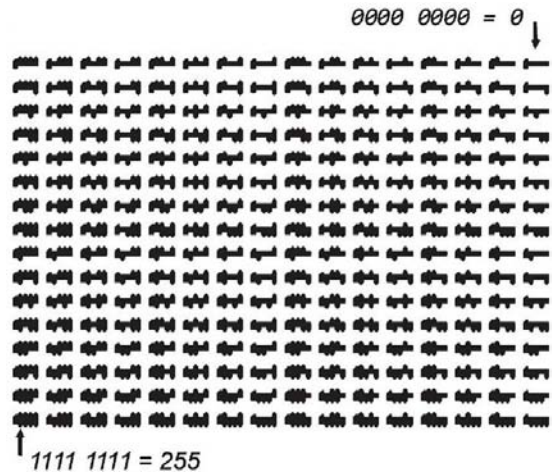
Figure 3.2: Schematic representation of the full range of the 2D polySilicon Barcodes. a) Examples of the equivalent binary and decimal data for three different examples of barcodes. b) Pattern of the 256 different combinations. The series starts from top right and ends at the bottom left.

3.4.2 Wafer layout for the fabrication of 2D polySilicon Barcodes

Silicon wafers are default substrates in microelectronic techniques, where the wafer dimensions limit the maximum number of enabled devices to be manufactured. For a 10 µm x 6 µm device spaced 3 µm distributed in a 100 mm-wafer, the fabrication yields close to eight millions devices (Figure 3.3).
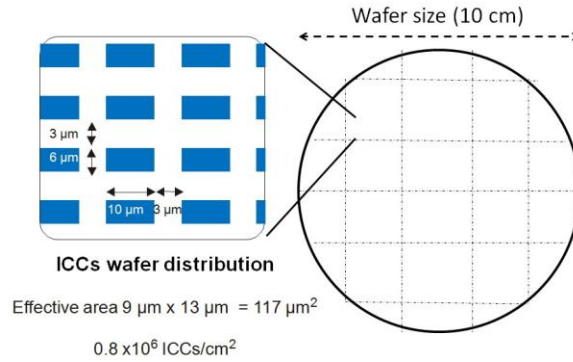
Figure 3.3: Distribution of 2D polySilicon Barcodes at wafer level. Schematic representation of barcode distribution along the wafer surface.

3.4.3 Technology development for the fabrication of 2D polySilicon Barcodes at wafer level

The 2D Silicon-based Barcodes were fabricated combining photolithographic with microelectronic fabrication techniques. The fabrication technology (Figure 3.4) was based on the combination of a device layer (polySilicon) and a sacrificial layer (silicon dioxide) on a 100-mm silicon wafer. First, using a plasma-enhanced chemical vapor deposition (PECVD) a silicon oxide layer was deposited on the front side of a silicon wafer to be used as a sacrificial layer (Figure 3.4a and 3.4b). This material was selected because it can be easily removed by hydrofluoric acid (HF), meanwhile polySilicon (our device material) is resistant to HF etching processes. The next step was the deposition of a 0.5 µm-thick polySilicon layer through a low pressure chemical vapor deposition (LPCVD) process (Figure 3.4c). Then, the barcodes were patterned by a photolithographic step (Figure 3.4d) and a subsequent dry etching process (Figure 3.4e). The etching uniformity and the vertical profile along the wafer were required due to the small dimensions of the codes (10 x 6 x 0.5 μm^3). An inductively coupled plasma etcher (ICP, Alcatel A601) was used, as it offers a 5% etch uniformity and provides an extremely vertical

etching profile. Barcodes were patterned by vertical dry etching using an optimized Bosh process recipe [14]. The etching process was stopped at silicon oxide layer and then the photoresist layer was removed by plasma etching (Figure 3.4f).
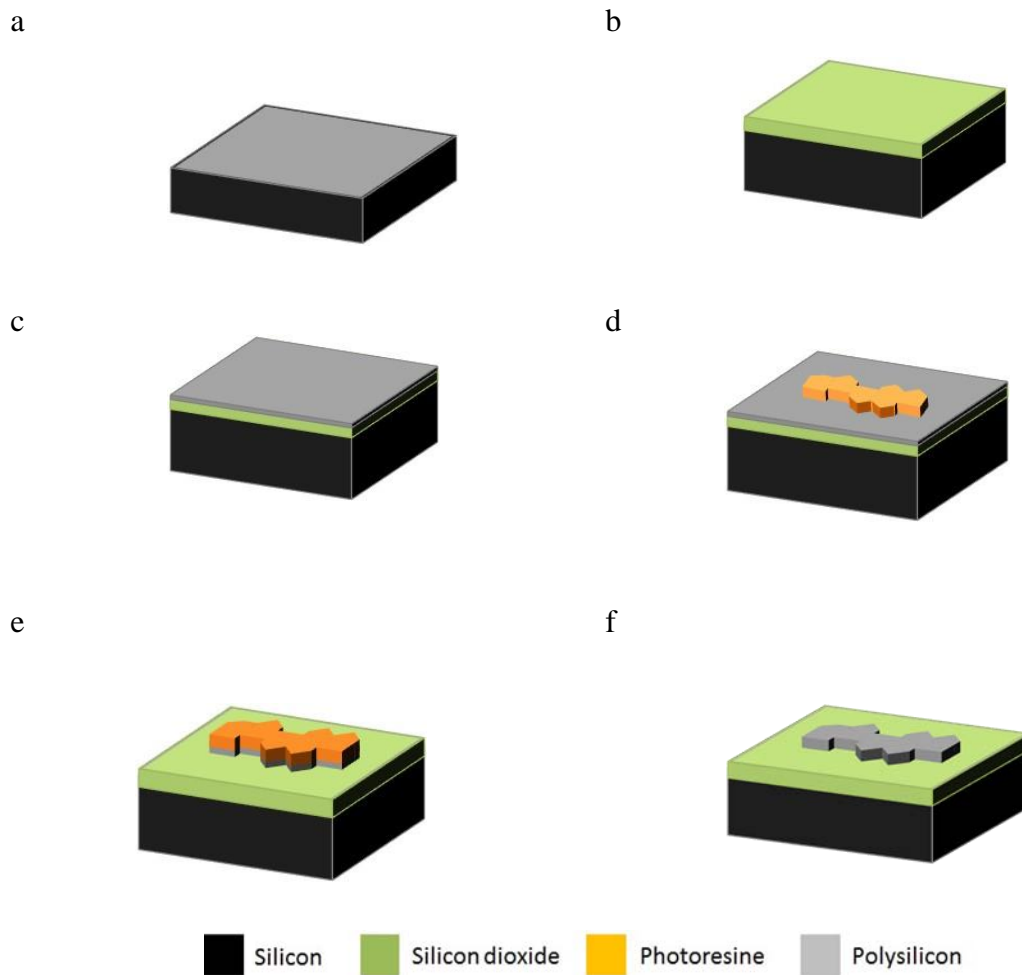
Figure 3.4: Fabrication process of 2D PolySilicon-based Barcodes. a) Silicon substrate as starting material, b) 1 µm-thick silicon dioxide was deposited as sacrificial layer, c) a 0.5 µm-thick polySilicon layer was deposited as device layer. d) 2 µm-thick photoresist layer was spun and exposed to fix the device area. e) PolySilicon layer was pattern by dry etching to define the barcodes. f) Photoresist layer was removed by plasma etching.

3.4.4 Release of 2D polySilicon Barcodes

Once the manufacturing process was finished (Figure 3.4), the wafer was divided into several small pieces (1 cm x 1 cm) using a diamond tip for a better handling (as it was already mentioned in subsection 2.7.1). Then, each piece was placed in a Teflon® holder, where it was subjected to a 40-minute 49% HF wet etching (Figure 3.5).
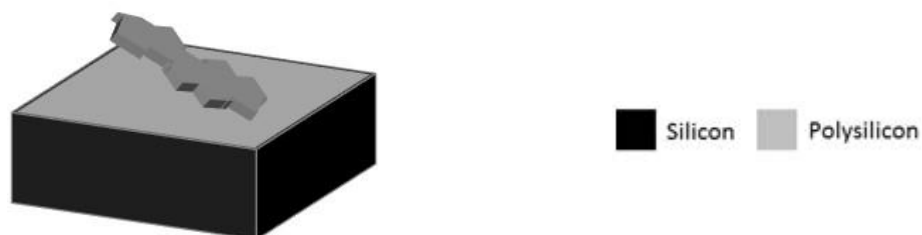
Figure 3.5: Release process of the 2D polySilicon Barcodes. Hydrofluoric acid wet etching step was carried out to release the 2D barcodes from the silicon substrate.

3.4.5 Collection of 2D polySilicon Barcodes

After 2D polySilicon barcodes etch, they were still attached to the silicon substrate (as it was already mentioned in subsection 2.7.2). So, the next step was oriented to collect them in suspension.

The piece of wafer was immersed in a glass beaker, which contained a few milliliters of 96% ethanol, next a sonicated step was performed and finally, the 2D polySilicon-based Barcodes were suspended in ethanol, distributed in different Eppendorf's (which contained a filter to prevent large wastes, as pieces of wafer) and collected by centrifugation at 14000 rpm for 5 minutes (Figure 2.7).

Collected 2D polySilicon barcodes can be stored until needed, however before handling the Eppendorf's should be centrifuged and the supernatant extracted. This allows the manipulation of the devices in microliter quantities by using micropipettes.

3.4.6 Physical characterization of 2D polySilicon Barcodes

Scanning electron microscopy (SEM) was used to characterize the fabricated devices (Figure 3.6). The results show that the barcodes do not break during fabrication or collection processes, which could be one of the main sources of false identification. Also, the SEM images show that fabricated barcodes maintain perfectly their well-defined shape and homogeneous surface even after the wafer release

a   b   c
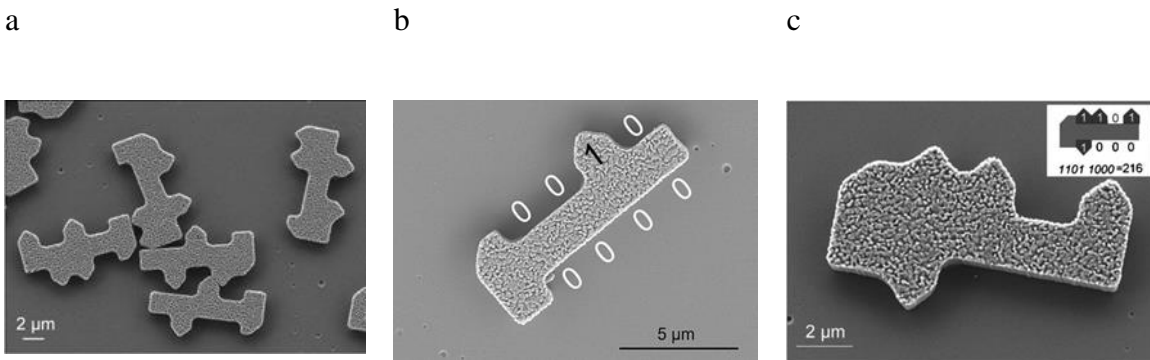
Figure 3.6: Fabrication results of 2D polySilicon-based Barcodes. Scanning electron microscopy images of 2D polySilicon barcodes with a) different binary codes, b) with the binary code *0011 0000$_b$* and c) with the binary code *1101 1000$_b$* that corresponds to decimal number *216$_d$*.

3.5 3D Silicon-based Barcodes

3.5.1 Design of 3D Silicon Barcodes

The second design, called 3D barcodes, presents a cylindrical-like shape, including also a start marker as identification system. The start marker is an asymmetric structure that allows the reader the correct reading of data (Figure 3.7a). The digits are small stacked structures centered on the start marker. The bits have two possible values (0 or 1), and are represented by a uniform cross-section cylinder (bit = 1_b) and a non-uniform cross-section cylinder (bit = 0_b, Figure 3.7b).

The data capacity of the barcode (number of possible difference codes) depends on the number of bits, which it is equivalent to the number of stacked cylindrical structures (Figure 3.7c). As it has been already mentioned, the barcode dimensions have to fulfil some requirements in terms of cell biology and visibility, such as barcode dimensions and biocompatible materials. Considering the code visibility and their intracellular applications, the lateral dimensions of a single bit were fixed approximately to 3 µm. Figure 3.7d shows an example of a 6 bit-code. The illustrated binary code is 011001_b that in decimal corresponds to the number 25_d.
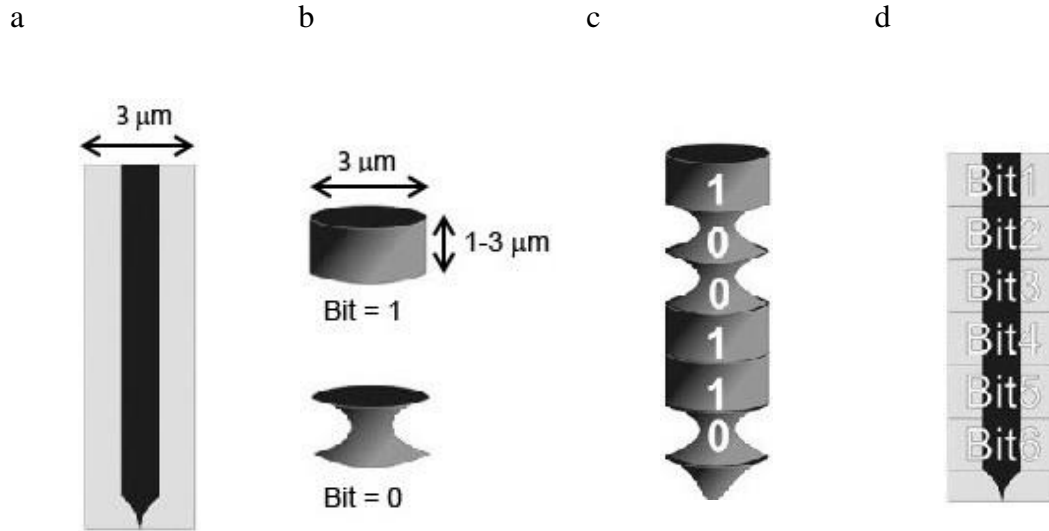
Figure 3.7: Conceptual representation of a 3D Silicon Barcode. a) Correct reading marker. b) Bit = 1 and bit = 0 representations. c) 3D representation of the code *011001$_b$*. d) Start marker and bit localizations.

3.5.2 Wafer layout for the fabrication of 3D Silicon Barcodes

As it was described at section 2.5, silicon wafers are the default substrates in device fabrication process. Wafer dimensions limit the maximum number of enabled devices to be manufactured. Using the same wafer layout described for intracellular chips fabrication process (3 µm x 3 µm-device, spaced 3 µm distributed in a 100 mm-wafer) (Chapter 2), the fabrication yields up to 150 million of 3D Silicon-based Barcodes (Figure 2.4).

3.5.3 Technology development for the fabrication of 3D Silicon Barcodes at wafer level

The proposed fabrication technology is based on silicon micromachining techniques in order to obtain micrometer-sized structures with well-controlled geometries, robustness and at low cost mass production. The key of this fabrication technology is that the code number is not defined by the photolithographic step. Therefore, the codes are defined by a series of sequential dry etching processes. The same pattern delimited the mask, and photoresist spots of 3 µm- diameter are used repetitively as many times as bits want to be defined. A vertical profile defines a bit $= 1_b$ and a non-vertical profile defines a bit $= 0_b$.

The fabrication technology of these barcodes is presented in Figure 3.8. First, a silicon wafer was used as a substrate (Figure 3.8a). A 1.5 µm-thick silicon dioxide layer was thermally grown (Figure 3.8b) and a photolithographic step was done to define spots of 3 µm x 3 µm (Figure 3.8c). The silicon dioxide layer was patterned by a reactive ion etching (RIE) process (Figure 3.8d and 3.8e). Next, every single bit was done by a silicon DRIE process (Figure 3.8f-i). Thus, we can freely program the codes along the axis by simply choosing the DRIE conditions to obtain vertical or non-vertical etched profiles. For instance, the bit $= 1_b$ was obtained by a vertical profile etching. Meanwhile the bit $= 0_b$ required a non-vertical profile etching in combination with a preceding 300 Å-thick silicon thermal oxidation in order to protect the bits already done. Without this oxide layer the previous bits would be destroyed. Following this method, an additional silicon oxide RIE step was required to remove the 300 Å-thick silicon dioxide protection layer before etching the next bit.
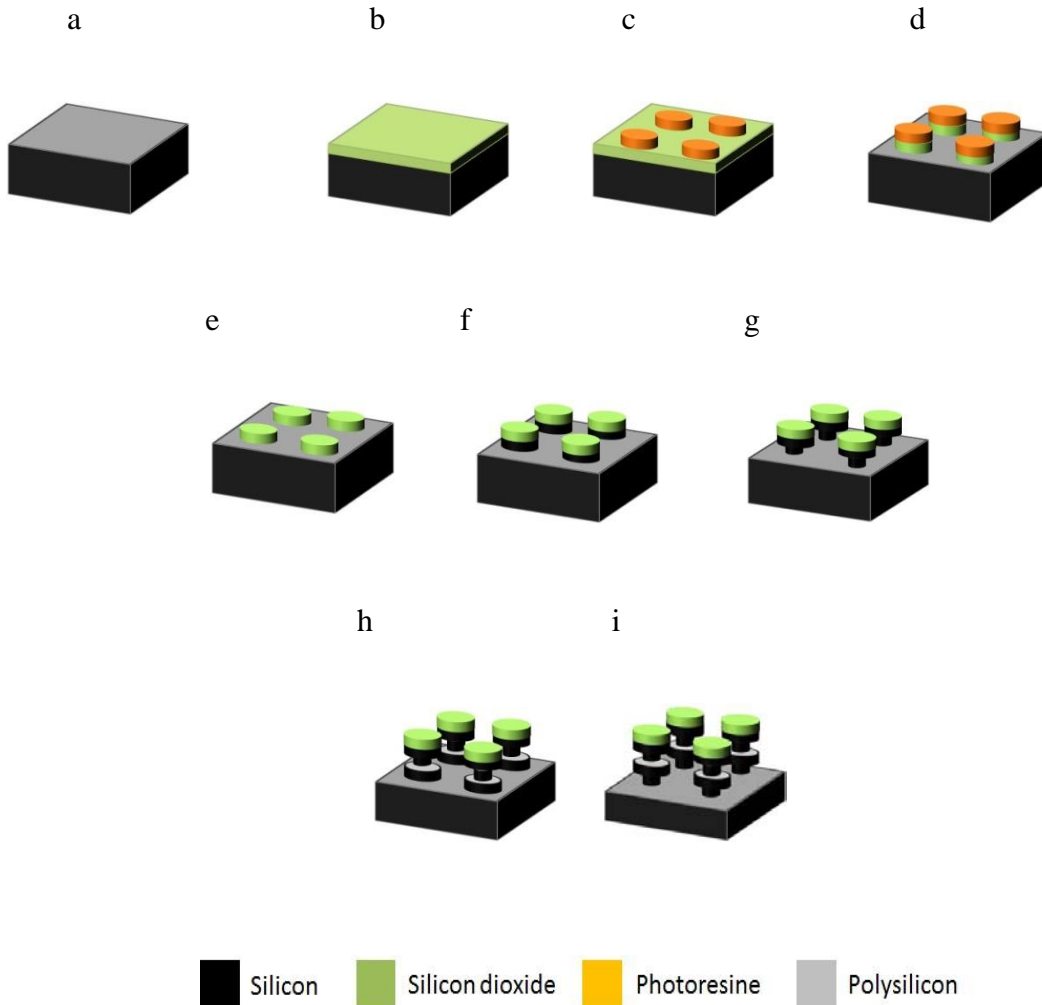
Figure 3.8: Fabrication process of the 3D Silicon Barcode 0101_b. a) Silicon wafers were used as starting material. b) A silicon dioxide layer was deposited. c) A photolithographic process defined the barcode design. d) The silicon dioxide layer was patterned to act as mask material. e) Photoresist removed. f) The silicon layer was etched by DRIE vertical profile creating a bit $= 1_b$. Then, g) an oxidation process was promoted and a silicon DRIE with non-vertical profile process was performed, bit $= 0_b$. h) An additional vertical etching, bit $= 1_b$, and i) a non-vertical etching, bit $= 0_b$ were performed.

An Alcatel A601 ICP (inductively coupled plasma equipment) was used for the DRIE processes and two recipes were designed for this equipment (Recipe A for vertical profiles and Recipe B for non-vertical profiles). Recipe A was based on a method which couples simultaneously the ion bombardment with the deposition of a chemical etch resistant polymer to achieve high vertical profiles and to avoid the scalloping produced when a DRIE Bosh process is used [15, 16]. And Recipe B was based on the ion bombardment without deposition of the passivation layer in order to achieve non-vertical profiles. Sulphur hexafluoride (SF_6) was used as etching gas, as it achieves a high etching rate, and octafluorocyclobutane (c-C_4F_8) was used as passivation gas. Although, originally ICP equipments were developed for deep silicon etching applications, high etching rates can hinder the control of the etched depth due to the required short times to obtain the barcodes. In addition, large scalloping can ruin sub-micron structures. Thus, vertical profiles with low etch rates and without scalloping were obtained by optimizing the ICP process parameters (source and substrate power, chamber pressure, etching times, fluxes of the passivation and etching gases). The non-vertical profile was obtained by removing the passivation gas from the recipe inducing an isotropic etching. By combining these two sequences any code can be made. The number of different codes is limited by the thick and wide dimensions of the silicon dioxide spot mask. Hence, potentially more than 15 bits (equivalent to 32768 in decimal code) could be produced using a 1.5 µm-thick 3 µm-wide spot mask by considering a 1000 Å silicon dioxide etching rate per bit (worst case) and a DRIE aspect ratio of 20:1. However, only few bits 4 or 8 (equivalent to 16 or 256 in decimal code, respectively) would be necessary for our cell cultures labelling. So, the proposed technology satisfies this requirement.

3.5.4 Release of 3D Silicon Barcodes

Once the codes were finished at wafer level, they were released through a large non-vertical

etching (Recipe B) (Figure 3.9).
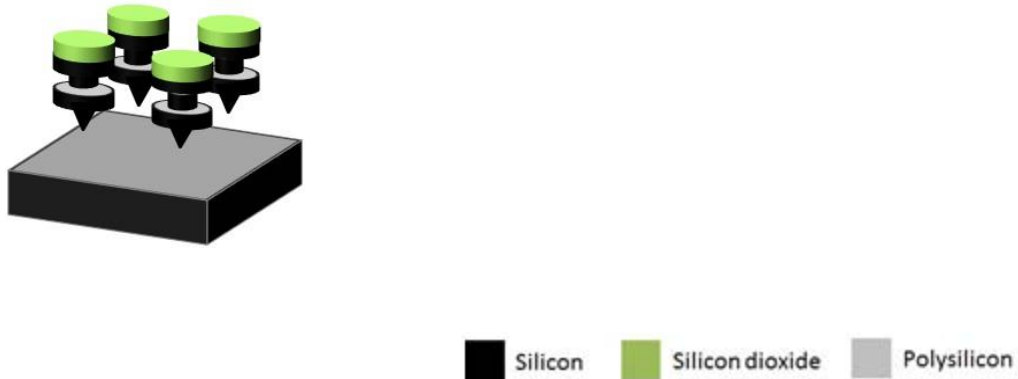
Figure 3.9: Release process of the 3D Silicon Barcodes. The barcodes were finally

released by a long isotropic silicon overetching process.

3.5.5 Collection of 3D Silicon Barcodes

As it was already mentioned in subsection 2.7.2, after the 3D Silicon-based Barcodes were

etched by Recipe B, they were still attached to the silicon substrate due to a weak static friction.

So, the next step was oriented to collect them in suspension.

Firstly, the wafer was divided into small pieces (1 cm x 1 cm) using a diamond tip (Section

3.4.5). Then, each piece of wafer was immersed in a glass beaker, which contained a few

milliliters of 96% ethanol, next a sonicated step was performed and finally, the 3D Silicon

Barcodes were suspended in ethanol, distributed in different Eppendorf's (which contained a

filter to prevent large waste) and collected by centrifugation at 1400 rpm for 5 minutes (Figure 2.7). Collected 3D barcodes can be stored until needed. Before handling them, the Eppendorf's should be centrifuged again and the supernatant extracted. This allows the manipulation of the devices in microliter quantities by using micropipettes.

3.5.6 Physical characterization of 3D Silicon Barcodes

Scanning electron microscopy was used to characterize the fabricated devices. SEM images of the 0101_b barcode at different fabrication stages are shown in Figure 3.10. In addition, SEM images of the fabricated barcodes after their release are shown in Figure 3.11. The obtained results show that fabricated devices maintain perfectly their well-defined shape and homogeneous surface before and after their wafer release.
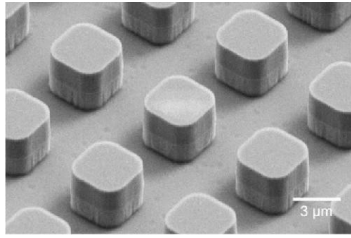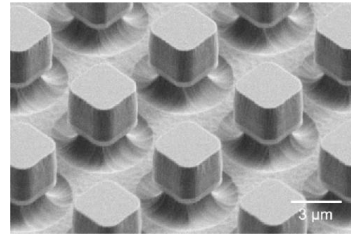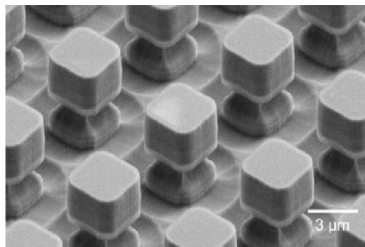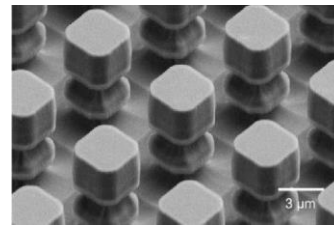
Figure 3.10: Fabrication results of 3D Silicon-based Barcodes. SEM images at different fabrication stages of the code 0101_b. a) Bit1 = 1_b, b) Bit2 = 0_b, c) Bit3 = 1_b and d) Bit4 = 0_b.
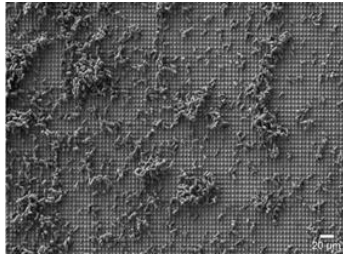
a   b
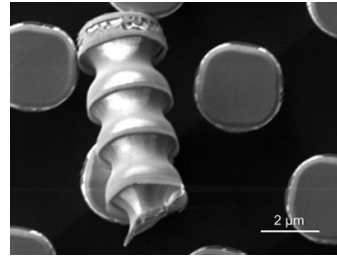
Figure 3.11: 3D Silicon-based Barcodes after their wafer release. SEM images of the released barcodes. The last etching process defines a conical structure at the end of the code that can be used as a start marker to indicate its correct readout

3.6 2D PolySilicon-based Barcodes in living human macrophages

(Biological experiments were performed in partnership with the group of Dr. Carme Nogués of the Department de Biologia Cel·lular, Fisiologia i Immunologia, Universitat Autònoma de Barcelona)

The next section shows the applicability of these barcodes as biological labels for cell tracking, as these devices can follow individual cells for up to ten days in culture and recording their locomotion. However, to track individual cells during several days in culture, and use an optical microscope, the codes have to fulfill some biological, optical, and fabrication requirements.

From the technological point of view, the fabrication process of 2D barcodes allows to manufacture different binary codes through a single DRIE step, simplifying and cheapening the production process. For this reason, finally 2D polySilicon-based Barcodes were chosen for the biological experiments.

3.6.1 Cellular uptake by phagocytosis

Barcode cellular uptake was analyzed in Human Macrophages, as these cells were chosen because of their capacity to phagocyte large pathogens or even polystyrene particles at least up to 15 μm [17]. Using an inverted optical microscope, barcodes were localized inside living macrophages and they could be clearly read. As barcodes have been designed with a reading start marker, no interpretation mistakes occurred.

a

b
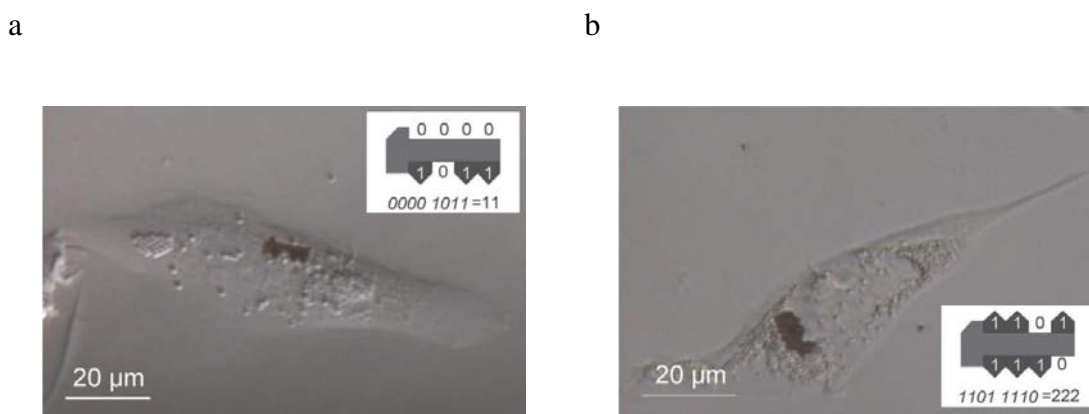
Figure 3.12: Inverted light microscopy images of two Human Macrophages with an internalized 2D polySilicon-based Barcode in their cytoplasm. a) Barcode 11_d and b) barcode 222_d. A schematic view of both barcodes is shown in the insets.

The flat shape of cells on living cultures facilitates the flat-placed position of the barcodes, allowing their clear identification (Figure 3.12). Only in a very few cases the barcodes were positioned close to 90° in a tilted angle regarding the focal plane and could not be read.

3.6.2 Cell viability and cytotoxicity assays

Both biocompatibility and cell viability (crucial biological requirements of the barcodes) were tested in this study. Macrophages carrying a polySilicon barcode were studied during 10 days to evaluate cell survival (Figure 3.13). The initial macrophage population (n = 38 cells) was reduced down to 20.0% (8 cells) after 10 days in culture. This decrease is similar to that observed in control cultures without polySilicon barcodes (21.1%; n = 70 cells).
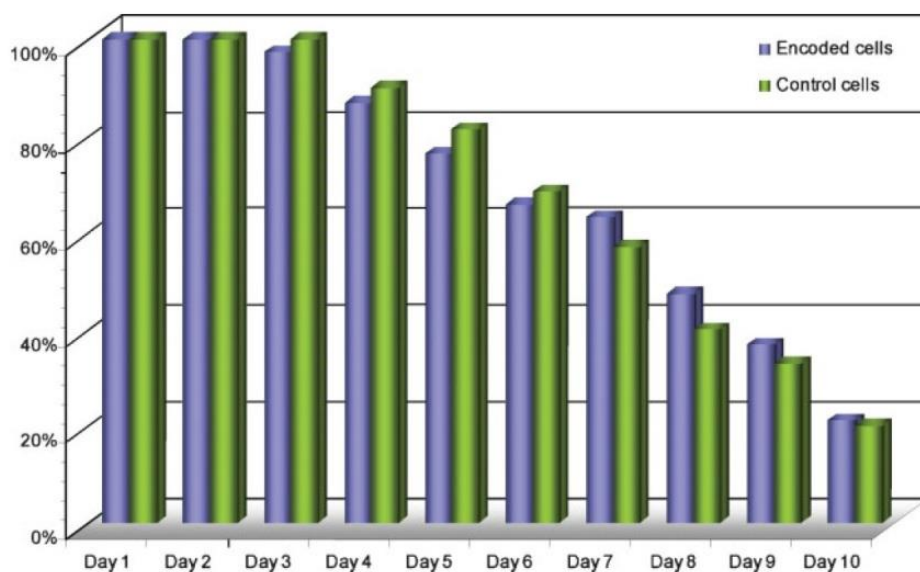
Figure 3.13: Cell viability test of the living Human Macrophages with internalized 2D Silicon barcodes. Cell viability of encoded and control macrophages during 10 days in culture. No statistically significant differences in the survival rates were found between the two populations.

3.6.3 Validation of 2D polySilicon Barcodes for cell labeling and tracking

Finally, a single cell tracking test was performed in 38 different macrophages carrying a polySilicon barcode (code = 158_d). Macrophages were cultured on reticulated coverslips to record the coordinates of each cell carrying a barcode (See Appendix D). This system allowed localizing and identifying a particular cell every 24 h during 10 days despite of its changing morphology during cell locomotion. Each cell was tracked individually and its movement was recorded. From the obtained data, the trajectory of 8 individual cells that survived up to 10 days was drawn, and the partial or total distance was measured (Figure 3.14 and 3.15).
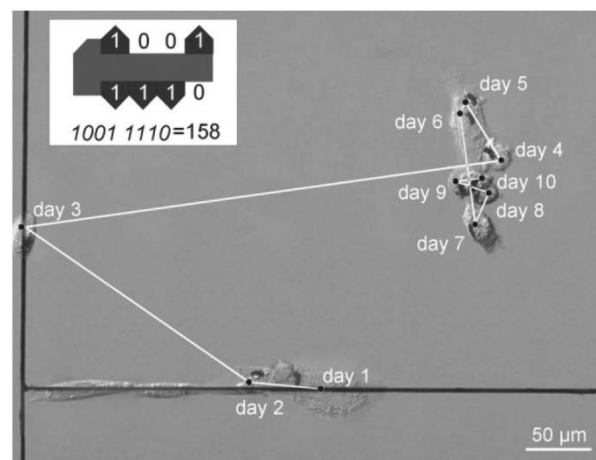
Figure 3.14: Daily movements of an encoded macrophage during 10 days in cell culture. Cell trajectory (white line) overlaying an optical image of a living macrophage. The encoded macrophage (code: 158_d) has traveled a total of 697 μm throughout 10 days.
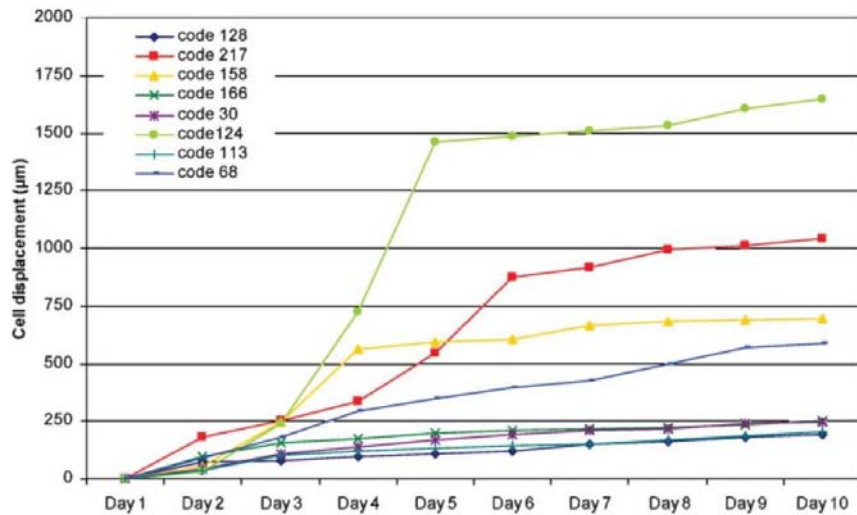
Figure 3.15: Daily movements of eight encoded Human Macrophages. Eight different macrophages with a barcode in their cytoplasm during 10 days in culture

3.7 Discussion and Conclusions

This chapter shows the technological development of two types of Silicon Barcodes obtained through silicon microtechnologies and developed with the main objective of labelling and tracking single living cells.

Firstly, the 2D polySilicon-based Barcodes were designed with 10.0 μm length, 6.0 μm width, allowing the production of more than 8M/wafer devices with 256 binary different codes, using a unique mask pattern. Taking advantage of the silicon microtechnologies, the fabrication process was performed. The designed barcodes can be visualized and their patterns easily recognized under a light microscope using a 60X objective (the maximum magnification routinely used in cell culture laboratories). Eventually, the obtained barcodes maintained perfectly their shape and presented a homogenous and high robust surface even after their wafer release. A possible

shortcoming of the 2D barcodes could reside in the code identification when it is used with cells in suspension, needing the barcodes a flat position for the correct reading of the binary code.

In contrast, the reported 3D Silicon-based Barcodes allow the production of more than 150M/wafer devices with a unique binary code using a single mask pattern. Besides, these 3D Silicon-based Barcodes are less sensitive to the spatial orientation of the codes with respect to the reader, which demonstrates the practicability to develop many deep reactive ion etching processes (DRIE). In addition, the etch profiles of these structures can be set by changing the etching conditions (enabling the production of millions of identical codes), meanwhile for the 2D barcodes will be necessary to change the mask pattern.

The main advantages of the proposed barcodes are well-controlled shape and dimensions, reproducibility, robustness, large enough to allow their readout by fluorescence and non-fluorescence light microscopes and small enough to be internalized inside living cells.

From the biological point of view, when survival rates of encoded (with an internalized barcode) and control Human Macrophages were compared, no significant differences were found in either the first five days in culture, or in the last five days (difference between proportions test). Hence, these results demonstrate that the reduction in viability in Human Macrophages can be attributed to the normal behavior of these cells after differentiation (attach to the substrate, stop proliferating, and finally die) [18] and not to the presence of the barcodes. In addition, it is worth mentioning that no UV light or laser beam was employed during the biological experiments to illuminate the barcodes. So that, DNA cell damage was prevented and cells were not disturbed.

Cells are tracked using manual or automated detectors coupled to sophisticated software [19, 20], which allows the cell monitoring for one or two days. The advantage of using Silicon-based Barcodes, is that no special equipment is needed, other than an inverted light microscope, that is typically found in all cell biology laboratories. As step forward in this line of work, an automatic code identification system could be designed in the near future as an improvement in the barcode readout system. Finally, using the microtechnology techniques presented in this chapter, a reduction in the barcode dimensions to submicrometer range could be envisaged; the limiting factor is only the resolution of present optical microscopes.

Bibliography

[1] N. H. Finkel, X. Lou, C. Wang, L. He. Anal. Chem. 76 (19), 352A (2004)

[2] D. B. Weibel, W. R. DiLuzio, G. M. Whitesides. Nat. Rev. Microbiol. 5, 209 (2007)

[3] M. Y. Han, X. H. Gao, J. Z. Su, S. Nie. Nat. Biotechnol. 19, 631 (2001)

[4] S. R. Nicewarner-Pena, R. G. Freeman, B. D. Reiss, L. He, D. J. Pena, I. D. Walton, R. Cromer, C. D. Keating, M. J. Natan. Science 294 (5540), 137 (2001)

[5] A. Bulbarello, S. Sattayasamitsathit, A. G. Crevillen, J. Burdick, S. Mannino, P. Kanatharana, P. Thavarungkul, A. Escarpa, J. Wang. Small 4, 597 (2008)

[6] F. Cunin, T. A. Schmedake, J. R. Link, Y. Y. Li, J. Koh, S. N. Bhatia, M. J. Sailor. Nat. Mater. 1, 39 (2002)

[7] P. Georges, P. A. Curmi, F. Treussart. Small 4, 2236 (2008)

[8] B. K. Oh, J. M. Nam, S. W. Lee, C. A. Mirkin. Small 2, 103 (2006)

[9] J. R. McCarthy, F. A. Jaffer, R. Weissleder. Small 2, 983 (2006)

[10] J. Voldman. Nat. Mater., 2, 433 (2003)

[11] E. Tasciotti, X. W. Liu, R. Bhavane, K. Plant, A. D. Leonard, B. K. Price, M. M. C. Cheng, P. Decuzzi, J. M. Tour, F. Robertson, M. Ferrari. Nat. Nanotechnol. 3, 151 (2008)

[12] E. Fernández-Rosas, R. Gómez, E. Ibañez, L. Barrios, M. Duch, J. Esteve, C. Nogués, J. A. Plaza, Small 5, 2433 (2009)

[13] F. Kuribayashi, S. Tsuruta, T. Yamazaki, H. Nunoi, S. Imajoh-Ohmi, S. Kanegasaki, M. Nakamura. Genes to Cells 13 (12), 1249 (2008)

[14] R. Abdolvand, F. Ayazi. Sensors and Actuators A 144, 109 (2008)

[15] J. A. Plaza, A. Sánchez, K. Zinoviev, F. Pérez-Murano, J. Bausells. Microelectron. Eng. 84 (5), 1132 (2007)

[16] F. Laermer, A. Schilp. Anisotropic etching of silicon substrates using a polymerisation process in between etching stages to protect lateral edges of the etched shape, Patent WO9414187-A, DE4241045-C.

[17] C. Foged, B. Brodin, S. Frokjaer, A. Sundblad. Int. J. Pharm. 298, 315322 (2005)

[18] S. Tsuchiya, Y. Kobayashi, Y. Goto, H. Okumura, S. Nakae, T. Konno, K. Tada. Cancer Res. 42, 1530 (1982)

[19] O. Debeir, I. Camby, R. Kiss, P. Van Ham. C. Decaestecker. Cytometry Part A, 60A, 2940 (2004)

[20] K. Li, M. Chen, T. Kanade. Medical Image Computing and Computer-Assisted Intervention MICCAI 2007, Pt 2, Proceedings 4792, 295302 (2007)

Chapter 4

Intracellular PolySilicon Chips for biomolecular recognition

4.1 Abstract

The miniaturization techniques in microelectronics and micro- and nanoelectromechanical systems (MEMS and NEMS) allow the fabrication of even more small chips mostly made of semiconductor materials. These complex structures can be mass produced with nanometer precision and high control over the shape (even reaching under living cell dimensions) and at low cost. In addition, the chemical properties of silicon enable the silicon-made devices to be easily modified, allowing them to be used in several applications such as advanced molecular recognition [1]. Furthermore, many different materials (semiconductors, metals, insulators) can be integrated into the same chip with precise dimensions and geometries, enabling even more advanced applications.

In order to open new perspectives in this line of research, in this chapter the ability to produce bio-functionalized silicon-based intracellular chips (ICCs) with dimensions under the 3 µm is shown. Once they are completely manufactured, the different steps to reach an efficient chip collection, manipulation and cell internalization, are also shown.

Eventually, the ability of these intracellular chips to be used as biomolecular sensors could be also proved by the observation of the hydrolysis of the fluorescein diacetate (CFDA), which is functionalized on the chip surfaces, by the intracellular esterases. Two cellular models, *Dictyostelium Discoideum* (Dicty) and *Human HeLa* cells are chosen to be tested, as the main objective is to test the biomolecular potential of ICCs. Furthermore, the demonstration that these small chips can be performed with more than one material

and their ability to be nanostructured is presented, allowing in a near future the integration of electronic and mechanical parts at ICC-scale level (a key step for the production and use of innovative intracellular silicon-based micro- and nanochips).

4.2 Introduction

Recent advances in micro- and nanotechnologies have enabled microelectromechanical systems and nanoparticles to be used as interactive devices in cell biology [2-7]. Even though silicon MEMS, based on photolithographic processes, exhibit high performance and versatility [8] their uses have been limited to extracellular applications, that is, cell biomolecular recognition [9], manipulation [10], mechanical analysis [11, 12], weighing [13] and positioning [14, 15]. In contrast, reported micro- and nanoparticles, characteristically formed or produced by chemical synthesis, have been used for intracellular applications [16].

As is reported in Chapter 1, an ICC is a silicon based-chip completely manufactured of Silicon or polySilicon. Thanks to microelectronic fabrication techniques, the combination of different materials and structures in the same chip is possible. In addition, the control of the dimensions and shapes into the same batch of devices is also possible. Accordingly, microelectronic technologies are highly-suitable candidates for the fabrication of these ICC devices, as they provide the possibility of growing or depositing several materials as semiconductors, insulations and metals with high precision. Furthermore, the well-known surface chemistry of the used materials, and their well-known biocompatible characteristics, enable their use in cell biology applications with a solid technology background.

In this chapter, silicon-based intracellular chips (ICCs) are successfully produced, collected, internalized inside living cells, and used as intracellular biomolecular sensors. In addition, a new line of research is open, as these small chips can be composed of more than one material and can be nanostructured, enabling the integration of electronic and mechanical parts at ICC-scale level.

4.3 Concept

The concept of this device is to obtain biochemically functionalized ICCs as a first step towards biochemical intracellular chips. The vertical dimensions of ICCs are fixed with nanometer precision by the thickness of a polySilicon layer, whereas lateral dimensions are fixed with micro- and submicrometric precision by the photolithographic techniques.

4.4 Design of Biofunctional Intracellular Chips

The same ICC design described in section 2.4.1 was used for the intracellular polySilicon chips for biomolecular recognition. The external dimensions were fixed to 3 µm diameter and a 0.5 µm thickness (Figure 2.1). In the same way, their dimensions limit the maximum number of enable devices that can be manufactured at the same time (Figure 2.3), and the maximum dimensions should allow their cell internalization being big enough to be easily visualized using optical microscopes.

4.5 Wafer layout for the fabrication of Biofunctional Intracellular Chips

Wafer dimensions (section 2.5) limit the maximum number of enabled devices to be manufactured. In this case, 3 µm x 3 µm devices spaced 3 µm distributed on a 100-mm wafer were obtained. The fabrication yield was more than 150 million ICC devices contained in a single wafer (Figure 2.3).

4.6 Technology development for the fabrication of Biofunctional Intracellular Chips at wafer level

As it was already mentioned in section 2.6.1, ICCs were fabricated combining photolithographic and micromachining technologies with polySilicon fabrication techniques. This approach allows an accurate control of the device shape and dimensions at the micrometer or even sub-micrometer level. The fabrication process was based on the combination of a 0.5 µm-polySilicon device layer (deposited by LPCVD) and a 1 µm-silicon oxide sacrificial layer (deposited by PECVD) coated onto a 100-mm silicon wafer, (Figure 4.1). A 1.2 µm-thick photoresist layer (*Fujifilm*) was spun and irradiated (*Karl-Suss MA6 contact aligner*) through a chromium mask. The radiated area was dissolved and the chips were patterned by vertical dry etching (*Alcatel A601*) using a modified Bosh process recipe (Section 3.5.1). The photoresist was removed by plasma etching (*Tepla 300-E*) and the chips were released by the etching of the silicon oxide sacrificial layer in vapors of hydrofluoric acid (49% HF).
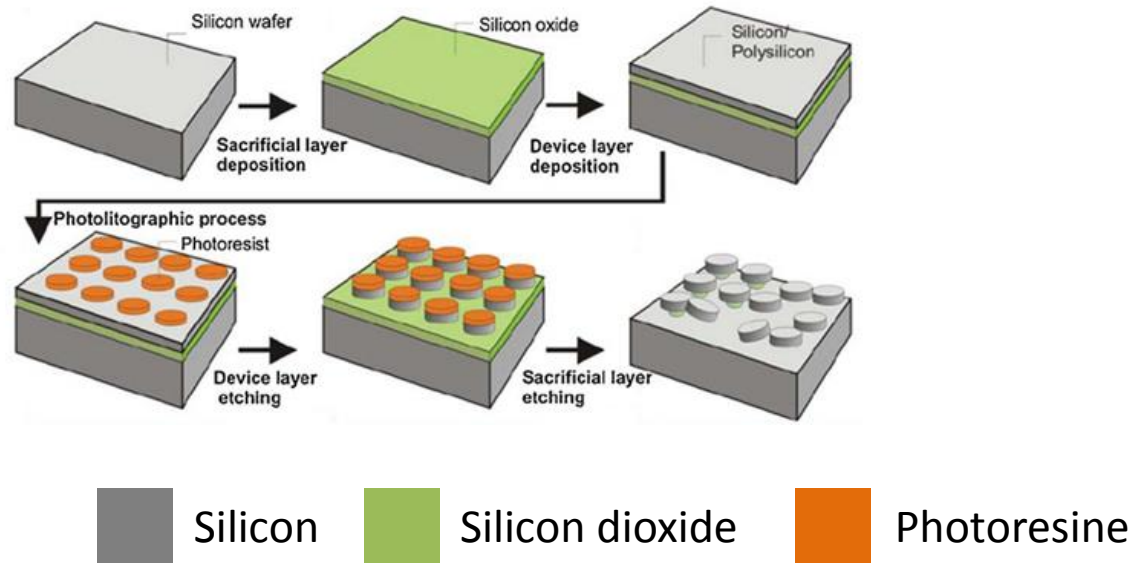
Figure 4.1: Biofunctional Intracellular Chips fabrication process. A silicon wafer was used as starting material, followed by a silicon oxide deposition (sacrificial layer), then by a polySilicon deposition (device layer). Next, the ICCs were obtained combining the photoresist deposition with a photolithographic step. Then, the device layer was etched to pattern the chips. Finally, after photoresist removal, the chips were released from the wafer by the SiO_2 sacrificial layer etching.

4.7 Technology development for the release and collection of Biofunctional Intracellular Chips

As it was mentioned in section 2.7, once the ICCs manufacturing process has finished (Figure 4.2a), the wafer was divided into small pieces (1 cm x 1 cm) by a diamond tip. Each piece was placed into a Teflon holder, where it was subjected to 49% HF vapors for 40 minutes. These HF vapors have the ability to etch the silicon oxide sacrificial layer and in this way the ICCs could be easily released from the wafer substrate (Figure 4.2b-c). The collection process started with

115

the immersion of a piece of wafer into a glass beaker, containing 96 % ethanol. Subsequently, a sonicated step was performed, as allows the final released of the devices into the ethanol beaker. Once the ICCs were suspended in ethanol, they were collected in several Eppendorf´s. The devices were concentrated by 5-µm filter rating (*Hydrophilic PVDF, Millipore*) and centrifugation at 1000 rpm for 5 minutes (*MiniSpin Plus*). Finally, they were stored for subsequent studies. After that, before handling the ICCs, the Eppendorf´s were again centrifuged and the supernatant extracted, this process allows the manipulation of the devices in microliter quantities by using micropipettes.

a   b   c
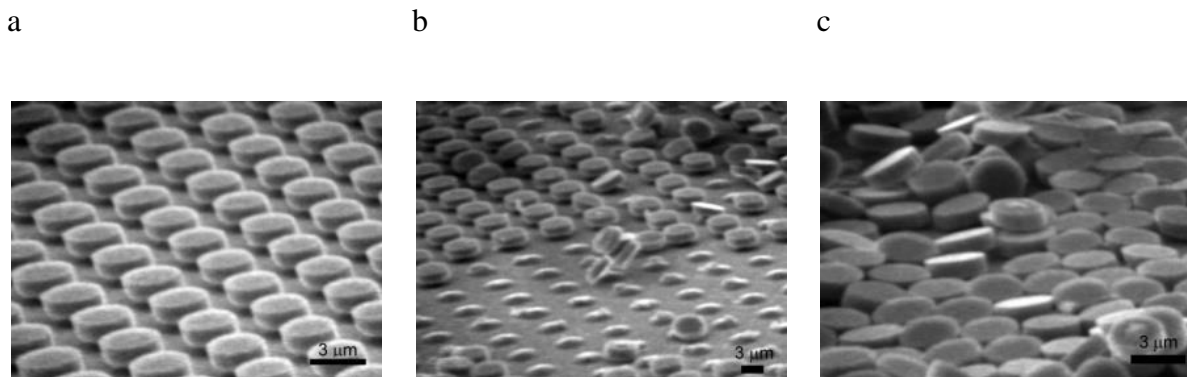
Figure 4.2: Release and collection processes of the Biofunctional Intracellular Chips. Scanning electron microscopy images of, a) ICCs after the dry etching, b-c) ICCs after the HF wet etching process. Scale bar = 3 µm.

4.8 Chemical functionalization of the Biofunctional Intracellular Chips

(Performed in partnership with the Instituto de Investigaciones Químicas y Ambientales de Barcelona IQAB-CSIC)

ICCs were cleaned with a mixture of HNO_3/MeOH (3:7), dimethylformamide (DMF):milliQ H_2O (7:3, 3 x 1 mL) and with ethanol (3 x 1 mL). To activate their surface, ICCs were incubated in a 1% KOH/ethanol solution (10 min), washed with DMF:milliQ H_2O (7:3, 3 x 1 mL) and with anhydrous ethanol (3 x 1 mL). Surface amination was achieved by incubation in 2.5% (v/v) 3-aminopropyl-trimethoxy silane (3 h/RT) followed by washing with anhydrous ethanol (3 x 1 mL) and with anhydrous DMF (3x1 mL). A 1 mM solution of fluorescein diacetate isothiocyanate in anhydrous DMF was added and the chips were left to react for 12h at RT in the dark. Finally, ICCs were washed with anhydrous DMF (3x1 mL) and stored in methyl tert-butyl ether. The used solvents were filtered with 0.45-mm filters and centrifugations were carried out for 10 min at 1500 g (10 °C).

4.9 Biofunctional Intracellular Chips in living *Dictyostelium Discoideum* and *HeLa* cells

(Performed in partnership with the Centro de Investigaciones Biológicas CIB -CSIC, for more information see Experimental Section-Appendix A, Reference 12)

4.9.1 Cellular uptake by phagocytosis and lipofection

PolySilicon devices with lateral dimensions of 3 µm-diameter and 0.5 µm-thickness were selected to be placed inside living cells. Cells from the social organism *Dictyostelium Discoideum* and *Human HeLa* cells were chosen. We took advantage of the phagocytotic capacity of Dicty and Dicty amoebas with ICCs at a ratio of 0.51 ICC/cell were incubated. Observation under optical light microscopy and confocal laser scanning microscopy (CLSM) showed that ICCs were efficiently internalized by healthy *D. Discoideum* (Figure 4.3a and c, and Figure 4.4a). Non-phagocytic cells such as *HeLa* cells, can internalize particles by endocytosis [27]. Preliminary experiments incubating *HeLa* cells with polySilicon ICCs (0.51 ICCs/cell) gave low yields of internalized ICCs. Consequently, lipofection techniques [18] were applied to obtain higher rates of ICC-containing cells. After incubating liposomes containing polySilicon ICCs with *HeLa* cells, we observed a 50% increase in the number of ICCs-containing cells, reaching an average of 25% and used lipofectamine here after. ICCs internalization in *HeLa* cells was observed by optical light microscopy and CLSM (Figure 4.3b and d, Figure 4.4b). To confirm ICCs internalization into the cytoplasm of *HeLa* cells a SEM-FIB station (Figure 4.3e-h) was used [19, 20]. This equipment allowed the machining (with nanometer precision) of fixed cells to verify the internalized ICCs, allowing high-resolution imaging by scanning electron microscopy (SEM)
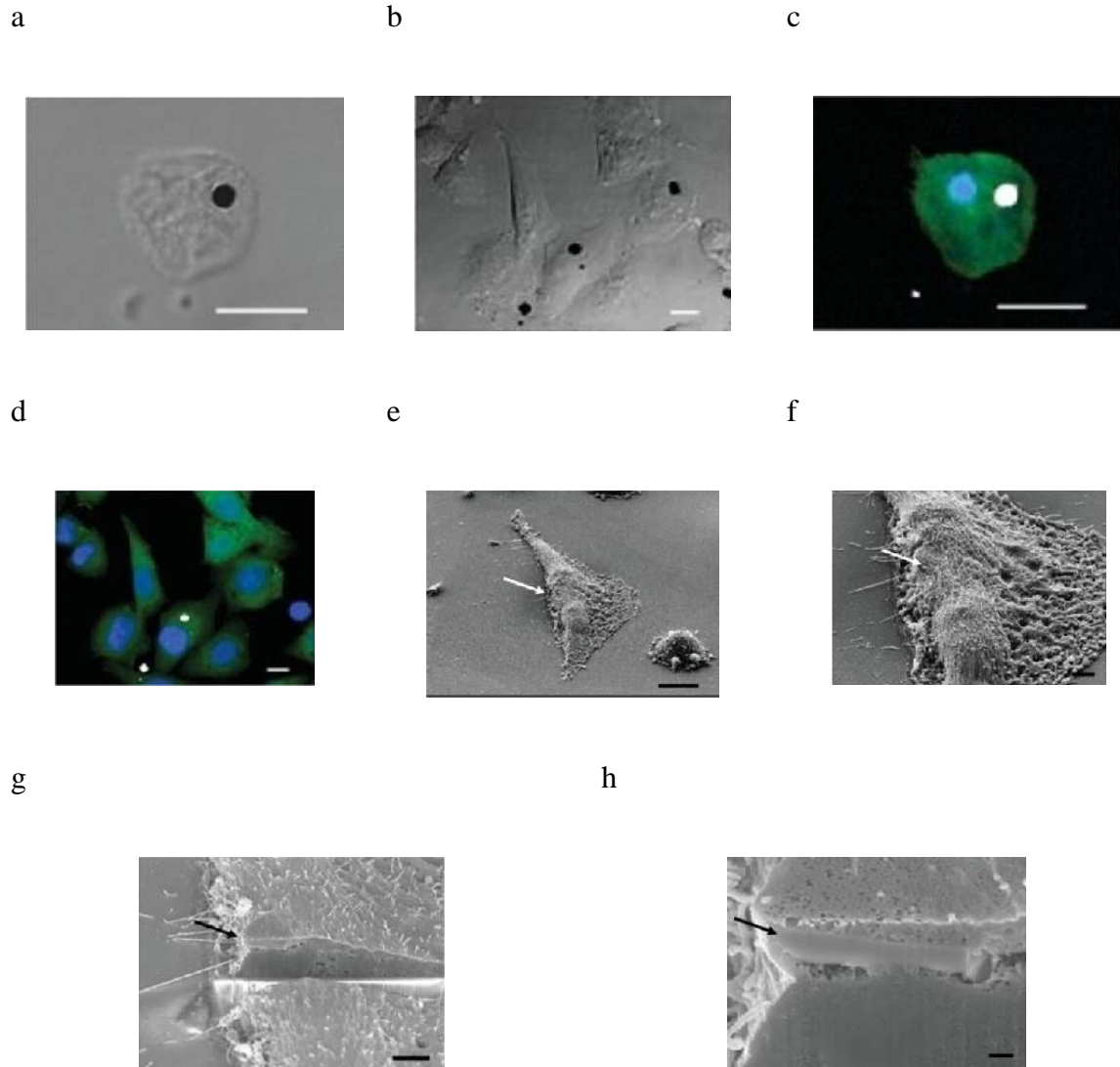
Figure 4.3: Cell internalization of polySilicon Chips in eukaryotic cells. ICCs appeared as black spots in optical-light microscopy transmission images (a,b) and in white in confocal laser reflection images (c,d). GFP-expressing *D. Discoideum* (c) and *HeLa* cells loaded with the vital CFDA dye (d) showed ICCs inside their cytoplasms. SEM images of a *HeLa* cell containing ICCs (e,f). SEM image of a *HeLa* cell nanomachined by FIB, where the ICCs is located inside the cell (g,h). White and black arrows indicate the position of the ICCs. Scale bar in (a-e) = 10 µm; (f,g) 3 µm; (h) 0.5 µm

a
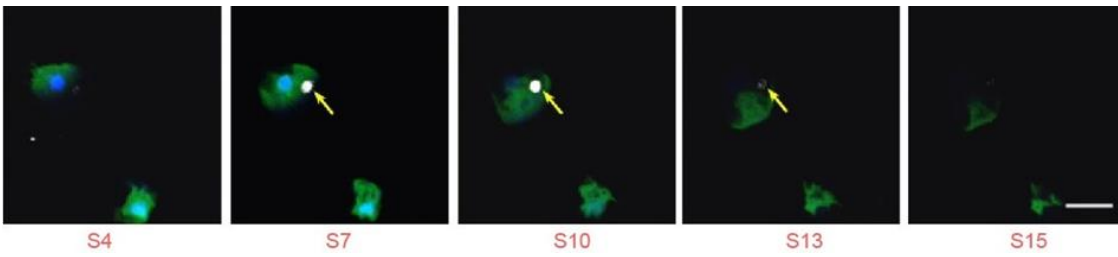
b
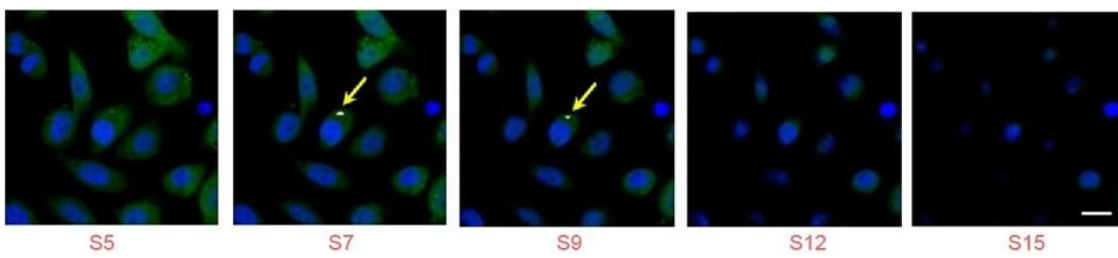
Figure 4.4: ICCs cytotoxicity in *D. Discoideum* and *HeLa* cells. Non-consecutive z

stacks taken by CLSM every 0.5 µm of (a) *D. Discoideum* (b) and *HeLa* cells. ICCs

appear as white spots and the nuclei are shown in blue. Yellow arrows indicate the

ICCs position. Confocal sections demonstrate that ICCs are inside the cytoplasm, as

ICCs appear only in the middle sections (S7-S13 in A and S7-S9 in B). Scale bar = 10

µm.

4.9.2 Cell viability and cytotoxicity assays

To assess if the ICCs-containing *D. Discoideum* and *HeLa* cells were healthy and alive after ICCs internalization, a vital dye fluorescein diacetate (CFDA) and time-lapse microscopy were used. Interaction of CFDA with active intracellular esterases hydrolyzes the acetate groups, producing fluorescein emission, which can be observed under a fluorescent light. Alive ICC-containing *HeLa* cells and *D. Discoideum* display green fluorescence (Figure 4.4a and Figure 4.4b). Time-lapse microscopy also showed healthy ICCs-containing *D. Discoideum* and *HeLa* cells (See videos V1 and V2 in DOI: 10.1002/smll.200901041/abstract#footer-support-info).

In addition, to evaluate the effects of polySilicon ICCs on long-term cell viability, ICC-containing *HeLa* cells were maintained for up to 7 days in proliferating cultures that resulted in confluent monolayers. After 3 and 7 days in culture, cell viability was assessed by loading *HeLa* cells with CFDA before fixation. Healthy living cells containing ICCs were observed 3 and 7 days after ICC lipofection (Figure 4.5a and b). Cytotoxicity was further evaluated with Propidium iodide (PI). Over 90% of cultured *HeLa* cells remained viable 7 days after lipofection and the same percentage of viable cells was observed for the ICC-containing *HeLa* cell population (Figure 4.5c and d).
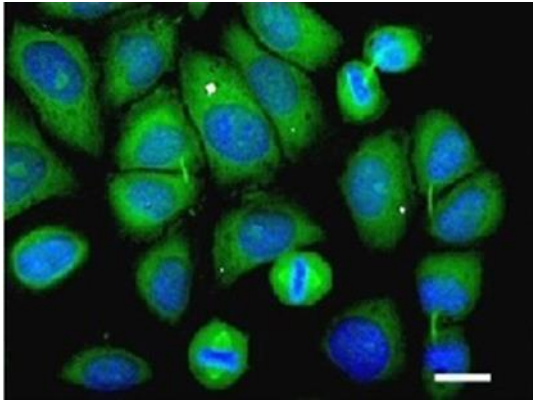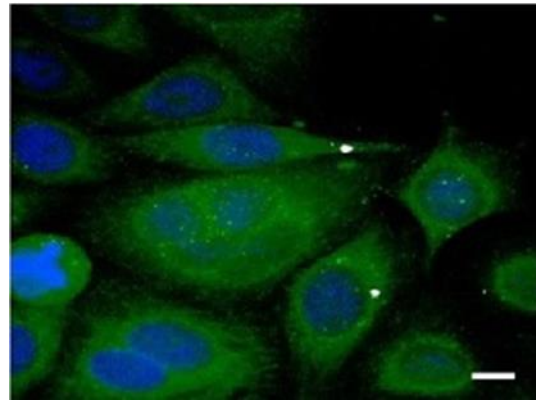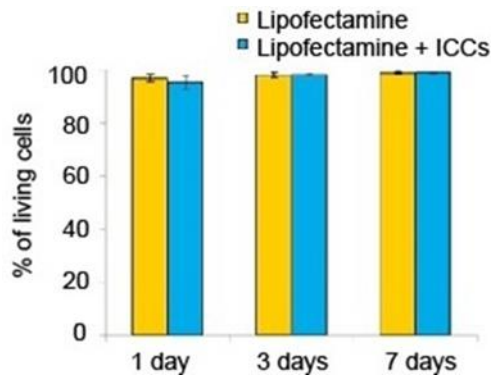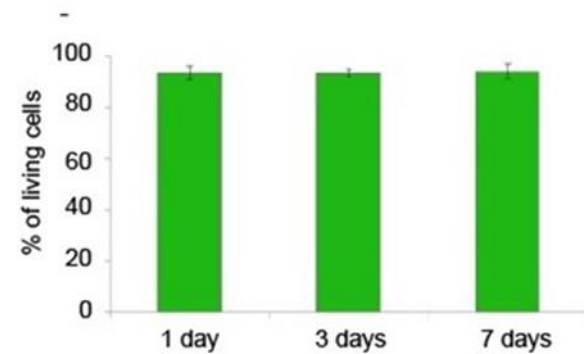
Figure 4.5: *HeLa* **cells remain viable several days after lCCs internalization.** Maximal confocal projections of cultured *HeLa* cells for (a) 3 and (b) 7 days after ICC lipofection. Green cytoplasm corresponds to viable cells that hydrolyze CFDA and white dots correspond to ICCs. Nuclei are shown in blue. Scale bar = 10 μm. (c, d) Graphs show *HeLa* cell culture viability measured by PI exclusion in cell cultures 1, 3 and 7 days after lipofection. (c) Total cell culture viability and (d) cell viability in the ICCs-containing cell population (d). The average of independent experiments is shown.

4.10 Validation of the Biofunctional Intracellular Chips for biomolecular recognition

(Performed in partnership with the Centro de Investigaciones Biológicas, CIB-CSIC)

After establishing that ICCs were not toxic to the cells, ICCs were derivatized with the same vital dye CFDA and delivered them to D. *Discoideum* and *HeLa* cells. Functionalized ICCs inside *D. Discoideum* and *HeLa* cells emitted green fluorescence, demonstrating that intracellular silicon chips can be used for biochemical detection (Figure 4.6). CFDA derivatized ICCs showed green fluorescence inside *HeLa* cells after 3 and 7 days in culture. This observation provides a proof of concept for measuring intracellular biomolecular parameters and opens an important venue for future molecular recognition inside living cells.

a   b   c   d
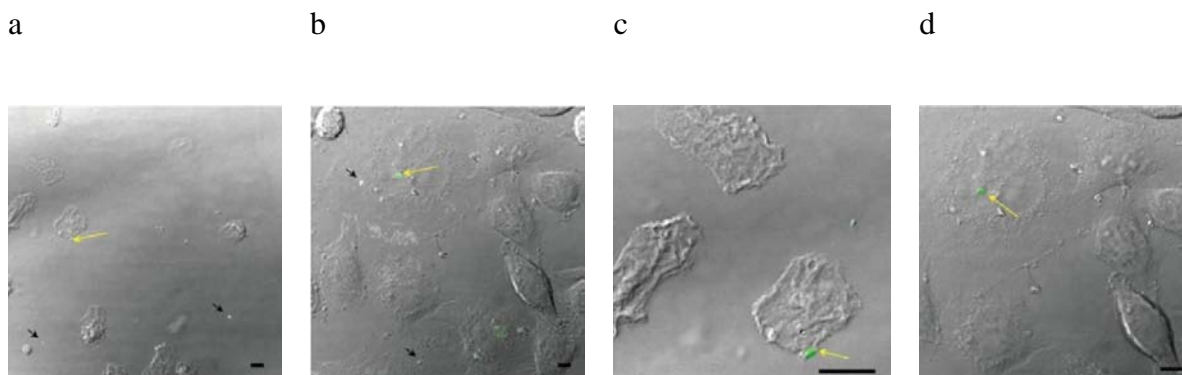
Figure 4.6: CFDA-derivatized Intracellular Chips interact with the cell cytoplasm. (a, c) *D. Discoideum* and (b, d) *HeLa* cells show intracellular ICCs with green fluorescence (yellow arrow). (a, b) Extracellular ICCs do not display fluorescence and appear as white dots (black arrow). (c) Zoom of *D. Discoideum* and (d) *HeLa* cells show functionalized ICCs. Images are maximal confocal projections taken with CLSM. Scale bar = 10 μm.

4.11 Silicon micromachining opportunities for future perspectives of Intracellular Silicon Chips

The combination of photolithographic and micromachining technologies with silicon-based fabrication techniques (described at section 4.6, and when is integrated with different materials and nanomachined techniques), provides the opportunity of created unique small three-dimensional structures for advanced devices. Therefore, to demonstrate the versatility of this technology, the integration of different materials in a single ICC and their nanostructuring capabilities were studied.

First, an ICC composed of a 3 μm x 3 μm misaligned platform of polySilicon and gold (Figure 4.7a) was fabricated by photolithographic processes. This technique allows precise dimensions and geometries of the two materials. Second, it is also worth mentioning that ICCs can be nanomachined in three dimensions using other common microelectronic techniques. For instance, a nanocoil, which can be defined by a Focused ion Beam (FIB) milling (Figure 4.7b).
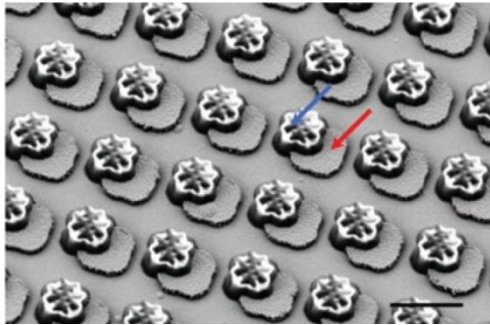
a   b
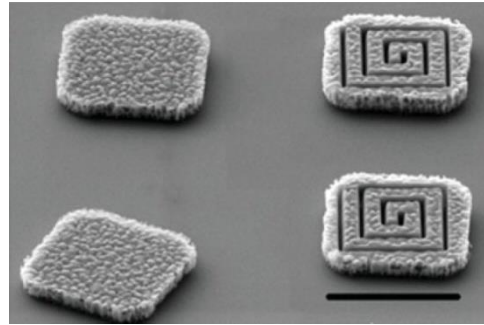
Figure 4.7: Future perspectives of Intracellular PolySilicon Chips. a) SEM image of ICCs made of two misaligned materials: a polySilicon square platform (red arrow) attached to a gold platform (blue arrow). b) SEM image of 3 µm x 3 µm x 0.5 µm polySilicon ICCs before (left) and after (right) create a 3D coil nanostructure by FIB nanomachining. Scale bar = 3 µm.

4.12 Discussion and Conclusions

The technology developed to fabricate biochemical-funtionalized polySilicon Intracellular Chips was reported in this chapter. The miniaturized chips were designed combining photolithographic and micromachining technologies with polySilicon fabrication techniques to allow their posterior introduction inside living cells. The fabrication process was based on standard techniques used in semiconductor and MEMS industries. Intracellular chips were designed, tested and fabricated, made of polySilicon, with 3 µm in diameter and with 0.5 µm in thickness. Technology allowed the manufacture of more than 170 million of chips on a 100 mm-wafer. An efficient process to release the intracellular chips out of the substrate, based on the use of HF vapors for silicon oxide sacrificial-layer etching, was applied and

adapted to the release of the obtained devices. This method allowed an easy and safe procedure. A collection process was also used, this process was composed of three steps; sonication, centrifugation and concentration, which allowed an easy handling and storage of ICCs.

Our results show that silicon-based Intracellular Chips can be phagocyted by living *D. Discoideum* and lipofected by *HeLa* cells, without interfering with cell viability. Furthermore, chemically functionalized intracellular chips could be used as intracellular biomolecular sensors since they can interact with the cell cytoplasm. Intracellular chips have similar dimensions to many synthesized micro- and nanoparticles but they have the advantages of silicon-chip technology. Intracellular chips also offer high flexibility and versatility in shape and size and they can be nanostructured in three dimensions and be integrated with several materials (semiconductors, insulators, metals) at chip-scale level.

In addition, nowadays, there is huge interest in biophysical single-cell properties. Consequently, compared to synthesized nanoparticles, silicon-based nanostructured devices can address the measurement of intracellular mechanical properties. We believe that our work makes important progresses towards functional intracellular NEMS. The objective for further experiments will be the miniaturization of electromechanical devices in combination with cytotoxicity studies for each specific device and cell lines.

In the near future, silicon-based micro- and nanodevices will permit the characterization, quantification, and *in vivo* real-time monitoring of cellular events inside a single cell. Where, the use of engineered Intracellular Chips as intracellular biomolecular sensors inside living cells constitutes a real challenge.

Bibliography

[1] J. Fritz, M. K. Baller, H. P. Lang, H. Rothuizen, P. Vettiger, E. Meyer, H-J. Guntherodt, C. Gerber, J. K. Gimzewskj. Science 288, 316 (2009)

[2] M. Ferrari. Nat. Rev. Cancer 5, 161 (2005)

[3] G. A. Silva. Nat. Rev. Neurosci. 7, 65 (2006)

[4] H. Andersson, A. Van den Berg. Curr. Opin. Biotechnol. 15, 44 (2004)

[5] L. Bousse. Sens. Actuators B. 34, 270 (1996)

[6] G. M. Whitesides. Nat. Biotechnol. 21, 1161 (2003)

[7] D. B. Weibel, W. R. DiLucio, G. M. Whitesides. Nat. Rev. Microbiol. 5, 209 (2007)

[8] J. Voldman. Nat. Mater. 2, 433 (2003)

[9] G. Shekhawat, S. H. Tark, V. P. Dravid. Science 311, 1592 (2006)

[10] C. C. Striemer, T. R. Gaborski, J. L. McGrath, P. M. Fauchet. Nature 445, 749 (2007)

[11] G. Bao, S. Suresh. Nat. Mater. 2, 715 (2003)

[12] S. E. Cross, Y. S. Jin, J. Rao, J. K. Gimzewski. Nat. Nanotechnol. 2, 780 (2007)

[13] T. P. Burg, M. Godin, S. M. Knudsen, W. Shen, G. Carlson, J. S. Foster, K. Babcock, S. R. Manalis. Nature 446, 1066 (2007)

[14] H. Lee, Y. Liu, D. Ham, R. M. Westervelt. Lab Chip 7, 331 (2007)

[15] D. S. Gray, J. L. Tan, J. Voldman, C. S. Chen. Biosens. Bioelectron. 19, 1765 (2004)

[16] S. K. Murthy. Int. J. Nanomed. 2, 129 (2007)

[17] S. E. A. Gratton, P. A. Ropp, P. D. Pohlhaus, J. C. Luft, V. J. Madden, M. E. Napier, J. M. DeSimone. Proc. Natl. Acad. Sci. USA 105, 11613 (2008)

[18] V. Ciccarone, Y. Chu,K. J. P. Pichet, P. Hawley - Nelson, K. Evans, L. Roy, S. Bennett. Focus. 21, 45 (1999)

[19] M. Milani, M. Ballerini, D. Batani, F. Squadrini, F. Cotelli, C. Lora Lamia Donin, G. Poletti, A. Pozzi, K. Eidmann, A. Stead, G. Lucchini. Eur. Phys. J. Appl. Phys. 26, 123 (2004)

[20] D. Drobne, M. Milani, A. Zrimec, V. Leser, M. Berden. J.Microscopy. 219, 29 (2005)

[21] E. Tasciotti, X. Liu, R. Bhavane, K. Plant, A. D. Leonard, B. K. Price, M. M. Cheng, P. Decuzzi, J. M. Tour, F. Robertson, Ferrari Mauro. Nat.Nanotech.151 (2008)

Chapter 5

A NanoOptoMechanical System (NOMS) for cell mechanics

5.1 Abstract

5.2 Introduction

2.3 Concept

5.4 Preliminary theoretical analysis

      5.4.1 Mechanical analysis

      5.4.2 Optical analysis

5.5 Design of a NanoOptoMechanical System as intracellular Pressure Sensor

5.6 Technology development for the fabrication of the Pressure Sensor at wafer level

      5.6.1 Fabrication technology at wafer level

      5.6.2 Device release and collection

5.7 Specific considerations of the polySilicon nanolayer

      5.7.1 Surface quality of the deposited polysilicon layer

      5.7.2 Fabrication and hermeticity analysis of polysilicon layer

      5.7.3 Polysilicon degradation test

5.1 Abstract

The possibility to measure the pressure value inside a living cell and inside its different components is an unprecedented challenge, because it offers an alternative way to study fundamental processes which involve cell deformation [1]. Nevertheless, most current techniques such as pipette aspiration [2], optical interferometry [3] or external pressure probes [4], use either indirect measurement methods or approaches that can damage the cell membrane. In this chapter a Nano-Opto-Mechanical System (NOMS) small enough to be internalized into a living cell is presented and it is demonstrated to detect pressure changes inside living cells. The NOMS consists of two membranes separated by a vacuum gap to form a Fabry-Pérot resonator (see Appendix C) [5-7], detecting pressure changes that can be quantified from the intensity of the reflected light on its surface. Using this NOMS, extracellular hydrostatic pressure transmitted into *HeLa* cells can be detected, demonstrating that extracellular pressure is transmitted totally to the cytosol of a *HeLa* cell. Moreover, we use this chip to show that cells can endure hypo-osmotic stress without significantly increasing their intracellular hydrostatic pressure.

5.2 Introduction

Scientific interest in the intersection of micro- and nanotechnologies with biology has focused on providing new tools to study fundamental questions in cell biology [8-10]. Fabrication based on these techniques offers the potential to develop integrated devices with nano-sized moving parts [11] and allows new opportunities for the mechanical analysis of cells [12, 13]. However, the use of this kind of devices has been focused on extracellular or invasive techniques [14]. Nevertheless, micro- and nanoparticles can be also internalized inside living cells and be used in numerous studies in cell biology. Furthermore, silicon-based particles have revealed their favorable position in biological imaging and drug delivery because of their inherent biocompatibility [15, 16]. In addition, related to single-cell labelling applications, which were demonstrated at Chapter 3, can be achieved through the use of silicon microchips based on semiconductor technologies [17, 18]. Additionally, using chemical functionalization, microchips could react directly with the intracellular medium (Chapter 4) [19]. In this chapter, a step further is showed, as suspended mechanical sensors for cell mechanics applications are produced.

Existing techniques for the indirect measurement of intracellular pressure include methods that induce a large deformation of the cell by aspiration [2], or methods that detect variations in the cell volume [1, 2]. In contrast, the servo-null technique allows a direct measurement by inserting a micropipette as a pressure probe [4], but in this process the cell membrane is mechanically damaged. Thus, the measurement of extracellular loads transmitted to the interior of the cell, and in particular to a subcellular component, has not been demonstrated directly. In fact, the cell is a highly complex and virtually unexplored mechanical system in which the membranes, cytoskeleton and extracellular matrix provide structural integrity.

In this chapter, a NanoOptoMechanical System that can be produced, collected and internalized inside living cells is reported. This system can detect intracellular pressure changes within living cells, enabling readouts through bright field and confocal laser scanning microscopies (CLSM) [20-22].

5.3 Concept

This design comprises a mechanical sensor defined by two membranes (separated by a vacuum gap), and an optical reference area (Figure 5.1a). The membranes act as parallel reflecting mirrors, constituting a Fabry-Pérot interferometer (see Appendix C), that is partially transparent for some wavelengths [23]. An external pressure (P) deflects the membranes and changes the gap distance (t_{gap}) (Figure 5.1b). Accordingly, the intensity of the reflected light at the centre of the membranes, (I_{r_Centre}), for a given wavelength (λ), is modulated by P. In addition, the reference area is used for focusing and normalization (I_{r_Ref}) purposes. Briefly, the sensing principle is based on the acquisition of images for a given a P versus λ and the quantification of I_{r_Centre}.
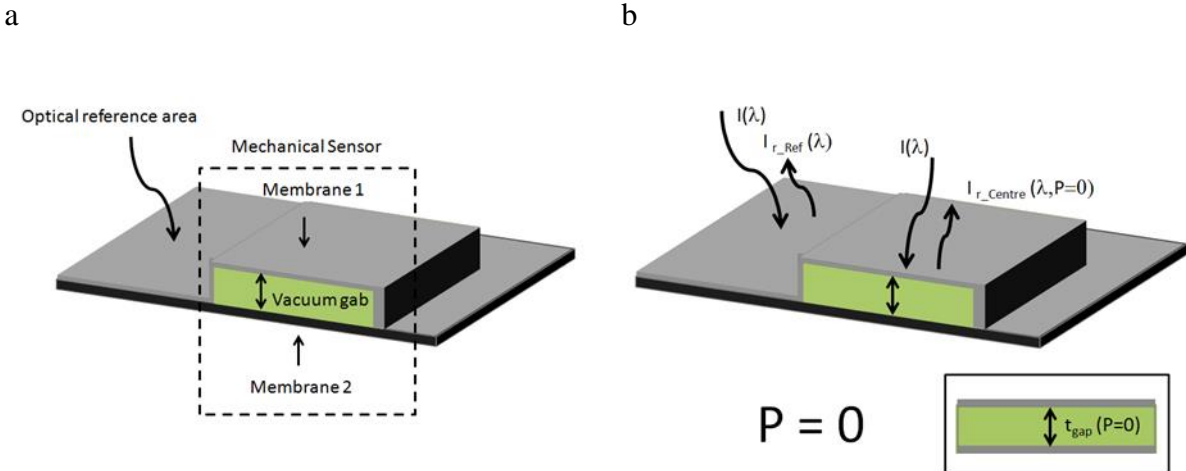
Figure 5.1: Design of the Intracellular Pressure Sensor. a) Schematic design of the mechanical sensor. b) Schematic draw of the working principle, illustrating the intensity of the incident light I (λ), and the intensities of the reflected light from the reference area I_{r_Ref} (λ) and from the centre of the membrane I_{r_Centre} (λ, P).

5.4 Preliminary theoretical analysis

The mechanical performance of the pressure sensor was simulated by the Finite Element Method (FEM) using ANSYS Multiphysics (Release 14.0, http://www.ansys.com). The device was modeled by using the 3D element SOLID95 and the layered 3D element SOLID186. First, the mechanical analysis was done, and then, optical simulations of the Fabry-Pérot (FP) structure were performed using the transfer matrix method. The numerical simulations could be subjected to inaccuracies in the mechanical-optical properties and dimensions of the simulated layers at the nanoscale.

5.4.1 Mechanical analysis

Based on polySilicon mechanical properties [24, 25], the analytical and simulated analysis show that the mechanical deformation of a polySilicon layer is highly dependent on the membrane thickness and show a linear response versus the applied pressure (P) (Figure 5.2). From these analysis, a value of 50 nm-thick membranes was selected (fixed 3 μm x 3 μm side), to achieve a theoretical mechanical sensitivity of 5.5 nm per bar. The dimensions of the polySilicon membrane, which strongly affect the sensitivity and the pressure response range, is also analyzed. The analytical formula, that describes the maximum displacement ($Displ_{memb}$) at the centre of a square plate of side a as a function of P, is given by the flexural rigidity of the plate (D). This value is defined by the thickness of the studied layer (t_{memb}) and the mechanical properties of the material by the Young's modulus (E), and the Poisson's ratio (ν) (the finite element analysis (FEA) is calculated for a deformation of 1 bar) [26]. The theoretical and simulated results of the $Displ_{memb}$ versus P are shown at Figure 5.2 and 5.3.
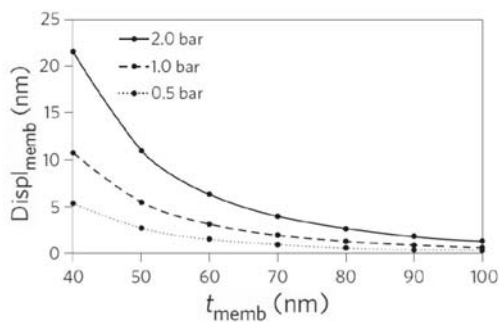
a   b
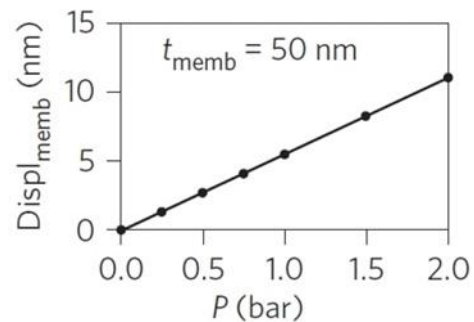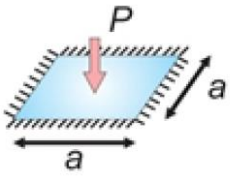
Figure 5.2: Mechanical analysis. Theoretical displacement of the membrane ($Displ_{memb}$), versus a) membrane thickness (t_{memb}) and b) versus applied pressure (P).

a   b

$$D = \frac{E}{(1-v^2)}\frac{t_{\mathrm{memb}}^3}{12}$$

$$Displ_{\mathrm{memb}} = 0.00126\frac{a^4}{D}$$
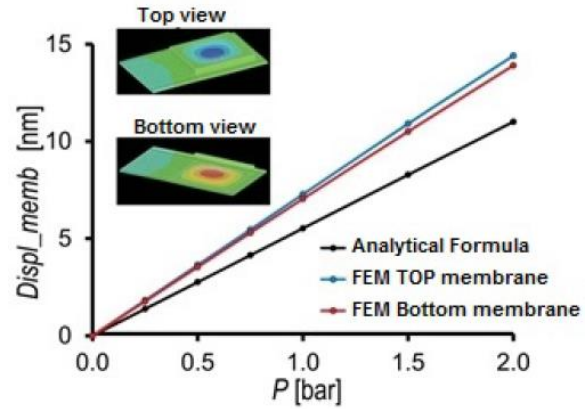
Figure 5.3: Applied load pressures: Theoretical analysis and FEM simulations. a) Maximum membrane displacement ($Displ_{\mathrm{memb}}$) as a function of flexural rigidity of the plate (D), side membrane dimension (a) and applied load pressure (P). D as function of Poisson's ratio (v) and the thickness of the studied layer (t_{memb}). b) Displacement ($Displ_{\mathrm{memb}}$) versus applied load pressure (P) for top and bottom membranes of the membrane calculated by the Finite element modeling and by the theoretical analysis.

Mechanical results, related to the potential cross-sensitivities for devices within cells due to unspecific adhesion of intracellular molecules to the mechanical membranes, was analyzed. The mechanical simulations about possible effects on surface stress cross-sensitivity due to non-specific biomolecular adsorption are shown in Figure 5.4.

a
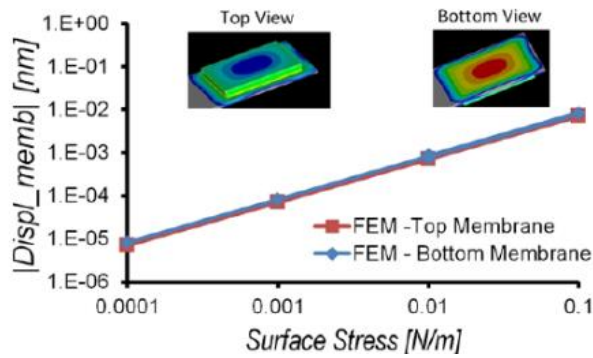
b
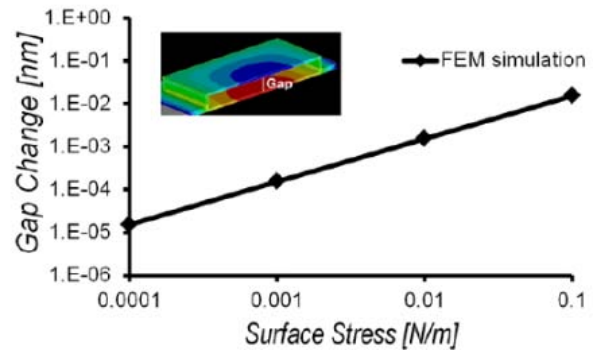
c
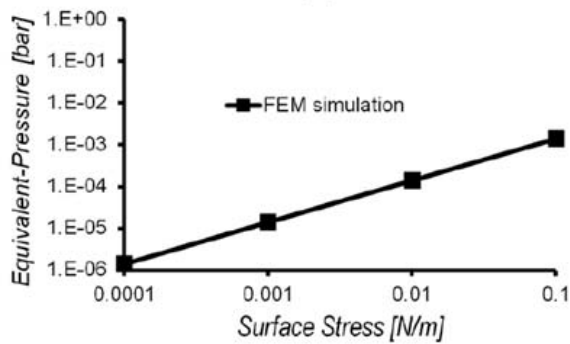
Equivalent pressure versus surface stress

1 mN/m ≡ 0.014 mbar

Figure 5.4: Mechanical effects due to unspecific biomolecular adsorption on polySilicon surfaces by FEM. a) Simulated absolute maximum displacement at the top and bottom membranes as a function of a surface stress load induce by unspecific biomolecular adsortion. b) Gap change as a function of the surface stress. c) An applied pressure (P) induces an equivalent displacement ($Displ_{memb}$) to the one which is induced by surface stress.

In addition, the result of an applied load pressure (P) versus a punctual force (F) was analyzed, for a lateral dimension of the mechanical membrane fixed in 3 µm. The analytical results explain an equivalent punctual force (F) at the centre of the membrane, which induces a $Displ_{memb}$ equal to the one induced by a pressure P (Equation 5.1). Its results show that for typical values of surface stress induced by unspecific biomolecular adsortion do not affect measurements of devices in range of a few bars.

Equation 5.1: Analytical formula. Applied load versus punctual force

$$\left.\begin{array}{l} Displ^{P}_{memb} = 0.00126\dfrac{a^4}{D}P \\[2em] Displ^{F}_{memb} = 0.0056\dfrac{a^2}{D}F \end{array}\right\} \quad \begin{array}{l} Displ^{P}_{memb} = Displ^{F}_{memb} \\[2em] Displ^{P}_{memb} = Displ^{F}_{memb}\big|_{a=3.10^{-6}m} \end{array} \quad \begin{array}{l} \Rightarrow P \equiv \frac{0.0056}{0.00126}\frac{1}{a^2}F \\[2em] \Rightarrow 200pN \equiv 1mbar \end{array}$$

5.4.2 Optical analysis

Without a doubt the most common material for the fabrication of MEMS devices is polycrystalline Silicon (PolySilicon) [24, 25]. In this way, polySilicon was selected as structural material because of its elastic behaviour and high reliability. In addition, polySilicon is also well known for its NOMS optical applications. The high refraction index of polySilicon gives a spectral selectivity to the structure and, subsequently, a high sensitivity to measure external applied pressures (P). Theoretically, the optical reflection of the structure (Figure 5.5) shows a resonance valley that is function of t_{gap} and (λ) (Figure 5.6). Thus, due to the applied pressure, that generates the gap change, the reflection curve shifted towards smaller values (~ 2 x Δt_{gap})

and, for a fixed λ, large variations in the reflection could be obtained. Where, $t_{gap} \sim 300$ nm was selected by considering the high optical sensitivity and cell internalization capabilities.
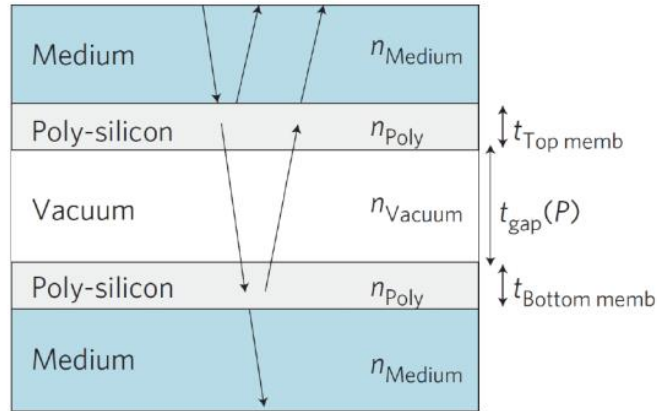
Figure 5.5: Sensing optical principle. Schematic of the optical multilayer structure defining the Fabry-Pérot resonator (n: refractive index; t: layer thickness).
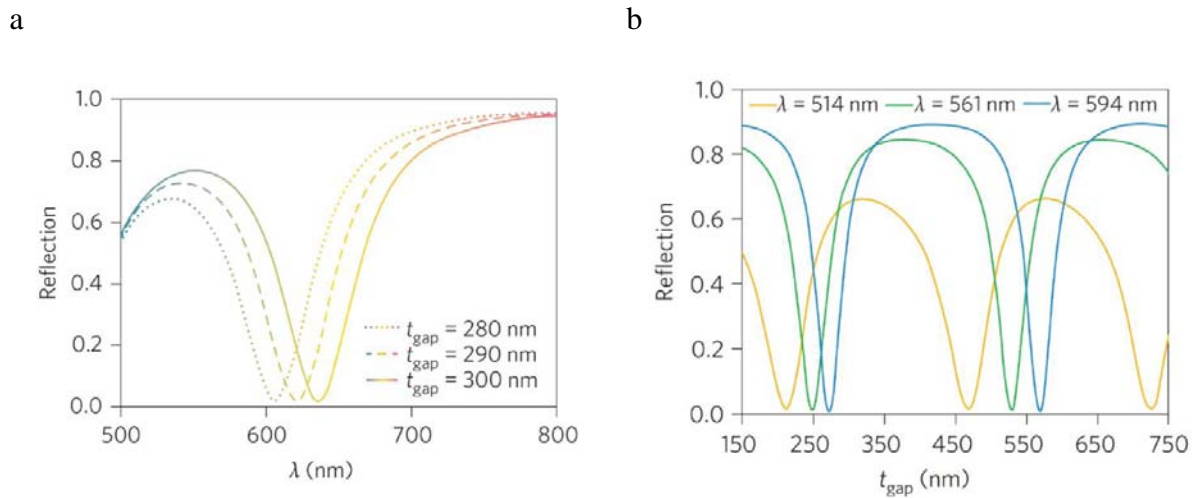
Figure 5.6: Reflection analysis of the Fabry-Pérot resonator. Simulated results of the reflection as function of wavelength (λ), a) and gap thickness (t_{gap}), b) for a multilayer structure comprising medium, 50 nm-thick polySilicon layer, vacuum gap, 50 nm-thick polySilicon layer and medium.

Respectively, the FP-resonator also depends of the incident light angle. Optical analysis shows the cross sensitivity due to the tilted of the device (Figure 5.7). First, the tilted device induced a uniform change all around the membrane on the reflected light of the FP. Meanwhile, the pressure induced a maximum change of the reflected light at the centre and zero change at its border (Figure 5.7a). Second, an optical simulation of the reflection versus the angle of the incidence of light (α), shows that the intensities of the reflected light at the reference area (Ir_Ref) are practically unaltered against the applied pressure (P) for a small tilt of the device. On the contrary, intensities of the reflected light at the centre area (Ir_Centre) shows pressure and tilt dependence (Figure 5.7b).

These results indicated that only devices with few degrees tilted should be processed and an algorithm to correct the results from tilted results must be developed. Simulations were performed in consideration of a plane wave on an infinitely long structure, mixed polarization with a ratio of 50/50, $\lambda = 594$ nm and an FP structure fitted to the experimental data.
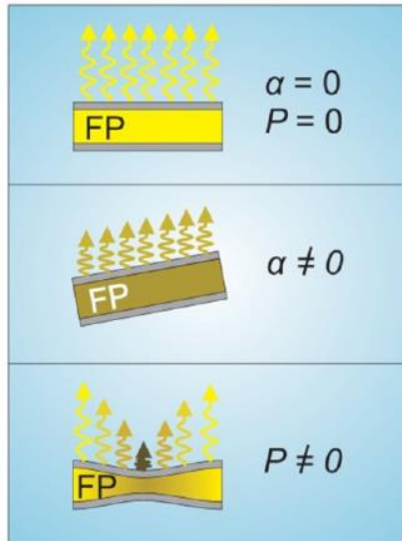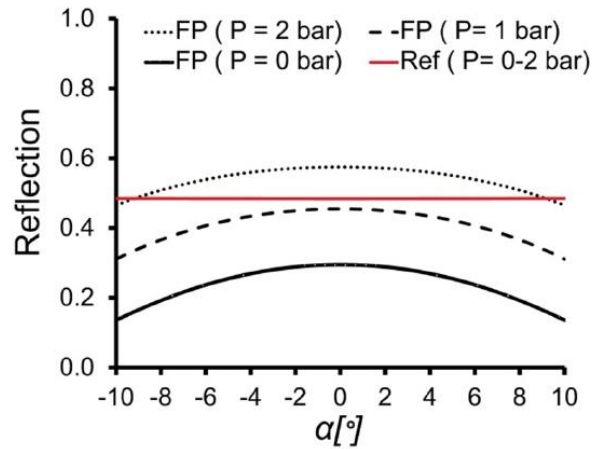
Figure 5.7: Optical analysis for the influence of the tilt of the devices in the Fabry-Pérot performance. Influence of applied pressure over the tilted device and over the reflected light. a) Reflected light readout due to tilt and the applied pressure (P). b) Simulated results of the reflection versus the angle of the light incidence (α).

5.5 Design of a NanoOptoMechanical System as an Intracellular Pressure Sensor

Based on the analytical and simulated analysis showed in the last sections, the lateral dimensions of the mechanical membranes (Fabry-Pérot resonator) were fixed to 3 μm x 3 μm side, and considering the lateral limitation of the reticle photolithographic technology that was used, the final dimensions of the NOMS were fixed to 6 μm x 4 μm, with an optical circular reference area fixed to 1 μm of diameter (Figure 5.8). The maximum height of the device was 400 nm.
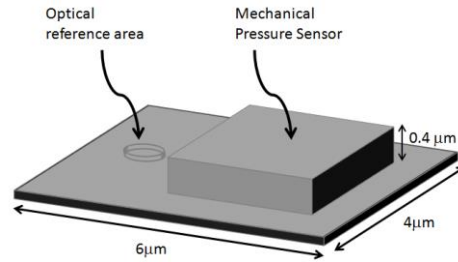
Figure 5.8: Design of the Intracellular Pressure Sensor. NOMS design includes an optical reference area and a mechanical pressure sensor. The final dimensions of the NOMS were fixed to 6 μm x 4 μm x 0.4 μm.

5.6 Technology development for the fabrication of the Pressure Sensor at wafer level

The technology of the NOMS combine three structural, and three sacrificial layers, made of polySilicon and Silicon oxide materials, respectively (Figure 5.9).

a   b
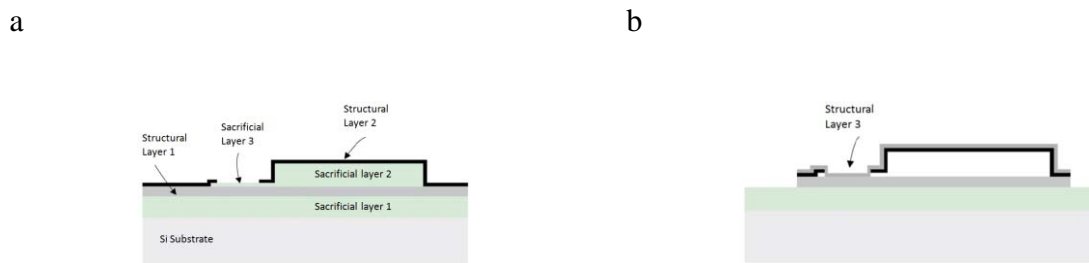
Figure 5.9: Schematic of the NOMS fabrication. a) The first sacrificial layer is used for the final release of the devices from the wafer. The first polySilicon layer (Structural layer 1) defines the bottom membrane; two layers of silicon dioxide, (sacrificial layer 2 and sacrificial layer 3), define the Fabry-Pérot cavity; another one layer of polySilicon (Structural layer 2), defines half of the top membrane, and b) the last polySilicon layer (Structural layer 3), defines the other half of the top membrane sealing the Fabry-Pérot cavity. Patterning the three structural layers the device was delimited.

5.6.1 Fabrication technology at wafer level

The silicon-based intracellular sensors were fabricated by combining photolithographic techniques with silicon microelectronic and micromachining technologies. The fabrication process includes the deposition of three structural polySilicon layers (Poly1, Poly2 and Poly3) and three sacrificial silicon dioxide layers (Ox1, Ox2 y Ox3) and four masks steps (Mask1, Mask2, Mask3 and Mask4) (Figure 5.10).

The initial substrates were 100 mm-diameter, 500 µm-thick, P-type, < 100 >, silicon wafers (Okmetic) (Figure 5.10a). A 100 nm-thick thermal silicon dioxide layer was grown by wet oxidation (950 $^{\circ}$C) -Ox1- (Figure 5.10b). A 50 nm-thick polySilicon layer was deposited by Chemical Vapour Deposition (570 ℃, 300 mTorr) -Poly1- (Figure 5.10c). A 300 nm-thick silicon dioxide TEOS (tetraethylorthosilicate, Si $(OC_2H_5)_4$) layer was deposited by Plasma-Enhanced Chemical Vapour Deposition -Ox2- (Figure 5.10d). The 1.2 µm-thick positive photoresist was spun onto the wafers (ma-P 6512 Micro Resist Technology). An exposure process to UV light (Stepper NSR1505-G7E; Nikon) was made through the first reticule. The resist was developed and baked (30 min, 200 $^{\circ}$C) (Figure 5.10e). The 300 nm-thick silicon dioxide layer was etched with C_2F_6 and CHF_3 (Drytek Quad 848). The photoresist was stripped (TEPLA 300-E, Techniques Plasma) (Figure 5.10f). A 30 nm-thick silicon dioxide TEOS layer was deposited -Ox3- (Figure 5.10g). The 1.2 µm-thick positive photoresist was spun onto the wafers. Exposure to UV light was performed through the second reticule. The resist was developed and baked (Figure 5.10h). The 30-nm silicon dioxide was wet etched by a buffered hydrofluoric acid (HF) solution (SiO-etch MT 06/01 VLSI Selectipur BASF) (Figure 5.10i), and the photoresist was stripped. A 25 nm-thick polySilicon layer was deposited -Poly2- (Figure 5.10j). A 1.2 µm-thick positive photoresist was spun onto the wafers. Exposure to UV light was

performed through the third reticule (Figure 5.10k). The resist was developed and baked. The 25 nm-thick polySilicon layer was etched using Cl_2 and HBr (AMI-Etch P-5000 MXP; Applied Materials Inc.) (Figure 5.10l) and the photoresist was stripped. A sacrificial layer of silicon oxide was wet etched using a HF-based solution (Figure 5.10m). Drying was performed with a critical point dryer of CO_2 (Automegasandri 915B, series C; Tousimis). A 25 nm-thick polySilicon layer was deposited -Poly3- (Figure 5.10n). The 1.2 µm-thick positive photoresist was spun onto the wafers (Figure 5.10o). Exposure to UV light was performed through the fourth reticule. The resist was developed and baked. The 100 nm-thick polysilicon layer was etched using Cl_2 and HBr (Figure 5.10p). The photoresist was stripped. Finally, the NOMS were released by hydrofluoric acid vapours (49% HF; Honeywell) (Figure 5.10q) and were collected in ethanol.

a. Si wafer
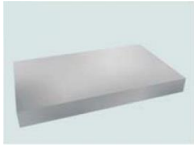
b. Ox1 layer
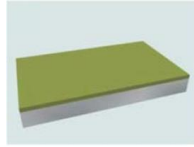
c. Poly1 layer
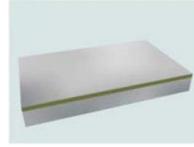
d. Ox2 layer
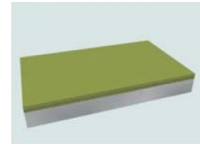
e. Mask 1
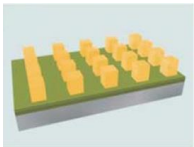
f. Etch Ox2
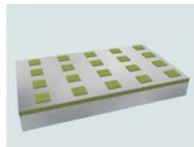
g. Ox3 layer
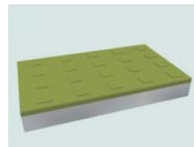
h. Mask 2
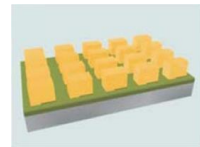
i. Etch Ox3
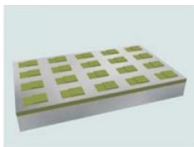
j. Poly2 layer
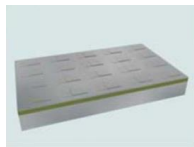
k. Mask 3

l. Etch Poly2
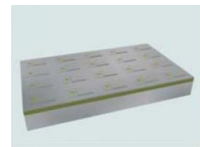
m. Etch Ox2
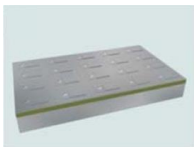
n. Poly3 layer
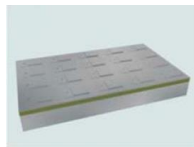
o. Mask 4
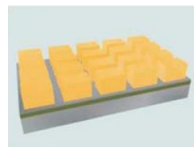
p. Etch Poly1,2 and 3

q. Etch Ox1

Silicon
Silicon Oxide
Photoresist
Polysilicon
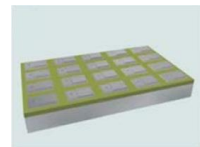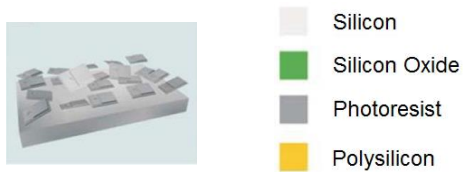
Figure 5.10: Detailed sequence of steps for the fabrication of the Intracellular Pressure Sensor. a) Silicon wafer as starting material, b) a silicon dioxide deposition (sacrificial layer, Ox1), c) 50 nm-thick polySilicon deposition (structural layer 1, Poly1). Next, d) silicon dioxide deposition (defining FP cavity, Ox2), e) the first photoresist spin and a photolithographic step (defining the lateral membrane dimensions, Mask 1), f) the etching away of the deposited silicon dioxide (RIE and photoresist stripping, Ox2), then g) 30 nm of silicon dioxide layer were deposited (Ox3 - layer). Next, h) a second photoresist step define the etching-port (Mask 2), i) an etching step of the deposited silicon dioxide layer (Etch Ox3). Then, j) 25 nm-thick polySilicon layer to define part of the top membrane was deposited (Poly2 - layer). Next, k) a third photoresist step defines the geometry of etching-port, l) the etching of exposed polySilicon layer (Poly2) of then, m) silicon dioxide through etching-port, was removed (Etch Ox2). Next, n) a 25 nm-thick polysilicon layer to hermetically seal the etching pore, and to define the device top of the mechanical membrane, was deposited (Poly3-layer). Then, o) a fourth and last photoresist step defines the final dimensions of the devices. The last two steps, include p) etch away the exposed polysilicon, which defines the devices (Etch - Poly3) and q) HF vapors to etch step of the sacrificial silicon dioxide (Etch - Ox1), to release the chips from the wafer.

5.6.2 Device release and collection

As it was described in section 2.6, once the intracellular pressure sensor manufacturing process has finished (Figure 5.10q, sacrificial etching step), the wafer was divided into small pieces (1 cm x 1 cm) by a diamond tip, for a better handling. Then, each piece was placed in to a Teflon holder, where it was subjected to 49% HF vapours for 40 minutes (Figure 2.7). These HF vapours released the devices from the wafer substrate by a silicon dioxide wet etching. The collection process started with the immersion of a piece of wafer into a glass beaker, containing 96 % ethanol, after the sonicated step, which allows the final released of the devices into the ethanol beaker. Once the devices were suspended in ethanol, they were collected in different eppendorfs and the devices were concentrated by centrifugation and kept then for subsequent studies. After that, before handling these devices, the eppendorfs were again centrifuged and the supernatant extracted. This process allows the manipulation of the devices in microliter quantities by using micropipettes.

5.7 Specific considerations of the polySilicon nanolayer

Different preliminary tests were performed to analyze the polysilicon structural material, and its stability within the cell.

5.7.1 Surface quality of the deposited polySilicon layer.

Different conditions for the polySilicon deposition were analyzed to evaluate the physical characteristics of this material, such as roughness (Table 5.1) and optical appearance (Figure 5.11). Roughens (spots) or flat (not spot) surface results determine mechanical and optical

148

performance of the device. Flat surface deposition results enable an optimal functioning of the devices.These results allowed us to select the best deposition condictions.

Table 5.1: Polysilicon deposition conditions

Wafer	T ^{O}C	Pressure [mTorr]	Flow [sccm]	Chemical environment	Thickness [nm]	Roughness [Å] (P1, P2 = points of test)
W1	570	350	45	SiH$_4$	78	P1 = 14,2 - P2 = 22,5
W2	580	350	45	SiH$_4$	67	P1 = 17,6 - P2 = 26,3
W3	630	90	25	SiH$_4$	64	P1 = 19,9 - P2 = 25,0
W4	620	90	25	SiH$_4$	57	P1 = 19,1 - P2 = 27,9
W5	630	120	25	SiH$_4$	67	P1 = 18,6 - P2 = 26,9
W6	620	120	25	SiH$_4$	310	P1 = 33,7 - P2 = 27,1
W7	620	120	25	SiH$_4$	62	P1 = 34, - P2 = 32,0

5.7.2 Fabrication and hermeticity analysis of polySilicon layer

Once the limits of the technology were assessed, the next step was to evaluate the hermeticity of the polysilicon layers. The hermeticity is one of the most important properties for the manufacture of the pressure sensor, due to any kind of porosity present in the polySilicon layers can negatively affect the pressure determination (Figure 5.12).

To test the hermeticity of the polySilicon layers, a new technological fabrication sequence was carried out to produce dummy test wafer. Initial substrates 100 mm-thick, 500-µm-thick, P-type, < 100 >, silicon wafers (Okmetic) as shown on Figure 5.10a were used. Then, a silicon oxide layer was deposited as the sacrificial layer as shown on Etch Ox1, Figure 5.10b. Then, the

dummy layers of polysilicon were deposited under different process conditions. Next, the wafer was diced in 1 cm x 1 cm samples. To test the best results in terms of hermeticity the samples were immersed on HF. The samples with porosity showed the etching of the sacrificial silicon oxide underneath each porous in the polysilicon layer.

5.7.3 PolySilicon degradation test

Some polySilicon degradation layer tests at pH = 4, pH = 7 and pH = 9 were performed. These results will help us to evaluate the potential degradation of the devices inside the cell environment. A fast material degradation inside the cell will ruin the device performance.

Dummy wafers with a sacrificial silicon oxide layer and the 50 nm-thick polysilicon (Poly1) (Figure 5.10c) were used for the degradation test. Next, the wafer was diced in 1 cm x 1 cm samples. Then, the samples were immersed from 1 to 7 days in three different buffered solutions of pH = 4, 7 and 9 (Crison)

After etching, the polysilicon thickness was measured in a spectroscopic reflectometer (Nanospec 3000). The results did not show any detectable degradation (Figure 5.13), which allowed us to do not consider a relevant degradation of the chips inside the cells.

a

b

c

d

e

f

g
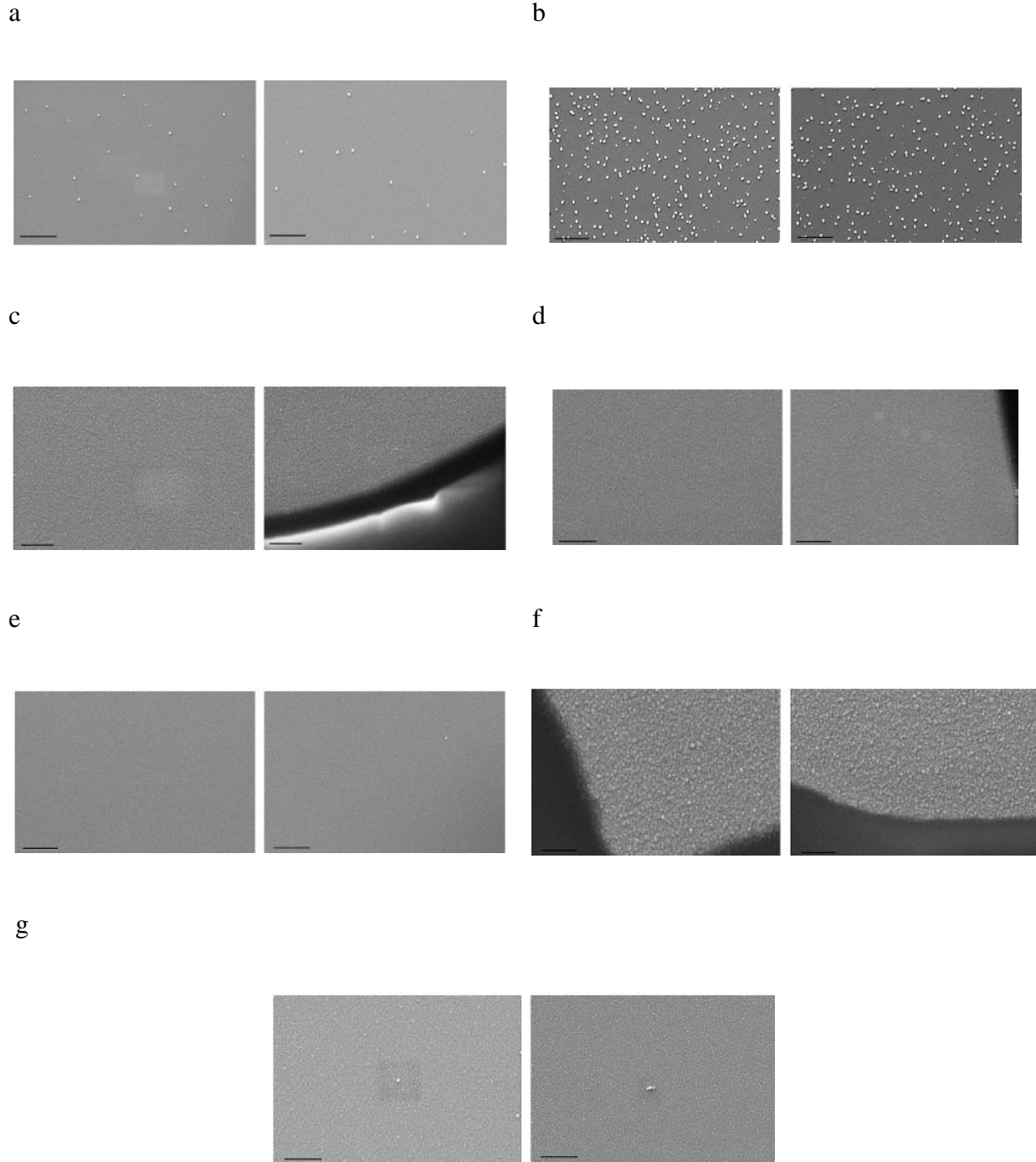
Figure 5.11: SEM images of the deposited polySilicon layers. Scanning electron microscopy images of the different thicknesses of polySilicon depositions. a) Wafer 1, b) wafer 2, c) wafer 3, d) wafer 4, e) wafer 5, f) wafer 6 and g) wafer 7. Scale bar = 300 nm.
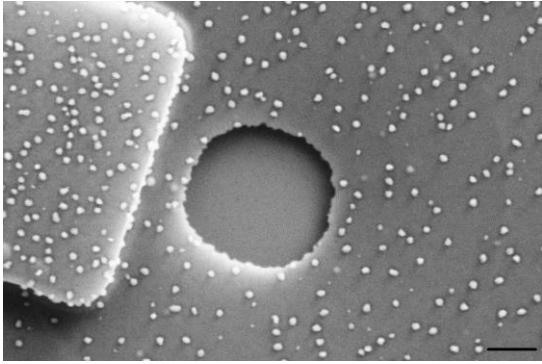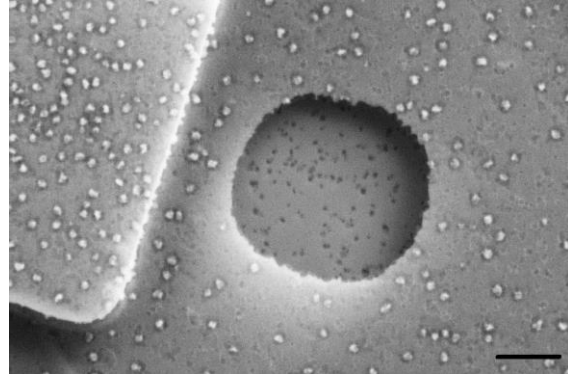
Figure 5.12: Porosity test of the polySilicon layer. HF etching test allowed the identification of the tightness of the deposited polySilicon layer (Poly1, 50 nm-thick layer, figure 5.11c). Porous silicon layers involve a loss of sealing devices. SEM images of a) the non-porous polySilicon layer at the bottom of the hole, and b) of the porous polySilicon layer at the bottom of the hole. Scale bar = 300 nm.
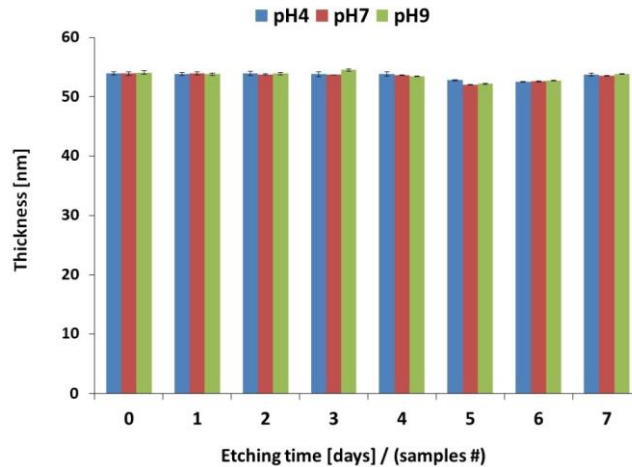
Figure 5.13: Degradation polySilicon layer tests. PolySilicon thickness versus etching time in buffer solutions under pH = 4, pH = 7 and pH = 9 conditions.

5.8 Microscopy characterization of the Intracellular Pressure Sensor

Due to the small dimensions of the devices, four high-resolution inspection techniques, (SEM, Confocal Microscopy, Confocal Laser Scanning Microscopy (CLSM) and Atomic Force Microscopy (AFM)), were used to characterize the fabricated chips.

5.8.1 Scanning electron microscopy inspection

Scanning electron microscopy was used to characterize the fabricated devices. Images of the NanoOptoMechanical Systems still on the wafer can be seen in figure 5.14a, b and c. In addition, several released chips after 49% HF wet etching can be observed in figure 5.14d and e. As it can be observed the fabricated chips maintain their well defined shape, dimensions and robust design even after their wafer release.
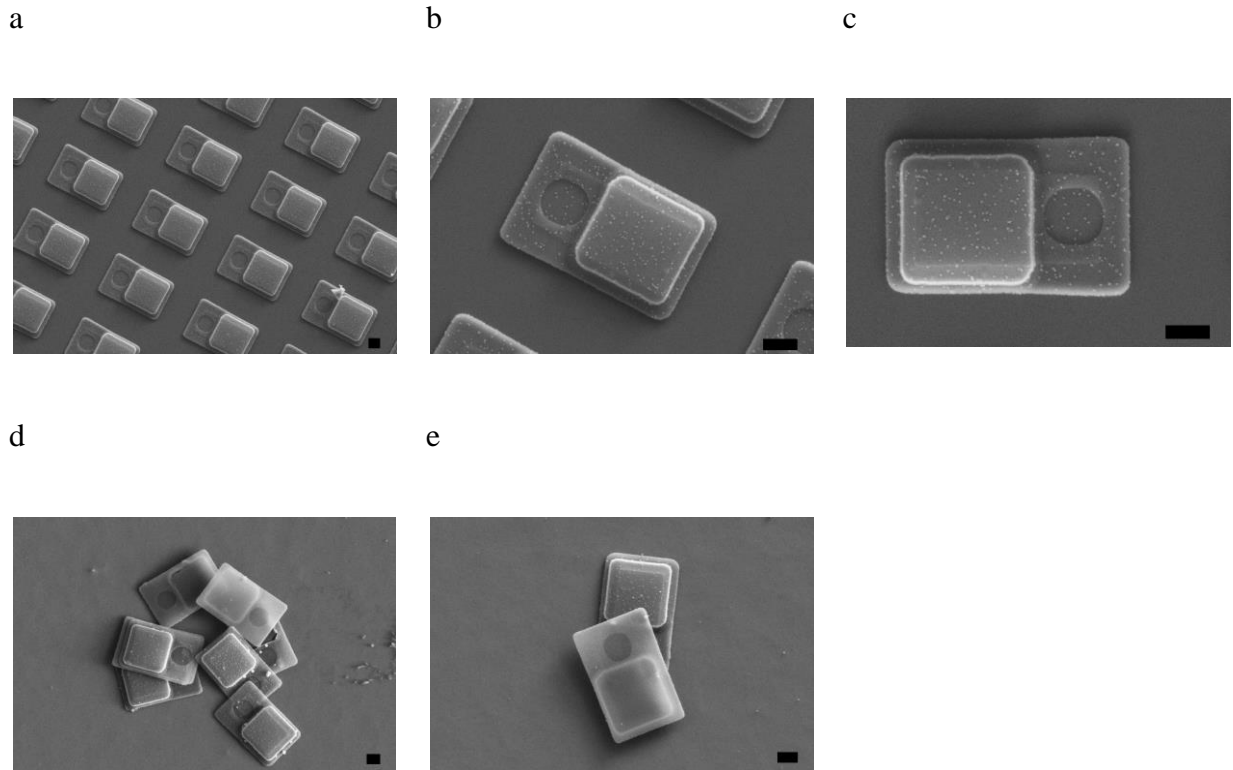
Figure 5.14: SEM images of the fabrication results of the Intracellular Pressure Sensors.
Scanning electron microscope images of the fabricated chips. a-c) On the wafer, and d-e) after their release. Scale bar = 1 μm.

5.8.2 Confocal microscopy inspection

The devices were measured for a topography characterization by confocal microscopy (3D optical profiler Microscopy, Pl-µSensofar) (Figure 5.15). These techniques allow to determine the dimensions and final shape of the fabricated chips. Figure 5.15 show a total high of 400 nm. The resolution of the in-house equipment does not allow a precise characterization of the dimension of the devices.
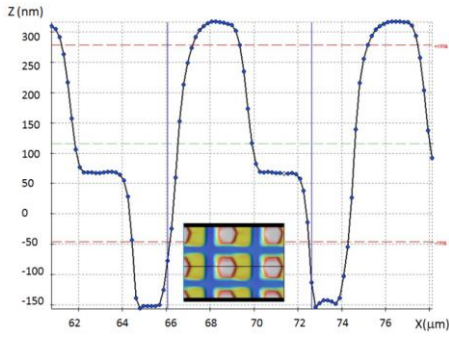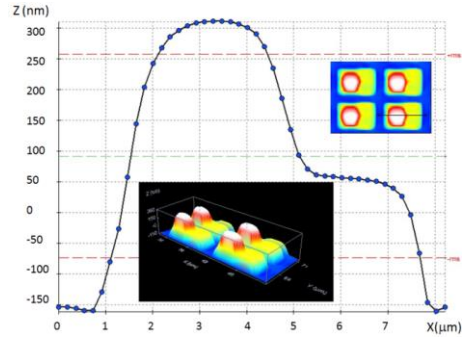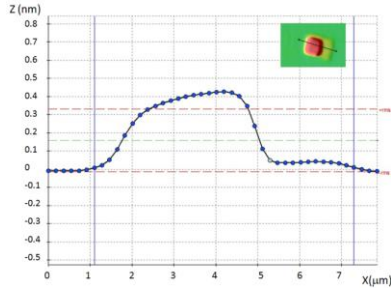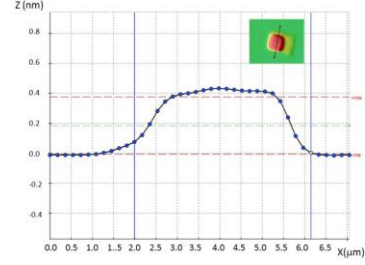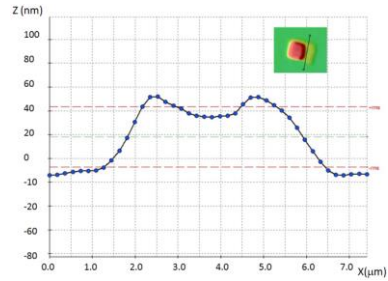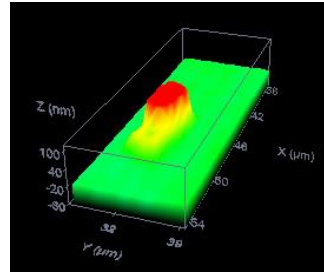
Figure 5.15: Confocal characterization of the Intracellular Pressure Sensors. a) 2D profile image and its corresponding 3D confocal image (inset) and b) 2D profile image and 3D confocal images (insets) of a small wafer area. c-e) 2D profiles images and 3D confocal (inset) of different chip areas and f) a 3D confocal image for the same release device.

5.8.3 Atomic force microscopy inspection

The fabricated Intracellular Pressure Sensors (IPS) were measured for a dimension characterization by atomic force microscopy (AFM) (Cypher Atomic Force Microscope (Asylum Research)) (Figure 5.16). This technique allows the collection of accuracy values of the final dimensions of the fabricated chips. In figure 5.16a a 2D AFM image of a fabricated chip can be observed. In figure 5.16b a profile with two steps at 100 nm and 400 nm and a 3D AFM image of figure 5.16a (inset) are shown.
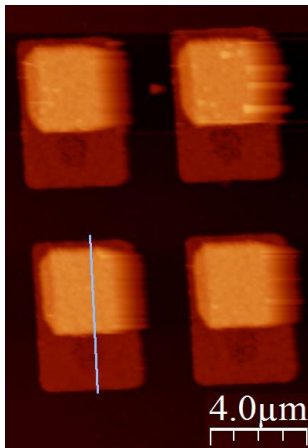
a   b
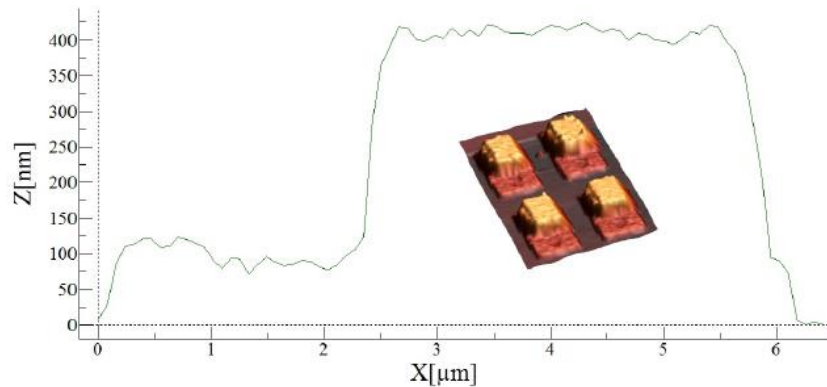
Figure 5.16: Atomic force microscopy images of the fabricated IPS. a) 2D AFM image and b) its corresponding profile (Inset: 3D image of a small wafer area).

5.9 Validation of the sensing principle for pressure detection

5.9.1 Bright-field optical microscopy

The fabricated devices were validated using a bright-field optical microscope (BFOM). The pressure setup consisted of a portable pressure calibration kit (LPP-KIT-PD-05-9005, Druck & Temperature Leitenberger GmbH) and PolyTetraFluoroEthylene (PTFE) tubing. The LPP-KIT includes a LPP 30 hand pump that was used to generate pressures up to +35 bar and the electronic pressure calibrator LR-Cal TLDMM with a range of -1 to +5 bar with an accuracy of 0.05% FS.

The preliminary pressure experiments were conducted inside a hermetic handmade pressure chamber (Figure 5.17) for the microscope (Nikon Eclipse ME600L). The methacrylate robust parts were joined to a metallic body with an inspection hole to fix the cover slip (12 mm-diameter) which provided a high stiffness for the pressure experiments (Figure 5.17).
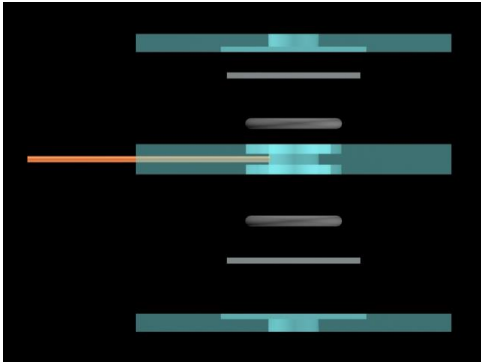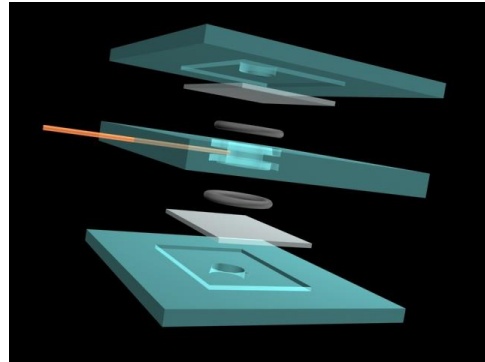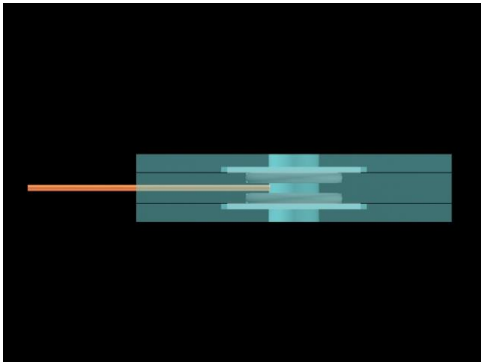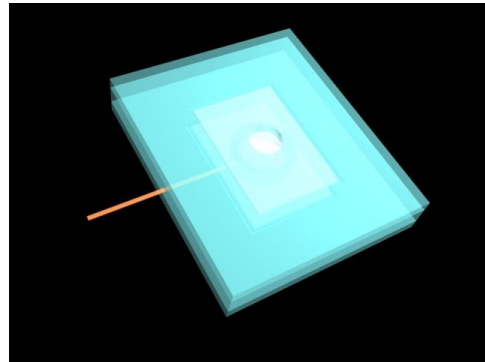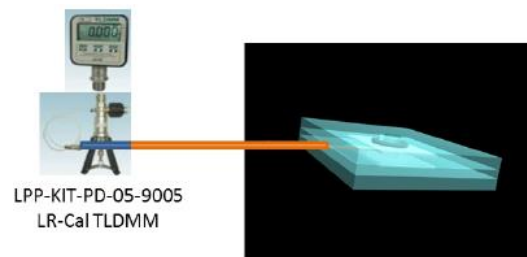
Figure 5.17: Handmade pressure chamber built for the validations of the sensing principle. a-d) Different views of the design of a hand-made pressure chamber. e) Pressure setup consisted of a portable pressure calibration kit with a hermetic pressure chamber.

The fabricated devices were validated using a bright-field optical microscope. Experimental true-color images wavelength (λ) versus pressure (P) in air medium were performed. An Eclipse ME600 upright optical microscope (Nikon), with a 100x magnification by a 0.8 NA long-distance objective LU Plan ELWD 3.5 (Nikon) was used. Images via an 8-bit color CCD camera (DXM1200F; Nikon) using the advanced control software Nikon ACT-1 (Automatic Camera Tamer) were recorded. And band-pass filters from 500 nm to 650 nm (THORLABS, Ltd) coupled with an YM-NCB11 filter slider (Nikon) to select the wavelength (λ) of the incident light were used.
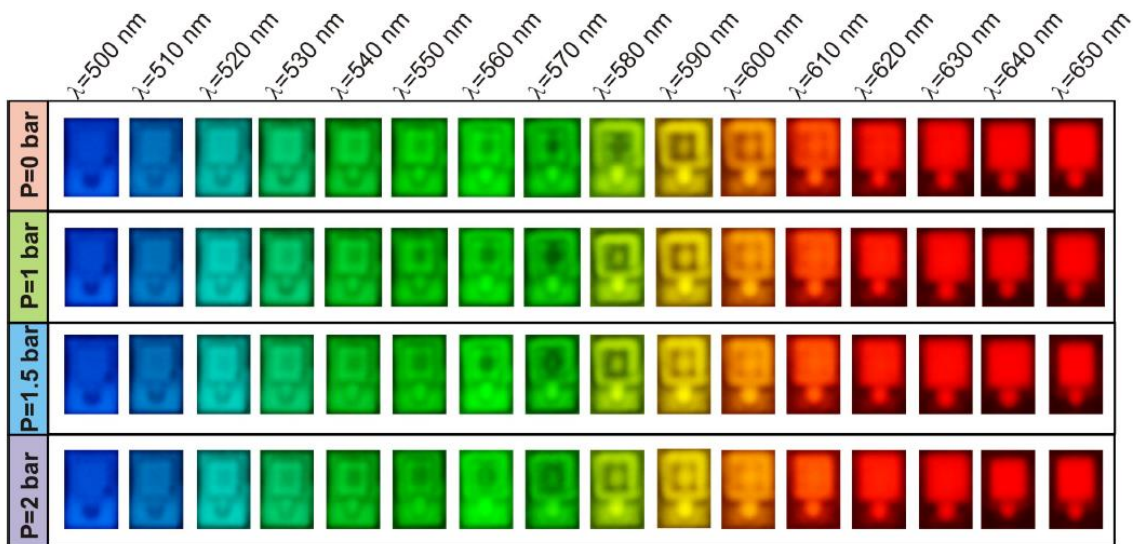
Figure 5.18: Validation of the sensing principle. Experimental true-color images taken on a bright-field optical microscope with an 8-bit colour CCD camera wavelength (λ) versus pressure (P). Band-pass filters from 500 nm to 600 nm were used to select the working wavelength (λ) for P = 0 to 2 bar.

After observing the optical changes in the reflection versus the applied pressure (P) for a fixed working wavelength (λ) (Figure 5.18) several analytical analyses, to obtain values to these optical changes, were performed. IMAGEJ software (Rasband, W.S., IMAGEJ U. S. NIH, http://rsb.info.nih.gov/ij/) was use for this task. First, two regions of interest (ROI), (I_{r_Centre} and I_{r_Ref}) to each experimental true color images, were assigned (Figure 5.19).
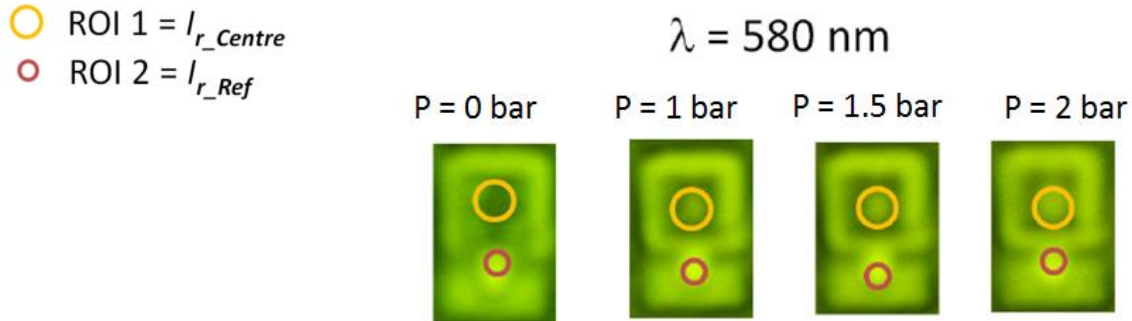
Figure 5.19: Regions of interest (ROI) of the experimental true-color images. Examples of assigned ROIs to experimental true color images taken by bright-field optical microscope with an 8-bit colour CCD camera versus wavelength (λ) and applied pressure (P) (i.e $\lambda = 580$ nm).

Secondly, the arbitrary values measured by ROI1 were analyzed by the following equation $(I_{r\_Centre}(Px) - I_{r\_Centre}(Po))/ (Px - P0)$ for x =0, 1, 1.5 , 2 by each λ. The results showed a high sensitivity for $\lambda = 580$ nm (P = 1 bar) (Figure 5.20).

To avoid errors between the different images, due to any change through the optical path, the measurements were normalized (I_{r_Centre}/I_{r_Ref}) at 255 a.u. for $\lambda = 500$ nm, for measured ROIs (Figure 5.19). External pressure was applied from 0 to 1 bar and from 1 to 0 bars. The result showed how the applied pressure (P) can induce a shift of the curve towards smaller wavelengths (λ). Additionally, for a fixed λ positive or negative sensitivities were also observed (black

arrows) (Figure 5.21). This experiment showed a minimum reflection for $\lambda = 570$ nm. For a fixed λ, I_{r_Centre} increased depending of the applied pressure (P) for $\lambda > 580$ nm and decreased for $\lambda < 560$ nm. I_{r_Sensor} decreased with a laser wavelength of $\lambda = 514$ nm and increased for values of $\lambda = 594$ nm (Figure 5.21b).
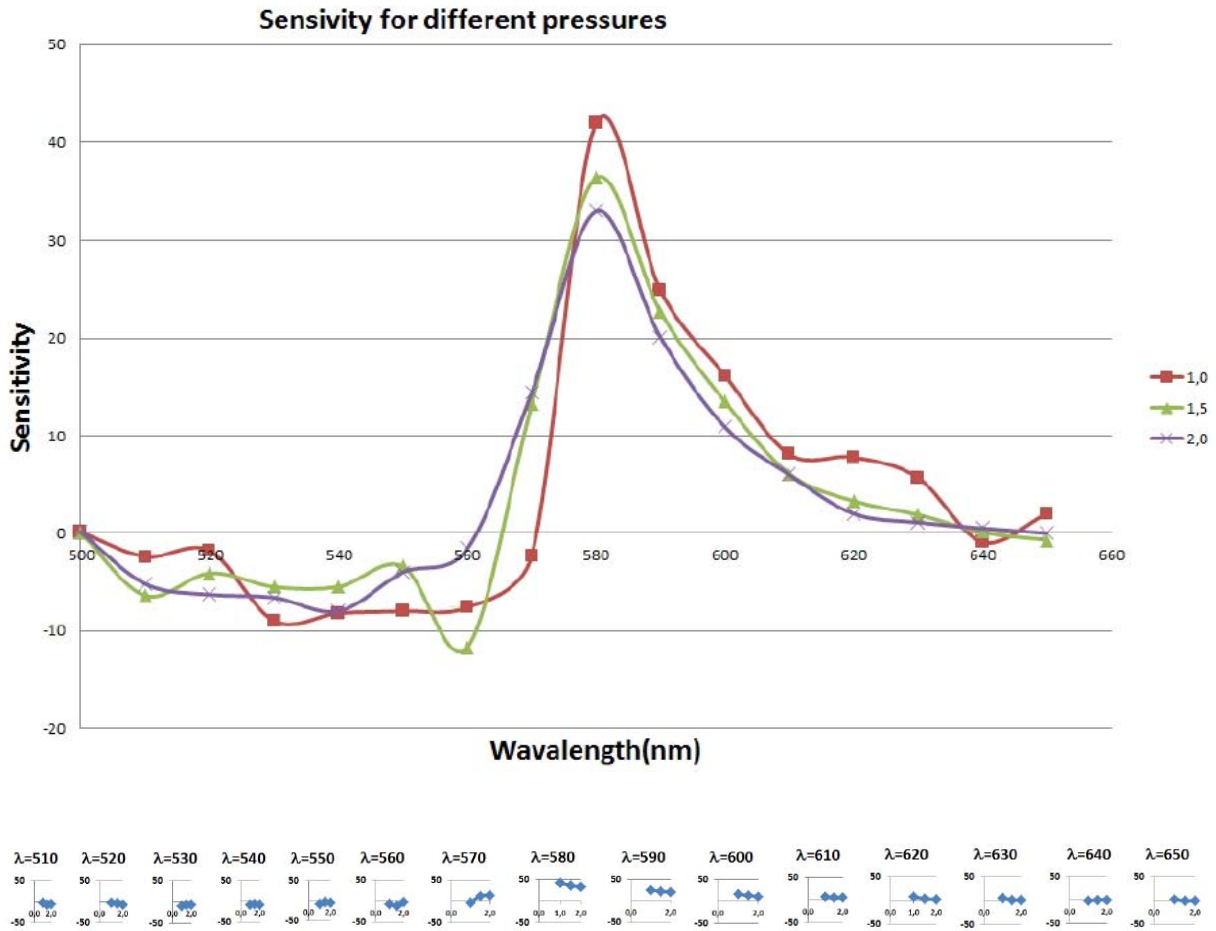
Figure 5.20 Experimental spectrum taken from the true-color images. Normalized values $(I_{r\_Centre}(Px) - I_{r\_Centre}(Po))/(Px - P0)$ for x = 0, 1, 1.5, 2 showed a high sensitivity for $\lambda = 580$ nm.

a
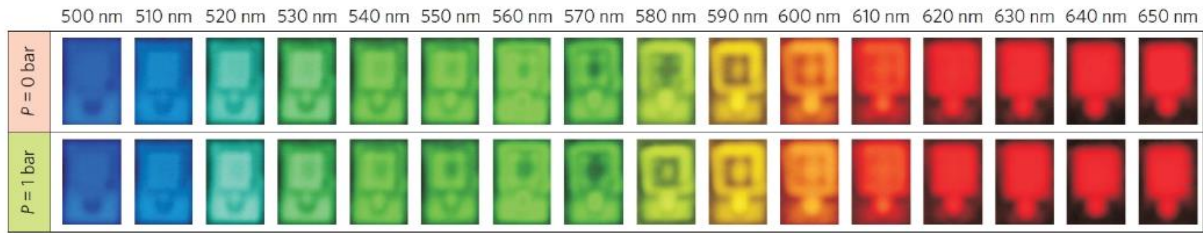
b
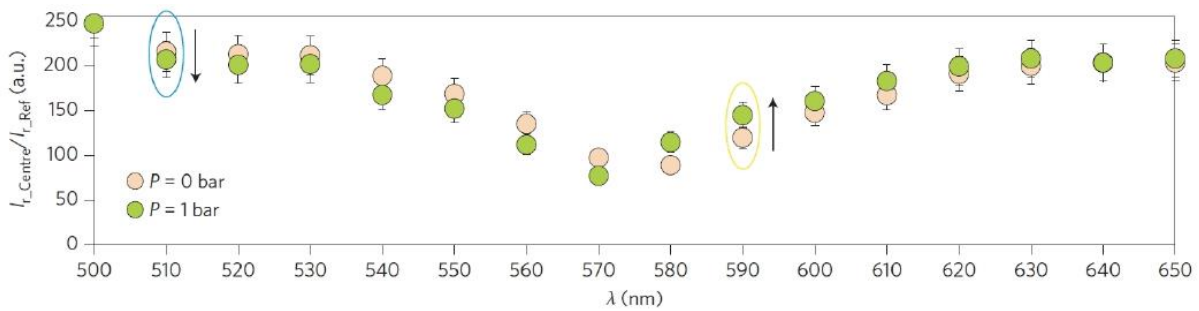
Figure 5.21: Validation of the sensing principle. Bright field optical microscope (BFOM) experiment in air medium. a) Experimental true-color images taken by an eight-bit color CCD camera λ versus P. Band-pass filters from 500 nm to 650 nm were used to select the working λ. b) Normalized I_{r_Centre}/I_{r_Ref} (255 a.u. for $\lambda = 500$ nm). Applied pressure (P) induces a lateral displacement of the curve towards smaller wavelengths (λ). For a fixed λ positive or negative sensitivities were observed (black arrows). Ovals indicate light color ($\lambda = 510$ nm, blue; $\lambda = 590$ nm, yellow). Error bars $= \pm 10$ % (values on uncertainly measurements from the studies images).

5.9.2 Confocal scanning laser microscopy

The fabricated devices were validated using Confocal Scanning laser Microscopy (CLSM). Experimental images versus wavelength (λ) and applied pressure (P), in air medium, were performed. Confocal images were acquired by a confocal Leica TCS-SP5 microscope (Leica Microsystems GMbH) using 514 nm, 561 nm and 594 nm excitation laser wavelengths (AOTF = 1%) for the fabricated batch of chips. The confocal analyses were conducted in the AOBS reflection mode, with 16 bit-depth resolution and in the X-Y-Z scan mode. A 63x/0.9 HCX APO water objective (Leica Microsystems GMbH), with an acquisition time of ~ 25 s was used. Finally, the images were pre-analyzed by LAS AF (Leica Microsystems GMbH).

The pressure setup consisted of a portable pressure calibration kit LPP-KIT-PD-05-9005 (Druck & Temperature Leitenberger GmbH) and PTFE tubing. The LPP-KIT included a LPP 30 hand pump that was used to generate pressures up to +35 bar and the electronic pressure calibrator LR-Cal TLDMM with a range of -1 bar to +5 bar and an accuracy of 0.05% FS. The pressure experiments were conducted inside a hermetic live-imaging chamber (for the microscope) (Ludin Chamber Type 3; Life Imaging Services GmbH). The steel body and the cover slip (12 mm-diameter) provided a high stiffness for the pressure experiments. The CLSM-pressure set-up is shown in Figure 5.2
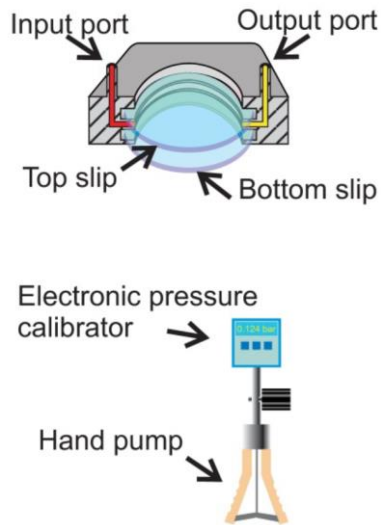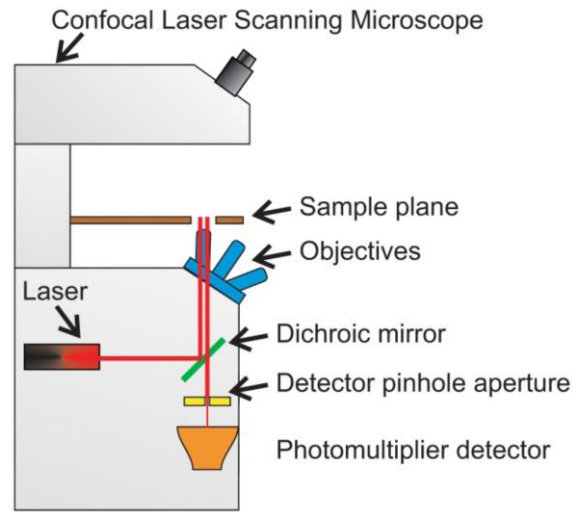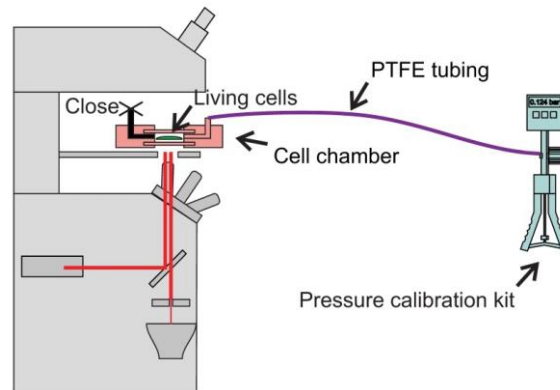
Figure 5.22: Confocal laser scanning microscope and pressure setup. a) A schematic cross-section of the cell chamber showing the top and the bottom cover-slip and a schematic view of the pressure calibrator kit. Cells were cultivated on coverslips, which are placed inside the cell chamber. b) A schematic view of the CLSM showing the main parts. c) A schematic view of the set-up. The cell chamber was hermetically sealed using a top slip and closing one of the ports for pressure experiments.

External pressure was applied from 0 bar to 1 bar and from 1 bar to 0 bar. Intensity of the reflected light at sensor (I_{r_Sensor}) decreased with a laser wavelength of $\lambda = 514$ nm and increased with values of wavelength $\lambda = 594$ nm (Figure 5.23). CLSM high resolution images allowed an accurate image processing algorithm developed to detect the pressure loads applied over the IPS, based on a quantification of the mean intensities of three regions of interest (Figure 5.24a).
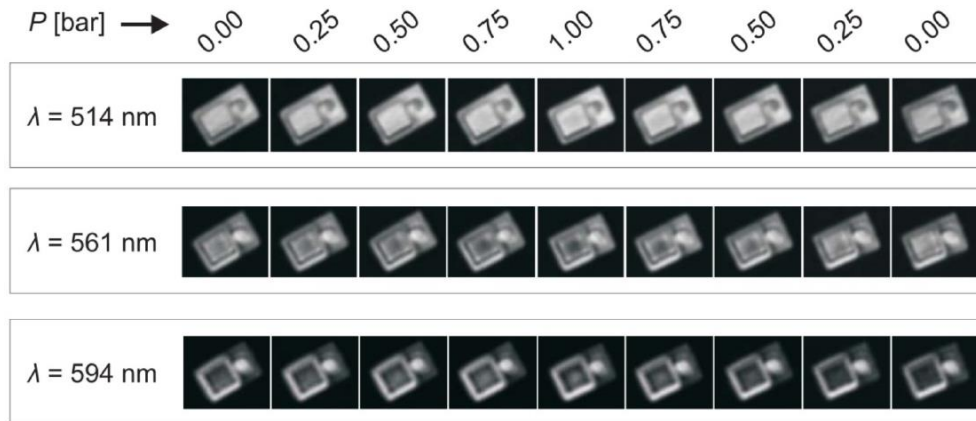
Figure 5.23: Confocal laser scanning microscope results of the experimental reflective images. Experimental reflective images taken with a confocal laser scanning microscope using $\lambda = 514$ nm, 561 nm and 594 nm excitation laser wavelengths versus a specific applied pressure (P) (for P = 0 to 1 bars, and 1 to 0 bars, steps = 0.250 bars).

Following the same method used in bright field optical microscope tests, analytical analysis provides values through CLSM reflective images. The CLSM images were processed using the IMAGEJ software (Rasband, W.S., IMAGEJ U. S. NIH). .Lif files from the CLSM Leica AS contained separated images of transmitted visible light and reflected light from lasers. The transmission channel was not required for processing. The following processes were conducted for every laser channel and every applied pressure. Three different circular Regions of Interest

(ROI) were selected and their mean intensities were obtained (Figure 5.24a). First, the ROI (Ref) was used to select the on-focus slide, the maximum mean intensity on ROI (Ref), from the z-stack images obtained by the CLSM (Figure 5.24b). Second, after the intensity (I) was calculated for each ROI (Figure 5.25), the ROI (Ref) was used for the normalization of the intensities because I_{r_Ref} do not depend on applied pressure (P). Data were normalized by a β-mean intensity factor at the initial pressure (P = 0) (Figure 5.26). Third, the normalized mean intensities at ROI (Centre) and ROI (Border) were subtracted to compensate the device-tilt cross-sensitivities (Figure 5.27).

a   b
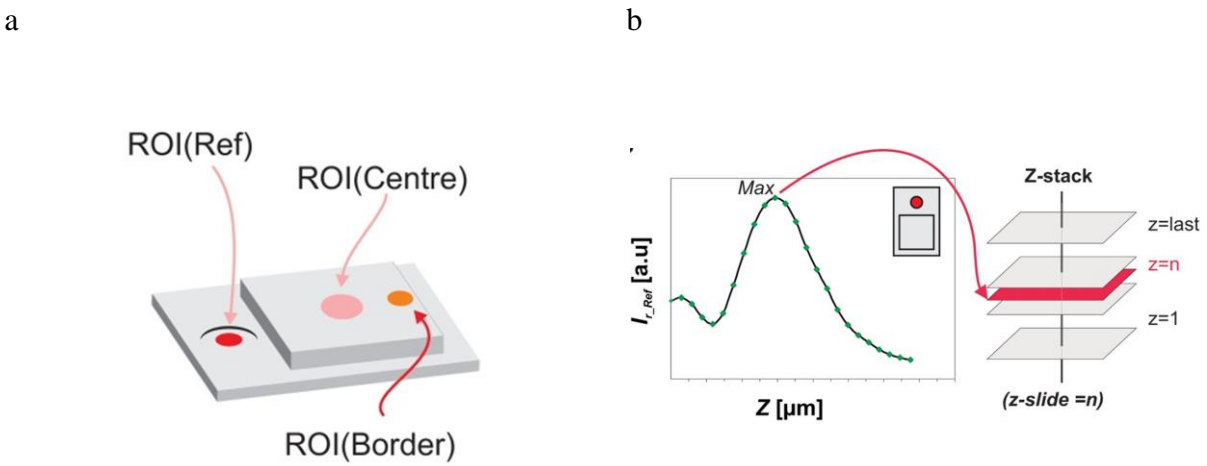
Figure 5.24: Localization of the ROIs for the confocal laser scanning microscope image processing (I). a) Schematic view of the regions of interest (ROIs). b) The selection of the well-focused images (images with the highest I_{r_Ref}) from the z-stack obtained by the CLSM.
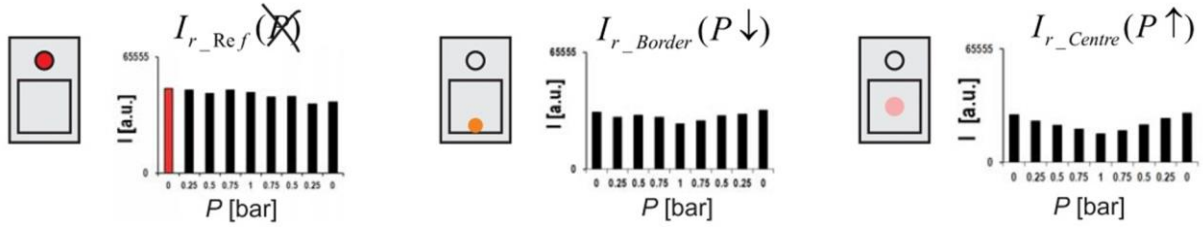
Figure 5.25: Confocal laser scanning microscope image processing (II). Experimental measurements of the intensity reflected image at each regions of interest (ROI) (I_{r_Ref}, I_{r_Border} and I_{r_Centre}), for applied pressure (P) and wavelength (λ).

Equation β-mean normalization factor:

$$\beta = \frac{I_{r\_Ref}\,(P=0)}{I_{r\_Ref}\,(P)}$$
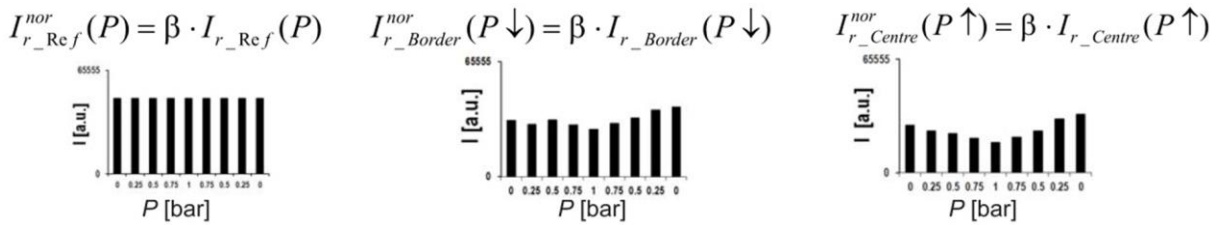
Figure 5.26: Confocal laser scanning microscope image processing (III). Processing of the intensity reflected image at different regions of interest (ROI) (I_{r_Ref}, I_{r_Border} and I_{r_Centre}), after the normalization by factor β, for each applied pressure (P) and each wavelength (λ).

$$I_{r\_Sensor}(P) = I^{nor}_{r\_Centre}(P) - I^{nor}_{r\_Border}(P) + I^{nor}_{r\_Border}(P = 0)$$
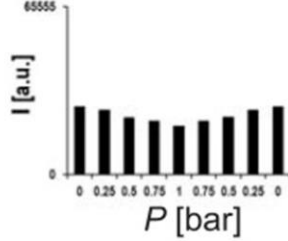
Figure 5.27: Confocal laser scanning microscope images processing (IV). Final analytical processing of the intensity reflected image to obtain the sensor intensity (I_{r_Sensor}), for an applied pressure (P) and wavelength (λ). At ROI normalized I_{r_Centre} was subtracted at ROI normalized I_{r_Border}.

5.9.3 Analytical experimental results

CLSM experiments in air medium show the relation between $I_{r\ Sensor}$ versus P from 16-bit deep images. Lasers with λ = 514 nm, 561 nm and 594 nm were used to select the working λ. External pressure was applied from 0 to 1 bar and from 1 bar to 0 bar.

The analytical results, after the image processing, show that $I_{r\ Sensor}$ decreased with the laser wavelength of λ = 514 nm and increased with a wavelength value of λ = 594 nm. When P increase positive and negative sensitivities were also observed at λ = 594 nm and λ = 514 nm, respectively. $I_{r\ Sensor}$ decreased for $0 \leq P \leq 0.75$ bar values and increased for P = 1 bar, λ = 561 nm, because this λ is close to the resonance valley of the Fabry-Pérot spectrum (Figure 5.28).
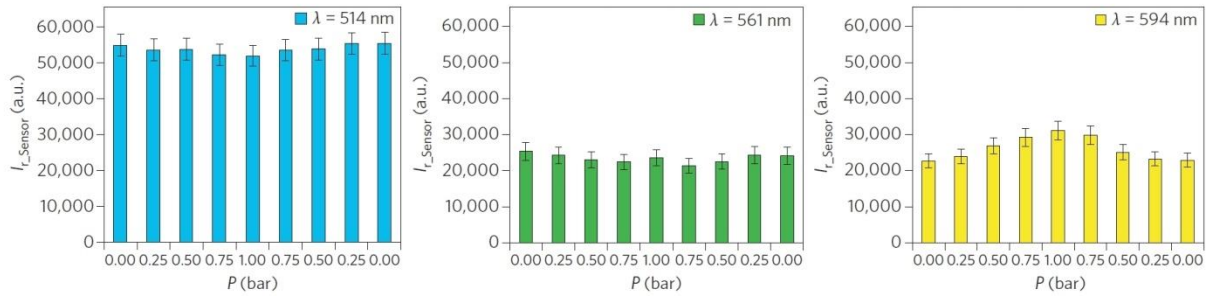
Figure 5.28: Confocal experimental results for I$_{r\ Sensor}$ versus P. The reflected intensity on the FP resonator. Lasers with $\lambda = 514$ nm and 594 nm show positive and negative sensitivities, respectively. I$_{r\ Sensor}$ decreased for $0 \leq P \leq 0.75$ bar and increased for P = 1 bar, $\lambda = 561$ nm. Error bars, $\pm$ 5 %, 9 % and 8 % for $\lambda = 514$ nm, 561 nm and 594 nm, respectively.

The like reproducibility of the measurements was also investigated. The result for $\lambda = 514$ nm, 561 nm and 594 nm showed good values of reproducibility (Figure 5.29).

a
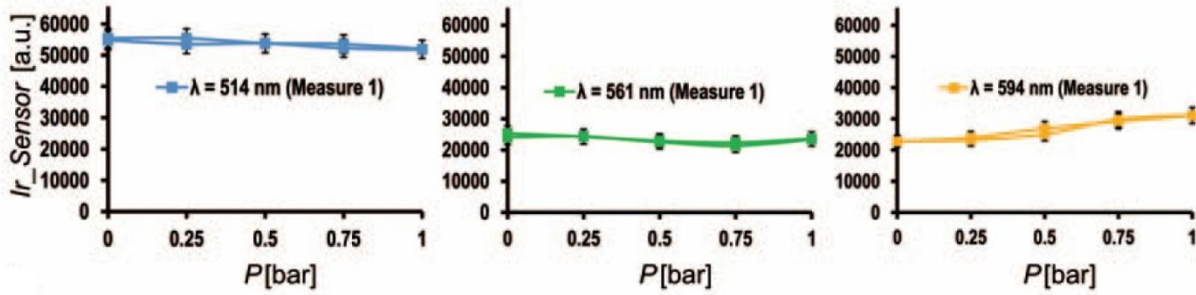
b
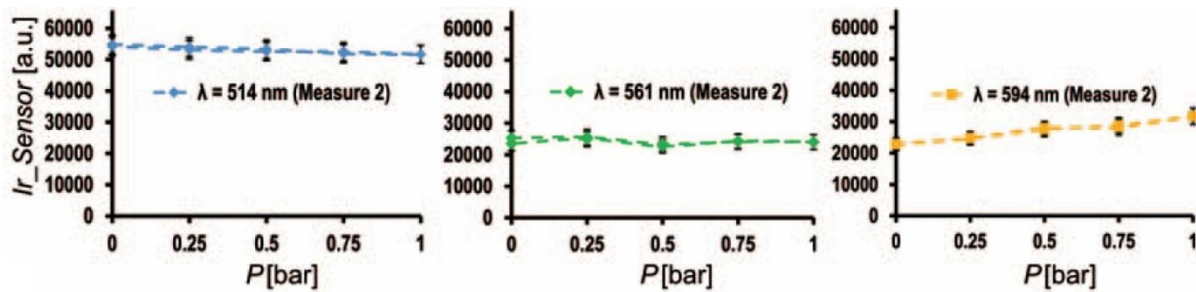
c
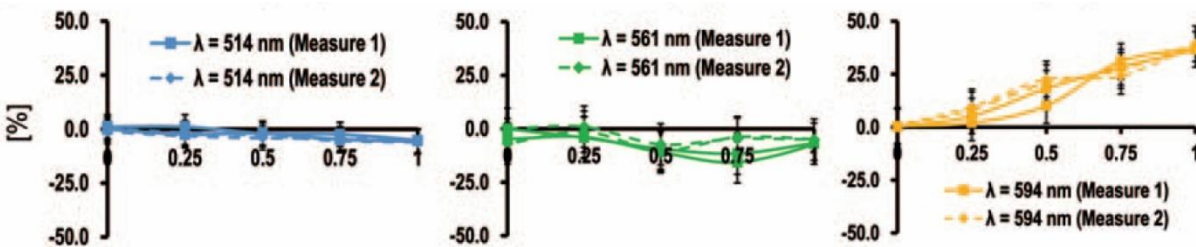
Figure 5.29: Reproducibility of the IPS. The $I_{r\text{ Sensor}}$ versus P ($\lambda = 514$ nm, 561 nm and 594 nm) for two cycles of measurements (0 bar/1 bar). a) Cycle of measurement 1 and b) cycle of measurement 2. c) Sensitivity comparison between the two cycles of measurements. Error bars, $\pm$ 5%, 9% and 8% for $\lambda = 514$ nm, 561 nm and 594 nm, respectively.

5.10 Pressure sensor in *HeLa* Living cells

(*Performed in partnership with Centro de Investigaciones Biológicas, CIB (CSIC)*)

Our works showed that the internalization of silicon-based microparticles were possible [19]. Thus, in this section the internalization of the fabricated IPS and their chemical stability inside the *HeLa* cells was evaluated. Cell-viability tests were performed in partnership with the Dr. Teresa Suarez group at CIB-CSIC.

5.10.1 Cell viability assays

HeLa cell line was selected for the biological experiments, as this cell line is a simple model for different studies about internalization of micro- and nanoparticles [27-31]. The chips were first mixed (0.5 - 1 chips/cell) with Lipofectamine 2000 (Invitrogen, Carlsbad, Ca, EE.UU.). *HeLa* cells were cultured in Dulbeccos modified Eagle medium (DMEM) and plated in well dishes (25000 cells/well), incubated with chip-containing liposomes and cultured in standard conditions for 12 h - 16 h. Cells were observed under a TCS SP2 AOBS CLSM with X63 oil immersion lens (Leica Microsystems GmbH). Green fluorescence was monitored with excitation and emission settings of $\lambda = 488$ nm and 505-550 nm, respectively. Red fluorescence was monitored with excitation and emission settings of $\lambda = 561$ nm and 580-610 nm, respectively. A 351 nm laser line was used to image nuclei, and fluorescence emission was measured at 415-460 nm. Chips were imaged with a $\lambda = 488$ nm laser line and they were detected by reflected light at $\lambda = 480$-495 nm. Time-lapse microscopy was performed with a Leica AF6000 LX model DMI6000B, and pictures were taken every 10 min.

Devices were easily localized by optical light microscopy because of the higher reflectivity of the polySilicon, and confocal laser scanning microscope showed the specific location of the chip into the cytoplasm. After lipofection a number of *HeLa* cells in the culture displayed vacuoles as a result of the procedure. The experiments showed that these vacuoles did not affect cell fitness or viability, and disappeared when cells were returned to normal culture conditions (Figure 5.30 and 5.31).
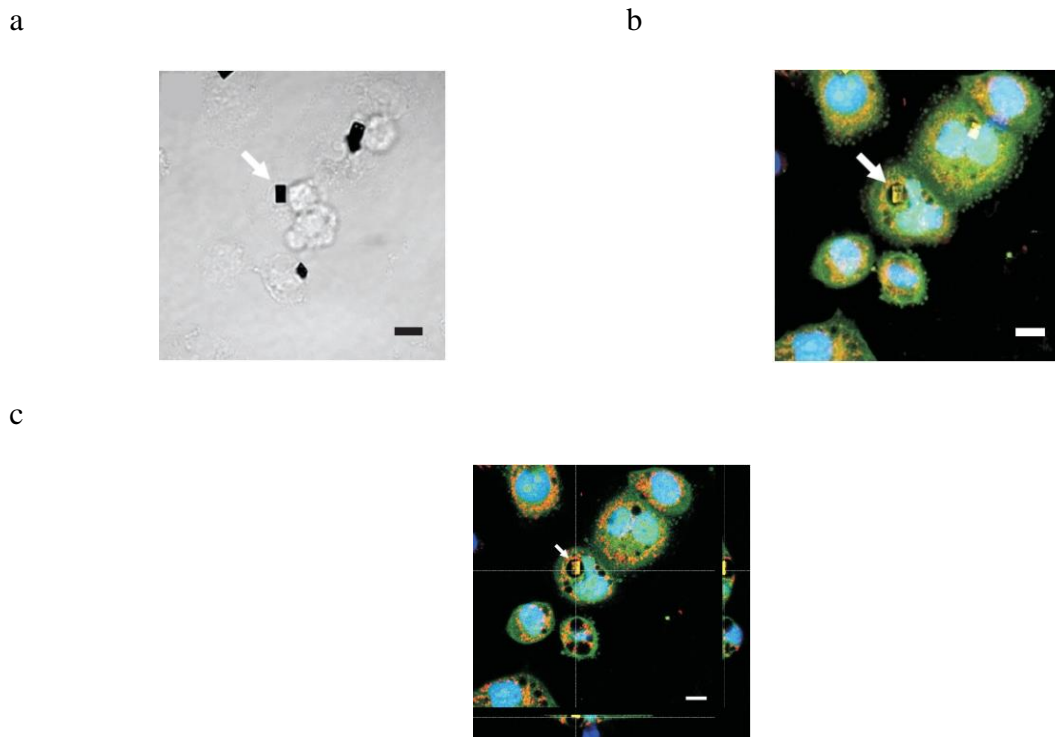
a   b

c

Figure 5.30: IPS inside a vacuole of a *HeLa* cell. A *HeLa* cell displaying an internalized device (white arrow) inside a vacuole. The cells were loaded with vital dyes CellTracker Green and MitoTracker Red before fixation. a) Transmitted visible light image. b) Overlay of confocal images. c) Orthogonal projection of confocal images showing the IPS inside the cell. Scale bars = 10 μm.
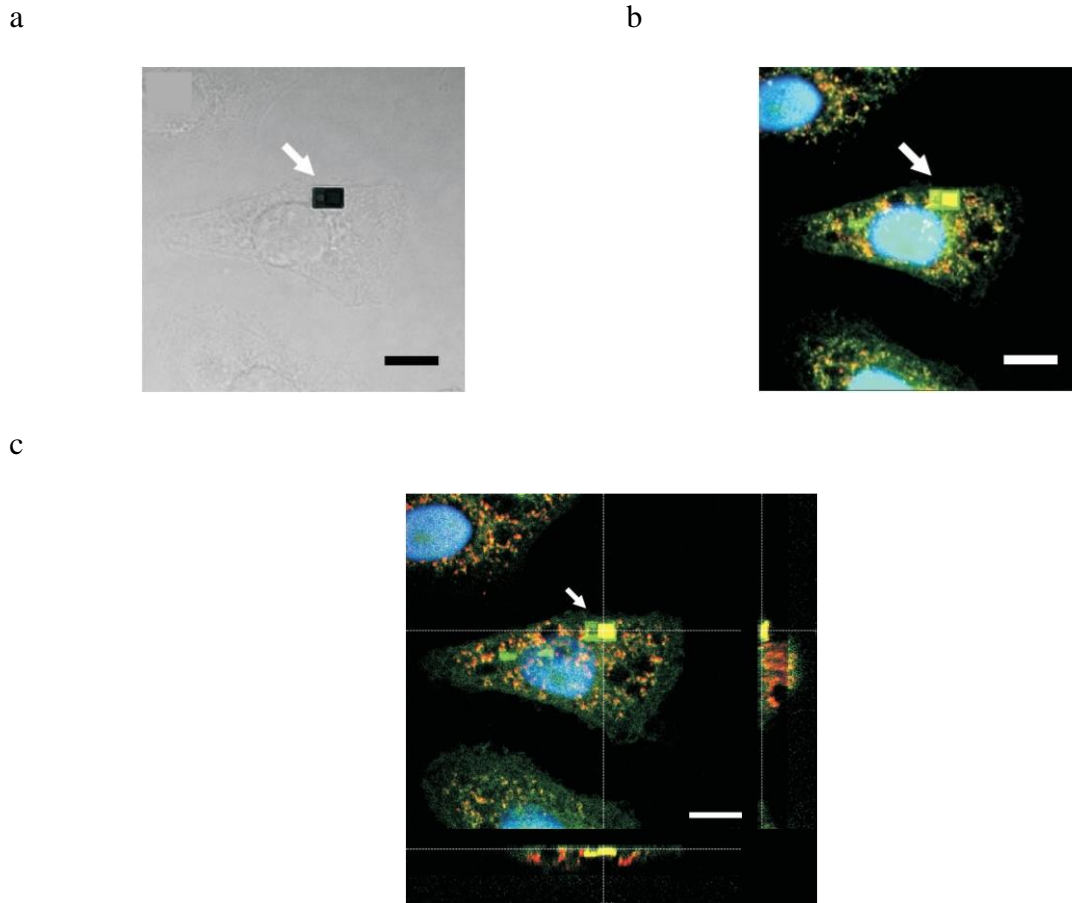
Figure 5.31: IPS systems inside the *HeLa* cell cytoplasm. A *HeLa* cell displaying an

internalized device (white arrow) inside the cell cytoplasm. The cells were loaded with vital

dyes CellTracker Green and MitoTracker Red before fixation. a) Transmitted visible light

image. b) Overlay of confocal images. c) Orthogonal projection of confocal images showing

the IPS inside the cell. Scale bars = 10 μm.

Additionally, analysis of the internalized devices and *HeLa* cell dimension-ratio were performed.

First, the projected area of a *HeLa* cell and its volume were estimated, the second assuming a

spherical shape of the cell. Second, chip volume and maximum projected area were calculated.

Third, chip/*HeLa*-cell ratio of volume and area were also estimated showing that the internalization only represented 0.2% of the total volume of the typical *HeLa* cell (Table 5.2). In spite of the fact that the area of the IPS can look relatively large when is compared to the area of a *HeLa* cell (Figure 5.32a), the volume ratio is very small. Geometrical calculations showed that the chip/*HeLa*-cell area-ratio is 10%. However, what it is expected to be relevant for cell functioning is the chip/*HeLa*-cell volume-ratio, which is lower, as the devices are extremely thin (Figure 5.32b).

a

	Area$[um^2]$	Volume $[um^3]$
HeLa Cell	~ 229	~ 2600

b

	Area$[um^2]$	Volume $[um^3]$
NOMS	24	5

c

	Area$[um^2]$	Volume $[um^3]$
NOMS/HeLa Cell	$\sim 10\%$	$\sim 0.2\%$

Table 5.2: IPS and *HeLa* cell dimension-ratio numerical analysis. a) Estimated *HeLa* cell volume assuming a spherical shape. b) Device volume and maximum projected area on an image. c) Devices/*HeLa* cell ratios of the volume and area values.
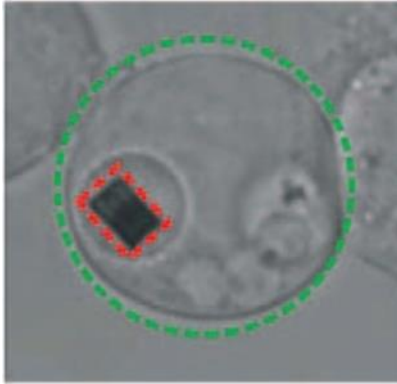
a   b

Figure 5.32: IPS and *HeLa* cell dimension-ratio image analysis. Images of *HeLa* cells with

a) an aligned (with the plane of the image) internalized IPS and b) not aligned IPS. Scale bars

= 10 μm.

Cell viability assays with stained techniques like Nile Red, MitoTracker red and Calcein-AM

(green) were performed (Figure 5.33 and 5.34). These techniques are used as structural

biological tests for cell physiological function. Nil red is the most common dye for cell lipids,

and Calcein *AM* is a cell-permeant dye to determine cell viability in most eukaryotic cells. In

living cells the non-fluorescent Calcein AM is converted to a green-fluorescent Calcein, and

MitoTracker red is only incorporated into the mitochondria of living cells.

Additionally, to display mitochondria activity, lipofectamine transfected *HeLa* cells were stained

with the mitochondrial potential-dependent probe DiOC and observed by CLSM. Despite the

number of mitochondria per cell, no significant differences in maximum intensities were found

between living cells with or without IPS (Figure 5.35).
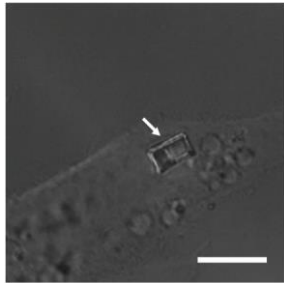
a   b
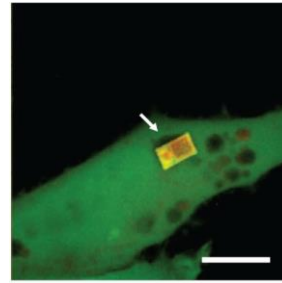
Figure 5.33: Cell viability assays-Nile Red/Calcein-AM. *HeLa* cell after transfection with an internalized device inside a vacuole stained with Nile Red and the vital probe Calcein-AM (green). a) Optical Nomarski image. b) CLSM overlay projection image (white arrows indicate the internalized IPS). Scale bars = 10 µm.
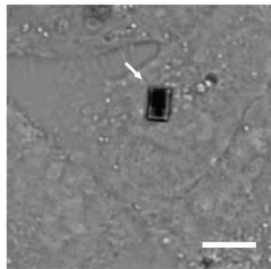
a   b
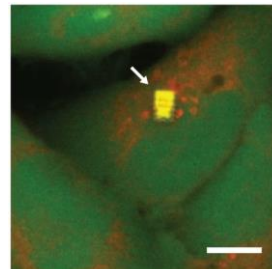
Figure 5.34: Cell viability assays-Mitotracker red / Calcein-AM. *HeLa* cell 24h after lipofection with an internalized device inside its cytoplasm stained with MitoTracker red and the vital probe Calcein-AM (green). a) An optical Nomarski image. b) Devices overlay the projection image with the IPS (white arrows indicate the internalized IPS). Scale bars = 10 µm.

a b c
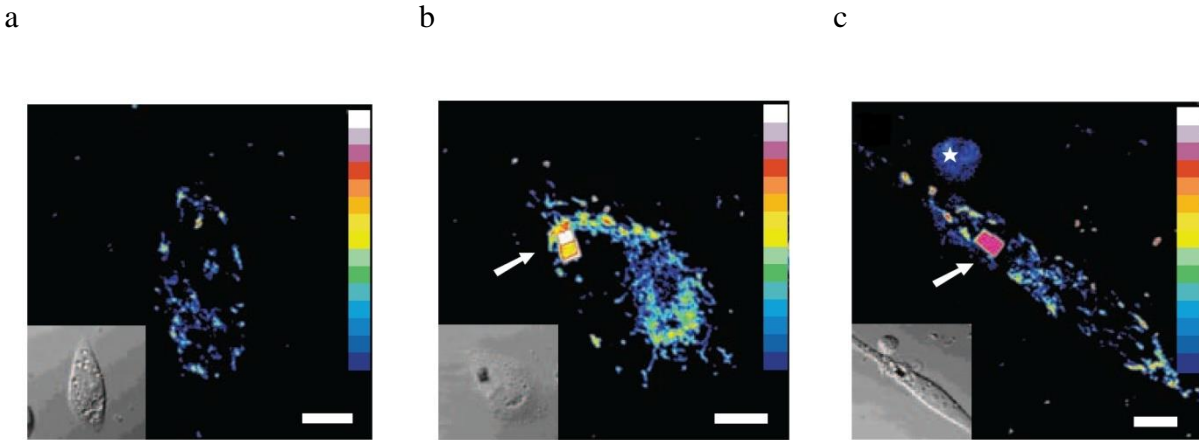
Figure 5.35: Cell viability assays - Mitochondria activity. Lipofectamine transfected *HeLa* cells were stained with the mitochondrial potential-dependent probe DiOC and observed by CLSM. a) Cell without IPS. b) Cell containing an IPS. c) Cell containing an IPS inside a vacuole. Dead cells showed a clear decrease in mitochondrial DiOC staining and pixel mean intensity (star). Pixel mean intensity was measured and pseudo-colored. Insets show Nomarski images. Scale bars = 10 μm.

Remarkably, sensor-containing *HeLa* cells, with or without, vacuoles showed a normally division (Figure 5.36).
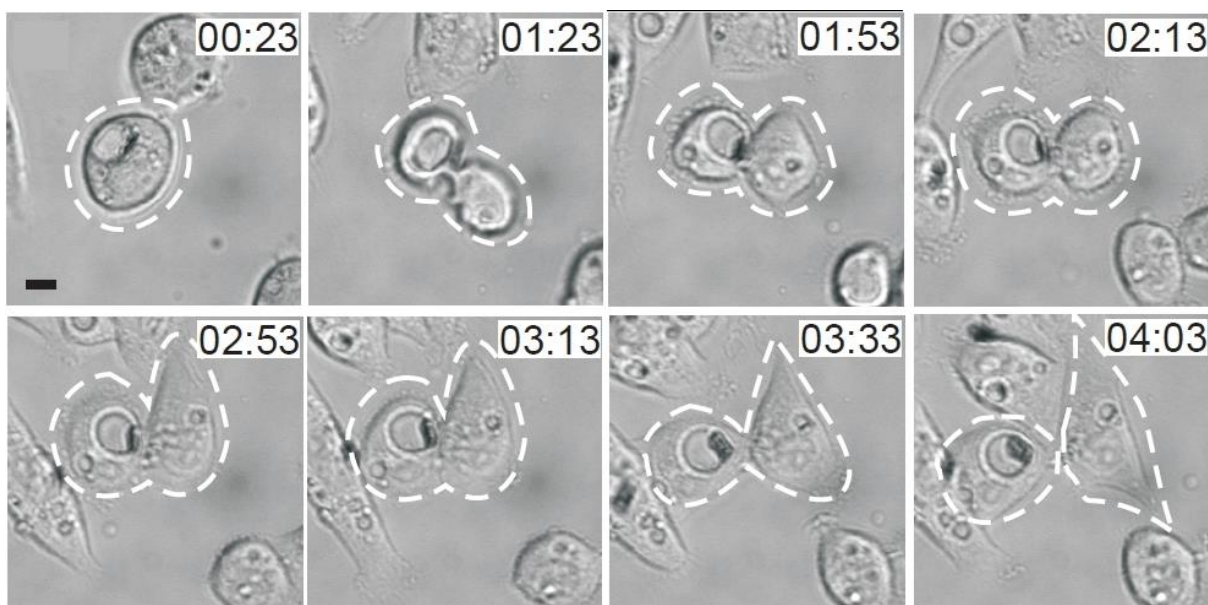
Figure 5.36: IPS validation inside Human Cells. A *HeLa* cell, containing devices inside a vacuole, show normal division (time format is hh:mm). Scale bars = 10 μm.

5.10.2 Device stability inside cells

After the internalization of the IPS, the pH value of a selected vacuole was analyzed to determine how this value can be affected by the presence of intracellular devices. Briefly, after 1h incubation with 10 μM of the probe, cells were washed with fresh medium to remove excess of the probe and observed under a TCS SP2 AOBS CLSM with 63X oil immersion lens (Leica Microsystems GMbH, Germany). Another set of IPS transfected *HeLa* cells were alternatively exposed to pH-calibration buffers (pH 4, 5, 6 and 7) in the presence of 10 μM nigericin to obtain pH calibration images. Measurement of pH values was performed by a Lysosensor Yellow/Blue DND-160 according to the manufacturer instructions, and images of emissions at $\lambda = 540$ nm and 450 nm with excitation line at $\lambda = 351$ nm were processed with Ratio-Plus plugin (ImageJ) to

obtain the vacuole pH (Figure 5.37). Most vacuoles, containing IPS, showed a pH between 4 and 6. These weak acidic values (silicon is commonly etched in high basic solutions as KOH) and the fact that any remarkable unexpected change was observed on the performance of the IPS would confirm a non-relevant degradation rate for the time scale of the experiments.

a

b
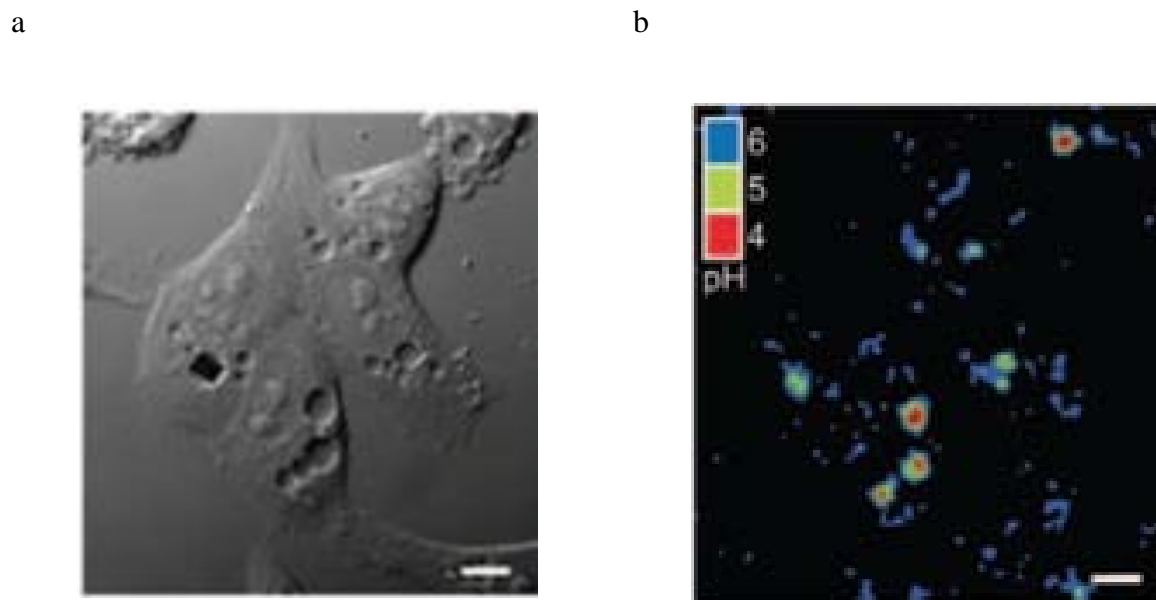
Figure 5.37: Assay of the stability of the IPS inside cells depending on the pH value. Vacuole pH was measured with a pH-sensitive probe Lysosensor Blue/Yellow DND-160 according to the specifications of the manufacture. Scale bars = 10 μm.

Additionally, *HeLa* cells after 9 days of the lipofection showed non-degraded devices, confirming the stability of the devices (Figure 5.38).
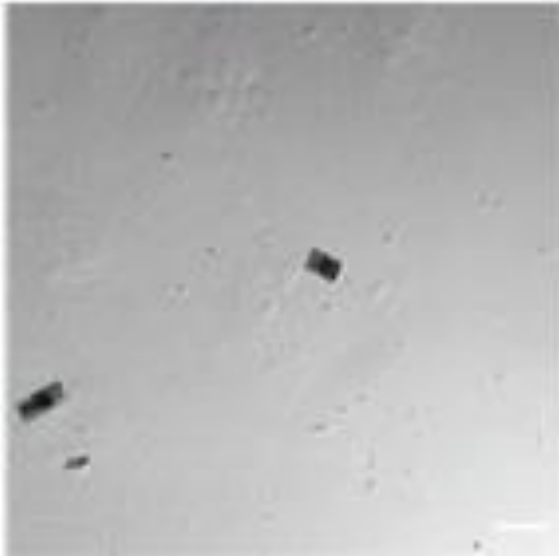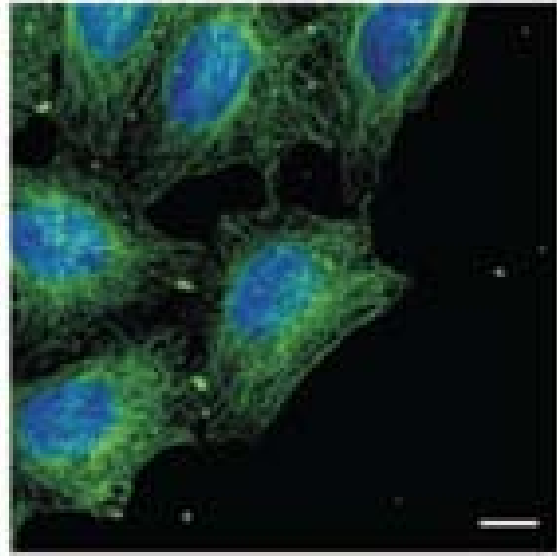
Figure 5.38: Non-degradation assay of the stability of IPS. *HeLa* cells after 9 days of the lipofection showed non-degraded devices. a) An optical Nomarski image. b) A staining nuclei (blue) and tubulin (green) showing cell integrity. Scale bars = 10 µm.

These results are in good agreement with the finding that polySilicon was not degraded in buffered solutions at pH values between 4 and 9 (Figure 5.13)

5.11 Extracellular pressure transmission into *HeLa* cells

Extracellular pressure on a living cell is a common load in many real situations. For instance, Human cells experience pressure changes $\Delta P = 0,2$ bar from feet to head. And this value can even increase during human activity, and deep-sea animals can be exposed to 200 bar upon diving [32]. Hard-wire tensegrity models postulate that the cytoskeleton can resist some mechanical forces [33]. The experiments described in the next sections support the supposition

that the cytoskeletons of Human *HeLa* cells do not mechanically withstand extracellular pressures in the studied range and under our experimental cell culture conditions.

5.11.1 Imaging acquisition during the pressure experiments

The fabricated IPS were validated using CLSM, and *HeLa* cells were incubated for 12 h – 16 h in lipofection medium, a protocol previously described [19]. Cells were grown on glass coverslips and observed under the CLSM inside a live-imaging Ludin chamber following the experimental setup describe at Figure 5.22.

For CLSM analysis, confocal images were acquired with a confocal Leica TCS-SP5 microscope (Leica Microsystems GmbH), using λ = 514 nm, 561 nm and 594 nm excitation laser wavelengths ((AOTF) = 1%). The confocal analysis was conducted in the acousto-optical beam splitters (AOBS) reflection mode, with 16 bit-depth resolution and in the XYZ scan mode. A X63 /0.9 HCX APO water objective (Leica Microsystems GmbH) was used. The image acquisition time was ~ 25 s. The images were pre-analyzed by LAS AF software (Leica Microsystems GmbH).

Next, the mechanical transmission of the extracellular pressure to a subcellular component was analyzed. The presence of an IPS inside a vacuole had several inherent advantages. First, it can give information about how an external pressure is transmitted mechanically to organelles. Second, it prevents the eventual existence of mechanical cross-sensitivity on the devices because of other organelles or cytoskeletal filaments, which can induce small forces and displacements (Figure 5.3). Third, high vertical-resolution and reduced out-of focus-blur images can be obtained by using CLSM (Figure 5.39). Finally, the presence of IPS inside vacuoles also

improves the imaging optical quality as it ensures a more uniform refractive index of the surrounding medium (Figure 5.40).
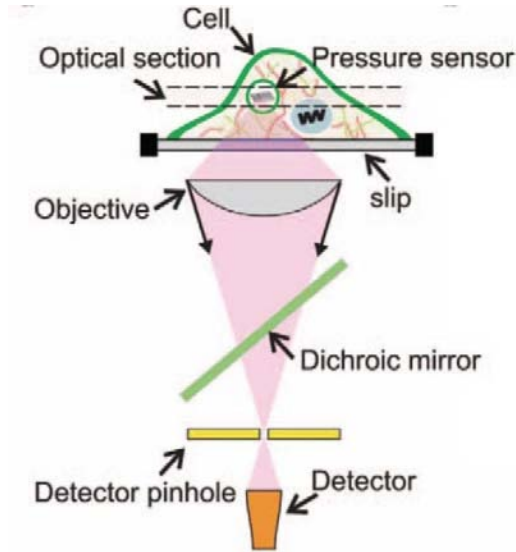
Figure 5.39: Scheme of a confocal detection by laser scanning microscope of an IPS. Emitted reflected light from the in-focus pressure sensor is focused at the detector pinhole and the reach detector.

a   b

Figure 5.40: CSLM image quality. Representative reflective images (left) and displays of a three dimensional graph of the intensities of pixels framed at centre of the membrane (right) for chips a) in air and b) inside a vacuole.

5.11.2 Extracellular pressure transmission assays

After the IPS internalization, an external pressure from 0 to 1 bar and form 1 to 0 bar was applied. Overlaid images of transmitted light laser channels, the vacuole and different parts of the pressure sensor can be easily recognized (Figure 5.41).

a   b   c   d
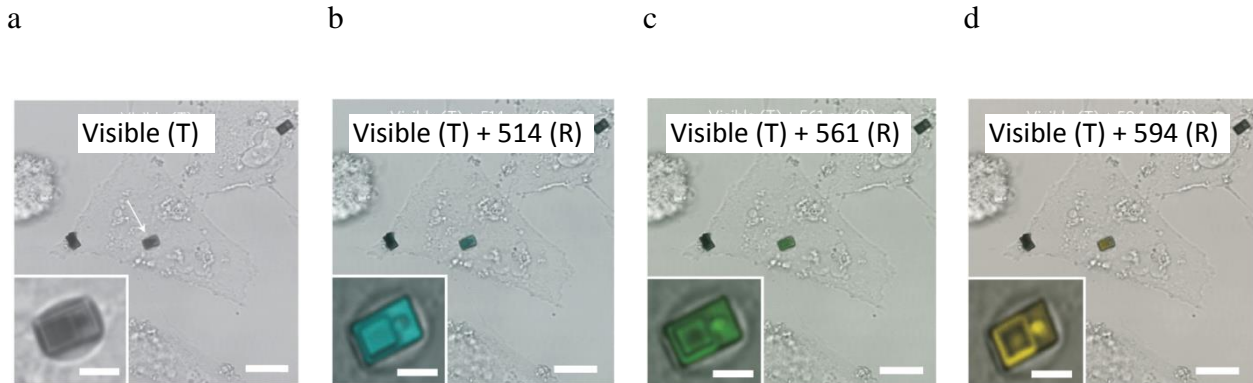
Figure 5.41: Pressure sensors inside living cells. False-color 16-bit confocal laser scanning microscope images of *HeLa* cells with an IPS inside a vacuole (white arrow). From a to d, images show the cells under transmitted visible light (T) and the reflected (R) light of selected lasers ($\lambda = 514$, 561 and 594 nm). Insets: A detail of the IPS inside a vacuole. Scale bars = 20 μm (main images), 5 μm (insets).

Next, CLSM experiments with pressure increased from 0 to 1 bar and decreased from 1 to 0 bar were performed. $I_{r\ Sensor}$ versus P (from 16-bit images) was monitored (Figure 5.42). A comparison between $I_{r\ Sensor}$ inside the vacuole (Figure 5.42) and the calibrated sensor in air (Figure 5.28) shows similar proportional changes, and confirmed that the extracellular pressure is transmitted into the vacuole. Thus, extracellular pressure is transmitted through the cytosol to the

inner compartments (Figure 5.43). The implication is that intracellular transmission of fluid pressure follows the Pascal's law.

a

b

c
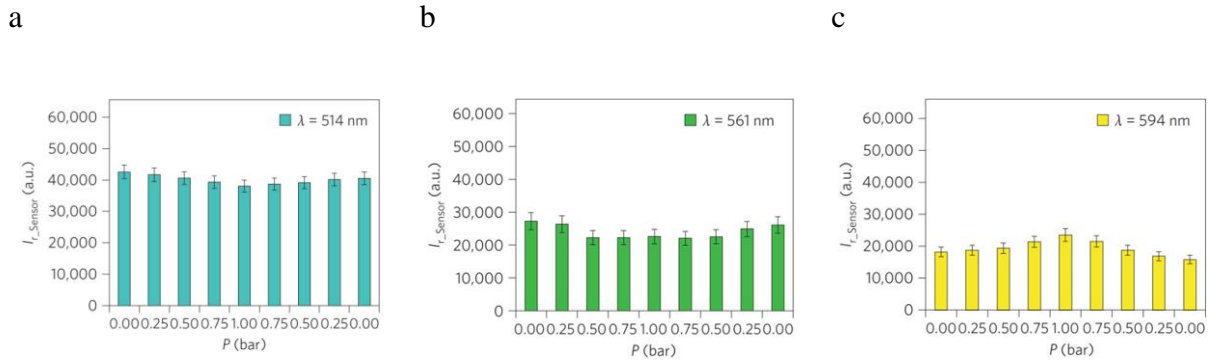
Figure 5.42: Transmission of the extracellular pressure to inner of the cell. $I_{r\ Sensor}$ versus applied pressure (P). Lasers with $\lambda = 514$ nm, 561 nm and 594 nm show positive and negative sensitivities, respectively. $I_{r\ Sensor}$ decreased for $0 \leq P \leq 0,75$ bar and increased for $P = 1$ bar, $\lambda = 561$ nm. Error bars, +5%, 9% and 8% for $\lambda = 514$ nm, 561 nm and 594 nm, respectively (based on measurement uncertainty from images).

a

b
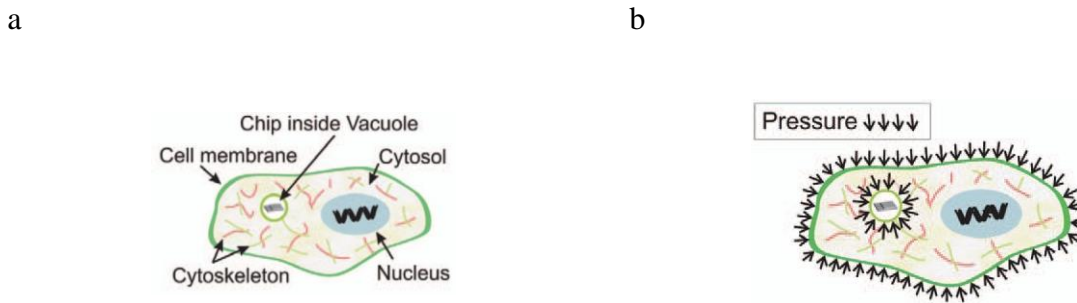
Figure 5.43: Schematic representation of the pressure transmission to the subcellular compartments. a) Drawing of an eukaryotic cell showing the cytosol, cell membrane and cytoskeleton, which provide the mechanical integrity of the cell, and some subcellular components, such as a vacuole with a IPS inside. b) Schematic picture of how the applied

extracellular pressure can be propagated through the cytosol inside the cell and the subcellular compartments.

The analysis showed in figure 5.44 demonstrates the capability of detecting pressure fluctuations inside a cell. This figure compares pressure data for IPS inside cell and IPS in air. Previous to this study, a parallel optical simulation was done to demonstrate the influence of the media on the FP optical spectrum, which showed that, although, the reflection from the sensor depends on the optical properties of the surrounding media (vacuole or air), the position of the resonance is almost invariant (Figure 5.44a).

Two statistical analysis (through Graph Pad Prism 4 software) were used. First, analysis of variance (ANOVA) and a Bonferroni test, to compare intra-group data (inside cell or inside air), and second, $\chi 2$ test to compare pressure data from calibration IPS in air versus IPS inside cells. These statistical results were: *P< 0.05; **P<0.01; ***P<0.001 (ANOVA, Bonferroni test) and, no significant differences were found between the IPS performance in air and inside cells ($\chi 2$ test, P = 0.6922), Figure 5.44b.
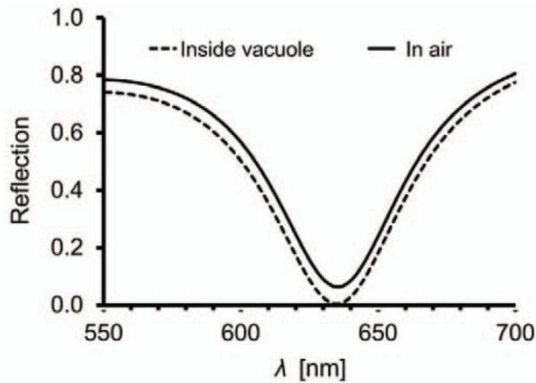
a   b
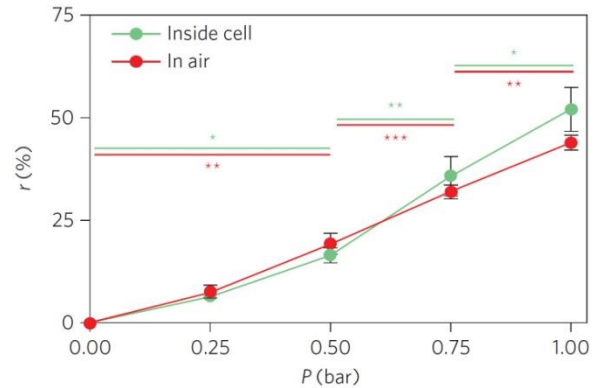
Figure 5.44: Comparison of the device performance inside cell versus in air data set results. a) An optical simulation of the reflection versus the λ for a chip immersed inside a vacuole and the use of a chip for calibration of the asymmetrical structure "air-sensor-glass".

b) Graph showing (r) = ($I_{r\ Sensor}$(P, λ = 594 nm)/$I_{r\ Sensor}$(P, λ = 514 nm))/($I_{r\ Sensor}$(P = 0, λ = 594 nm)/ $I_{r\ Sensor}$(P= 0, λ = 514 nm))$^{-1}$ for IPS in air and inside cells. Data are presented as the mean ± s.e.m. of five independent observations.

Finally, it was analyzed if non-specific adsorption of intracellular biomolecules on the IPS surface could induce a deformation on the membranes, varying the output of the sensor ($I_{r\ Sensor}$). First, mechanical simulations showed that this effect is very small compared with the values of the studied pressure (Figure 5.4). And second, from biological point of view, fluorescent-lipofectamine (red), Metafectene FluoR (Biontex), showed that IPS were still wrapped with this molecule 5 days after internalization (Figure 5.45), which should avoid non-specific adsorption of intracellular biomolecules on the sensors surface, that could induce a deformation of the membranes varying the readout measurement of the IPS. In addition, the pressure sensitivity of

the IPS was not affected by the presence of lipofectamine, as measurements of IPS inside cells (with lipofectamine) and IPS in air (without lipofectamine) show similar results (Figure 5.44a)

a   b   c
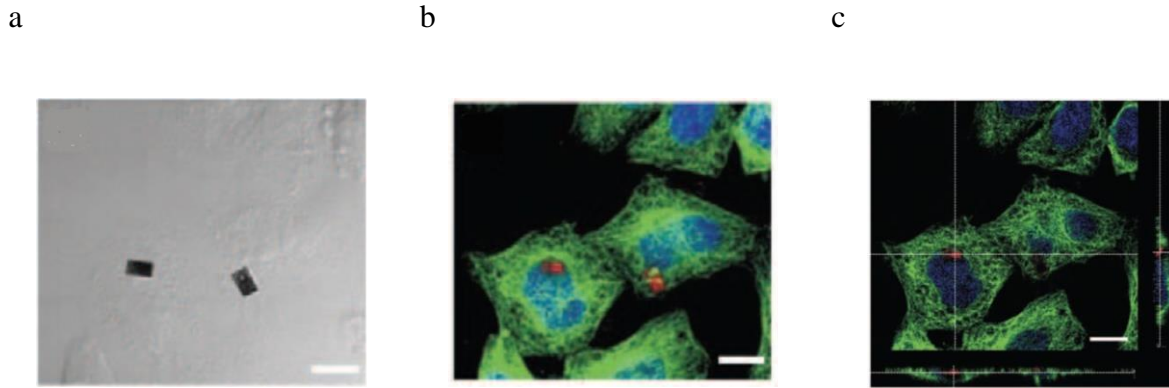
Figure 5.45: Surface stress cross-sensitivity due to non-specific biomolecular adsorption. Fluorescent-lipofectamine (red) and Metafectene FluoR (Biontex) showed that IPS were still wrapped with this molecule 5 days after internalization. Scale Bars = 10 µm.

5.12 Intracellular pressure change during an osmotic shock

To finish this studies, the effect of the exposure of *HeLa* cells to an osmotic shock (1/10 water dilution of the standard cell medium) was analyzed. Osmotic shock or osmotic stress is a sudden change in the solute concentration around a cell, causing a rapid change in the movement of water across its cell membrane.

First, a new batch of IPS was fabricated showing a minimum reflection of the spectrum at $\lambda = 490$ nm. The induced osmotic pressure predicted by Van´t Hoff law [38] is expected to produce a hydrostatic pressure of $P \sim 7$ bar inside the cell. Accordingly, the predicted osmotic shock pressure should shift the Fabry-Pérot resonator minimum reflection by $\lambda \sim 42$ nm. Second, the

HeLa Cells were exposed to an osmotic shock, where DMEM medium with 10% fetal bovine serum (Molecular Probes, Invitrogen) was 10% diluted in deionized water and perfused in the Ludin chamber.

Next, IPS located in a sub-cellular (vacuole) compartment and in the cytosol of *HeLa* cells before and after the osmotic shock were studied. Transmission and reflection images of *HeLa* cells in isosmotic and hypoosmotic medium were acquired. The chip reflective images at the different wavelengths (where the minimum reflection of the spectrum appears centered between $\lambda = 476$ nm and $\lambda = 488$ nm in both cases) is showed (Figure 5.46). This result implies a practically null shift of the spectrum in contrast with the expected $\Delta\lambda \sim 42$ nm in a semipermeable membrane due to the osmotic shock.

a
b
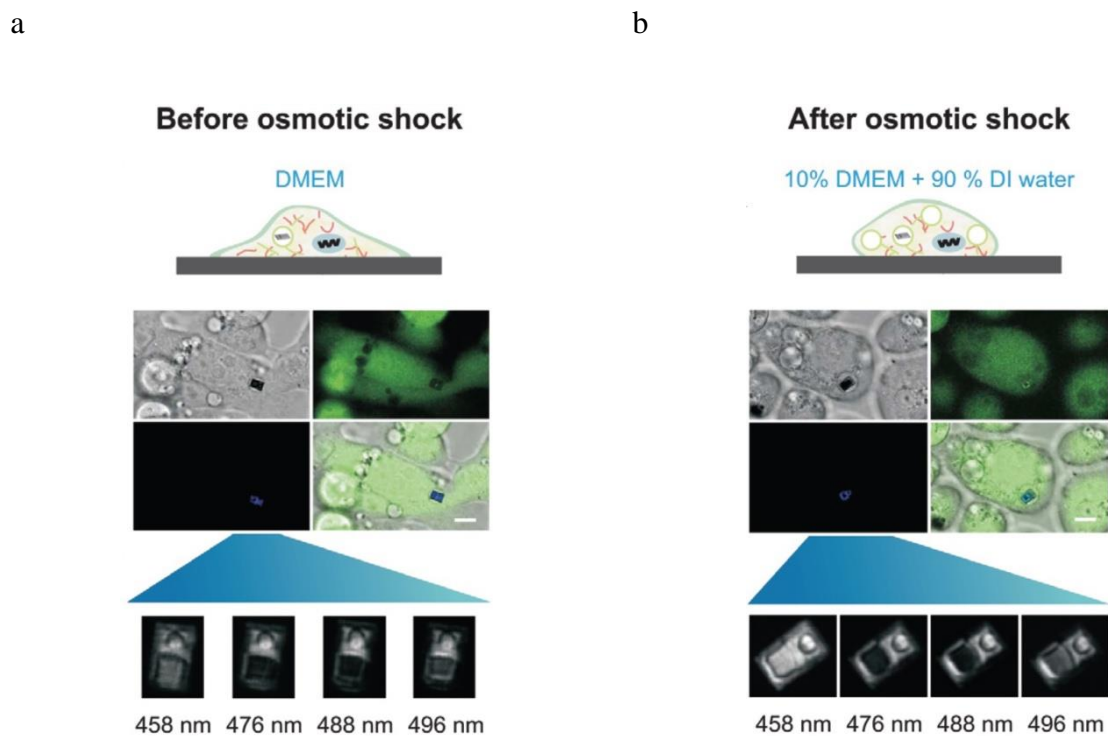
Figure 5.46: The *HeLa* cells in hypoosmotic medium. Schematic representation of the cells (a) before and (b) 1 hour after replacing the cell culture media to reduce the osmolarity.

A final analysis of the optical $I_{r\ Centre}$ spectrum, inside *HeLa* cell before and after the osmotic shock, demonstrated that de reflection profiles were practically the same (Figure 5.47). Additionally, extrapolating this wavelength data for a minimum reflection (the minimum correspond with those first derivative of the function was zero), by adjusting the mean intensities for the five selected laser to a second-order polynomial, a similar results was exhibited (Figure 5.48).

a
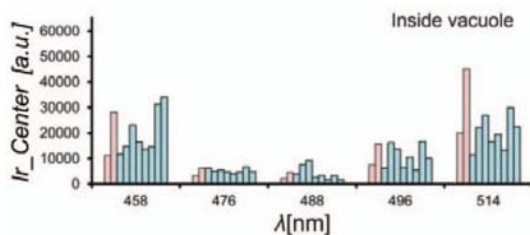
b
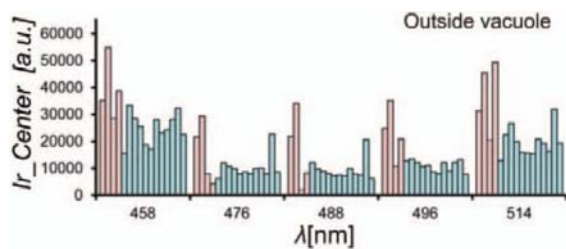
Figure 5.47: The optical spectrum of IPS inside *HeLa* cells before and after the hypoosmotic shock. $I_{r\ Centre}$ for the selected lasers ($\lambda = 458$ nm, 476 nm, 488 nm, 496 nm and 514 nm) of IPS, a) inside a vacuole and b) in the cytosol before (red) and after (blue) the osmotic shock. In all the cases λ for the minimum reflection is roughly between the $\lambda = 476$ nm and 488 nm.
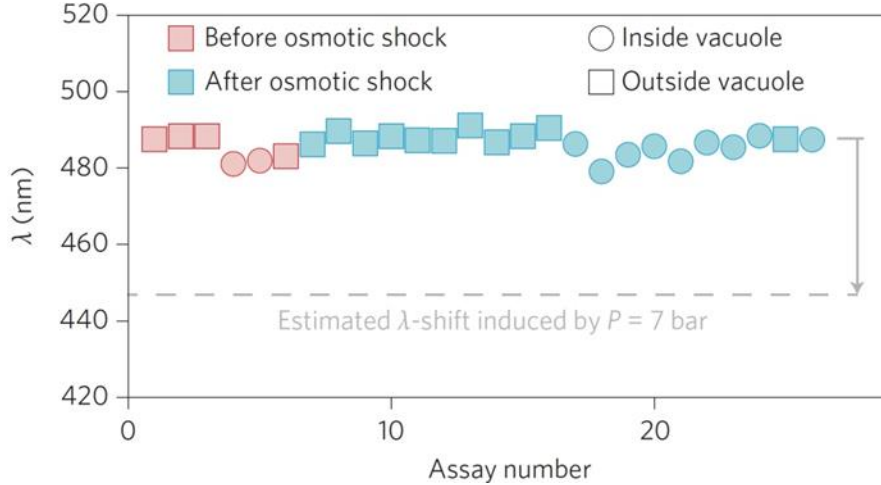
Figure 5.48: Extrapolated wavelength for the minimum reflection of IPS. Extrapolated wavelength for the minimum reflection of IPS in the cytosol and inside the vacuole before and after an osmotic shock, showing a non-significant shift of the reflected spectrum after the shock.

5.13 Discussions and Conclusions

A NanoOptoMechanical System as an Intracellular Pressure Sensor have been successfully designed and fabricated. Taking advantages of the polySilicon technology growth layer limits, a nanomechanical chip that can be internalized to detect intracellular pressure changes within living cells, was fabricated. First, a system with two membranes separated by a vacuum gap (constituting a Fabry-Pérot resonator) and an optical reference area were designed. Second, an interrogation method based on confocal laser scanning microscopy (CLSM), was implemented. Nanomechanical devices were manufactured because it was possible to grow 50 nm-thick non-porous layers of polySilicon. In addition, these devices can be collected and suspended for their

posterior use on cell cultures. Nanomechamical devices through Bright-field and CLSM optical microscope techniques were validated. Analytical and simulated analyses showed that mechanical deformation was highly dependent on the membrane thickness and the linear response versus pressure in the range of few bars.

Cell viability and chip internalization assays have been performed in *HeLa* cells and not revealed cell toxicity. Specific chip localizations in the cytoplasm or in subcellular compartments like vacuoles, by optical light or CLMS microscopy, not affecting cell fitness or viability, was showed. Additionally, normal cellular division and mitochondria activity, in cells with or without devices 9 days later, was founded. No device degradation inside a living cell, due to vacuole internal pH oscillation between 4 and 6 after 9 days later lipofection, was founded. Devices inside the cytosol or inside vacuole were demonstrated to detect pressure changes. The devices also confirm that the extracellular pressure is transmitted inside *HeLa* cells and also inside to its organelles as a vacuole. In addition, the devices also demonstrate that the *HeLa* cells can compensated an osmotic shock without a detectable increment in the intracellular pressure.

Additional work remains to be carried out to increase the sensitivity of the IPS to obtain accurate pressure measurements; further developments include thinner mechanical layers, autofocus and tilt-stage systems, and computer-assisted measurements.

Biomolecular adsorption phenomena should be considered in future work, where detecting pressures below millibars will be required. The surface stress effects will be important if their value changes during the measurement acquisition. Surface stress loads before the acquisition

would only change the offset of the IPS but not the measurements as the IPS is a differential pressure sensor. Furthermore, is also observed that Ir Sensor is reversible, demonstrating that the pressure inside the vacuole follows extracellular pressure changes.

For this work, the result shows that cross-sensitivities are not relevant. Additionally, mechanical forces are not very well understood and are involved in basic cellular processes such as cell migration [39, 40], diseases [41 - 43] and development [44]. The presented Intracellular Pressure Sensor will provide information directly from inside the cellular environment about these cellular forces and will provide new opportunities.

This work is a first step towards a wide-ranging field of intracellular nanochips that will offer a different perspective on fundamental problems in cell biology.

Bibliography

[1] M. P. Stewart, J. Helenius, Y. Toyoda, S. P. Ramanathan, D. J. Muller and A. A. Hyman. Nature 469, 226230 (2011)

[2] R. P. Rand, A. C. Burton. Biophys. J. 4, 115135 (1964)

[3] R. Strohmeier, J. Bereiterhahn. Cell Sci. 88, 631640 (1987)

[4] S. M. Kelly, P. T. Macklem. Am. J. Physiol. 260, C652C657 (1991)

[5] G. Hernandez. Cambridge, Fabry-Pérot Interferometers. Cambridge University Press (1988).

[6] J. M. Vaughan. The Fabry-Pérot interferometer : history, theory, practice and applications. The Adam Hilger series in optics and optoelectronics (1989)

[7] R. Paschotta. Encyclopedia of Laser Physics and Technology: Rabi oscillations (2005)

[8] G. M. Whitesides. Nature Biotechnol. 21, 11611165 (2003)

[9] R. Singhal, Z. Orynbayeva, R. V. K. Sundaram, J. J. Niu, S. Bhattacharyya, E. A. Vitol, M. G. Schrlau, E. S. Papazoglou, G. Friedman, Y. Gogotsi. Nature Nanotech. 6, 5763 (2011)

[10] B. Tian, T. Cohen-Karni, Q. Qing, X. Duan, P. Xie, C. M. Lieber. Science 329, 830834 (2010).

[11] J. L. Arlett, E. B. Myers, M. L. Roukes. Nature Nanotech. 6, 203215 (2011)

[12] S. E. Cross, Y. S. Jin, J. Rao and J. K. Gimzewski. Nature Nanotech. 2, 780783 (2007)

[13] N. Q. Balaban, U. S. Schwarz, D. Riveline, P. Goichberg, G. Tzur, I. Sabanay, D. Mahalu, S. Safran, A. Bershadsky, L. Addadi, B. Geiger. Nature Cell Biol. 3, 466472 (2001).

[14] A. Vaziri, A. Gopinath. Nature Mater. 7, 1523 (2008).

[15] J. Y. Fan, P. K. Chu. Small 6, 20802098 (2010)

[16] E. Tasciotti, X. Liu, R. Bhavane, K. Plant, A. D. Leonard, B. K. Price, M. Ming-Cheng Cheng, P. Decuzzi, J. M. Tour, F. Robertson, M. Ferrari. Nature Nanotech. 3, 151157 (2008)

[17] E. Fernández-Rosas, R. Gómez, E. Ibañez, L. Barrios, M. Duch, J. Esteve, C. Nogués, J. A. Plaza. Small 5, 24332439 (2009)

[18] S. Novo, L. Barrios, J. Santaló, R. Gómez-Martínez, M. Duch, J. Esteve, J. A. Plaza, C. Nogués, Elena Ibañez,Human Reprod. 26, 96105 (2011).

[19] R. Gómez-Martínez, P. Vázquez, M. Duch, A. Muriano, D. Pinacho, N. Sanvicens, F. Sánchez-Baeza, P. Boya, E. J. de la Rosa, J. Esteve, T. Suárez, J. A. Plaza. Small 6, 499502 (2010)

[20] N. S. Claxton, T. J. Fellers, M. W. Davidson. Laser scanning confocal microscopy Department of Optical Microscopy and Digital Imaging. National High Magnetic Field Laboratory. Florida State University, 37, Unpublished (2005)

[21] J. B. Pawley. Handbook of Biological Confocal Microscopy. Third Edition. Springer (2006)

[22] C. W. Chau. Laser Scanning Theory and Applications. Intech (2011)

[23] M. Born, E. Wolf. Principles of Optics. 6th edition. Pergamon (1980).

[24] P. J. French. Sens. Actuat. A 99, 312 (2002).

[25] G. Mohamed. Design and Fabrication 2nd Edition (CRC, 2005)

[26] S. Timoshenko, S. Woinowsky-Krieger. Ed., Theory of Plates and Shells (McGraw-Hill, NY 1959)

[27] S. E. Gratton, P. A. Ropp, P. D. Pohlhaus, J. C. Luft, V. J. Madden, M. E Napier, J. M. DeSimone. Proc. Natl. Acad. Sci. U.S.A, 105 (33), 11613 (2008)

[28] I. Slowing, B. G. Trewing, V. S. Lin. J. Am. Chem. Soc. 128 (46), 15792 (2006)

[29] Y. Pan, S. Neuss, M. Leifert, F. Wen, U. Simon, G. Schmid, W. Brandau, W. Jahnen-Dechent. Small 3 (11), 1941 (2007)

[30] I. Slowing, B. G. Trewing, V. S. Lin. J. Am. Chem. Soc. 129 (28), 8845 (2007)

[31] M. Semmling, O. Kreft, J. A. Munoz, G. B. Sukhorokov, J. Kas, W. J. Parak. Small 4 (10), 1773 (2008)

[32] K. A. Myers, J. B. Rattner, N. G, Shrive, D. A. Hart. Cell Biol. 85, 543551 (2007)

[33] D. E. Ingber. J. Cell Sci. 116, 11571173 (2003)

[34] M. Borgnia, S. Nielsen, A. Engle, P. Agre. Annu. Rev. Biochem. 68, 425458 (1999)

[35] C. Spagnoli, A. Beyder, S. Besch, F. Sachs. Phys. Rev. E 78, 031916 (2008)

[36] J. D. Finan, F. Guilak. J. Cell Biochem. 109, 460467 (2010)

[37] A. Pietuch, B. R. Bruckner, A. Janshoff. Biochim. Biophys. Acta Mol. Cell Res. 1833, 712722 (2013)

[38] J. H. vant Hoff. Zeitschrift fur Physikalische Chemie, 1, 481493 (1887)

[39] D. T. Tambe, C. C. Hardin, T. E. Angelini, K. Rajendran, C. Y. Park, X. Serra-Picamal, E. H. Zhou,M. H. Zaman, J. P. Butler, D. A. Weitz, J. J. Fredberg, X. Trepat. Nature Mater. 10, 469475 (2011)

[40] X. Trepat, M. R. Wasserman, T. E. Angelini, E. Millet, D. A. Weitz, J. P. Butler, J. J. Fredberg. Nature Phys. 5,426430 (2009)

[41] C. C. DuFort, M. Paszek, V. M. Weaver. Nature Rev. Mol. Cell Biol. 12, 308318 (2011)

[42] D. E. Jaalouk, J. Lammerding. Nature Rev. Mol. Cell Biol. 10, 6373 (2009)

[43] A. Fritsch, M. Höckel, T. Kiessling, K. D. Nnetu, F. Wetzel, M. Zink, J. A. Käs. Nature Phys. 6 730732 (2010)

[44] M. A. Wozniak, C. S. Chen. Nature Rev. Mol. Cell Biol. 10, 3443 (2009)

Chapter 6

General Conclusions and Future Work

Along the chapters of this doctoral thesis, the technology development for Intracellular Chips, among them the first intracellular silicon-based NanoOptoMechanical system, the design, the characterization, the methods to cell internalization and several of the potential ICC applications have been described and discussed. The proofs of concept, methods and applications presented here have contributed to the outbreak of the silicon-based systems for intracellular applications.

These contributions have permitted reach the following main goals:

1. The design and technological development for the fabrication of Dummy Intracellular Chips have been proposed. The performed techniques allow us to obtain Intracellular Chips with controlled features like their shapes and dimensions at intracellular scale. The fabrication technology at wafer level enables the manufacture of millions of devices per 100 mm-diameter silicon wafers. In addition, the method based on the use of HF vapors for the release of the MEMS structures out of the wafer was optimized and adapted to allow an easy and safe procedure. Finally, an efficient collection process, which allowed an easy handling of a high quantity of the Intracellular Chips and their respective storage, was optimized and developed. Biological tests have been also carried out with the objective of demonstrate the cell internalization process and the non-toxicity of the Intracellular Chips in Human Macrophages.

2. Intracellular polySilicon Barcodes for single cell labeling have been also proposed. These devices were designed and fabricated as labels for biology applications. The fabrication process

was optimized to obtain two types of microbarcodes. The fabrication process of the 2D polySilicon Barcodes enables the manufacture of hundreds of different barcodes with different binary codes with only one photolithography and etching step. And the fabrication process of the 3D Silicon Barcodes enables the manufacture of hundreds of identical codes with one photolithography step. However, several etching steps were applied, depending on the binary code that will represent the barcode. Biological studies have been also carried out with the purpose of demonstrate the successful internalization process, the non-toxicity effects and the correct barcode identification.

3. Biomolecular recognition approach through Intracellular polySilicon Chips was demonstrated. Intracellular Chips were designed and fabricated based on the previous successful technological processes. The internalization of Intracellular Chips by living eukaryotic cells, without interfering their cell viability was studied. In addition, the chip surface was also chemically functionalized to validate the use of these devices as intracellular biochemical sensors. Finally, the flexibility and versatility of the polySilicon Chips, through the nano-structuring in three dimensions and the integration of several materials inside the chips fabrication process, was also envisaged.

4. NanoOptoMechanical systems have been successfully designed and fabricated. Taking advantages of the polySilicon technology, a nanomechanical chip that can be internalized to detect intracellular pressure changes within living cells, was devised. First, a system with two membranes separated by a vacuum gap (constituting a Fabry-Pérot resonator) and an optical reference area was design. Second, an interrogation method based on confocal laser scanning microscopy (CLSM) was enabled. NanoMechanical devices were manufactured because of ability of growing non-porous, as thin as possible, layers of polysilicon. In addition, these

devices can be collected and suspended for their posterior use on cell cultures. The NanoOptoMechamical devices were also validated through bright-field and CLSM optical microscope techniques. Cell viability and chip internalization assays have been performed in *HeLa* cells and not revealed cell-toxicity. Analytical and simulated analyses showed that mechanical deformation was highly dependent on the membrane thickness. In addition, the specific localization of the chip inside the cell cytoplasm or into subcellular compartments like vacuoles, not affecting cell fitness or viability, was achieved by optical light or CLMS microscopy. Additionally, cellular division and mitochondria activity, in cells with and without devices, was founded. Overlaid images of transmitted light and laser channels confirmed the capability of these devices of detecting pressure fluctuations inside a cell. By using these devices we confirmed that the extracellular pressure is transmitted to inside the cytosol in *HeLa* cells. In addition, we also directly proved that HeLa cells do not increase the intracellular pressure under an osmotic shock.

The work reported in this thesis has been the basis for a world-wide pioneering research line focused on INTRACELLULAR CHIPS.

Future work

All this work and the mentioned contributions have opened a very successful and fruitful research field at the MICRO- AND NANOTOOLS group at CNM-IMB (CSIC). This thesis represents the first steps of this field, which we are just starting to envisage. Some of the future lines for the development of even more sophisticated Intracellular Chips are focused on the technology development (reducing the size of the minimum features, reducing thickness and roughness of deposited layers, optimization of the release and collection procedures, integrate other materials commonly used on MEMS), on the design (development of new designs for the applications reported in this thesis but also for new applications, many of them supported by FEM simulations), on the characterization techniques and on the sensing principles (for instance, improving the detection systems for the intracellular pressure sensor), and on the application side of the Intracellular Chips by using all the potential applications covered by MEMS.

Appendices

Appendix A: Scientific publications

List of publications related to the work

1. Sergi Novo, Inma Mora-Espí, **<u>Rodrigo Gómez-Martínez</u>**, Leonardo Barrios, Elena Ibañez, Xavier Such, Marta Duch, Xavier Mora, José Antonio Plaza, Carme Nogués. *Traceability of human sperm samples by direct tagging with polysilicon microbarcodes*. Reproductive Biomedicine Online, 31, 2, 162 (2015). DOI: 10.1016 j.rbmo.2015.04.012.

2. Sara Durán, Sergi Novo, Marta Duch, **<u>Rodrigo Gómez-Martínez</u>**, Marta Fernández-Regúlez, Álvaro San Paulo, Carme Nogués, Jaume Esteve, Elena Ibañez, José Antonio Plaza. *Silicon-nanowire based attachment of silicon chips for mouse embryo labeling*. Lab on a Chip, 15, 1508 (2015). DOI: 10.1039/C4LC01299B

3. Sara Durán, Marta Duch, Tània Patio, Alicia Torres, Oriol Penon, **<u>Rodrigo Gómez-Martínez</u>**, Leonardo Barrios, Jaume Esteve, Carme Nogués, Lluïsa Pérez-García, José Antonio Plaza. *Technological development of intracellular polysilicon-chromium-gold chips for orthogonal chemical functionalization*. Sensors and Actuators B: Chemical, 209, 212 (2015). DOI: 10.1016/j.snb.2014.11.077

4. Sergi Novo, Carme Nogués, Oriol Penon, Leonardo Barrios, Josep Santaló, **<u>Rodrigo Gómez-Martínez</u>**, Jaume Esteve, Abdelhamid Errachid, José Antonio Plaza, Lluïsa Pérez-García, Elena Ibañez. *Barcode tagging of human oocytes and embryos to prevent mixups in assisted reproduction technologies*. Human Reproduction, 29, 1, 18 (2014). DOI: 10.1093/humrep/det409.

5. **<u>Rodrigo Gómez-Martínez</u>**, Alberto M. Hernández-Pinto, Marta Duch, Patricia Vázquez; Kirill Zinoviev, Enrique J. de la Rosa, Jaume Esteve, Teresa Suarez, José Antonio Plaza. *Silicon chips detect intracellular pressure changes in living cells*. Nature Nanotechnology, 8, 517 (2013). DOI: 10.1038/nnano.2013.118.

6. Sergi Novo, Oriol Penon, Leonardo Barrios, Carme Nogués, Josep Santaló, Sara Durán, **<u>Rodrigo Gómez-Martínez</u>**, Jaume Esteve, Josep Samitier, José Antonio Plaza, Lluïsa Pérez-García, Elena Ibañez. *Direct embryo tagging and identification system by attachment of biofunctionalized polysilicon barcodes to the zona pellucida of mouse embryos*. Human Reproduction, 28, 6, 1519 (2013). DOI: 10.1093/humrep/det083

7. Sergi Novo, Roser Morató, Oriol Penon, Sara Durán, Leonardo Barrios, Carme Nogués, **<u>Rodrigo Gómez-Martínez</u>**, Lluïsa Pérez-García, José Antonio Plaza, Elena Ibañez, Teresa Mogas. *Zona pellucida tagging with barcodes allows the traceability of bovine embryos cultured in group*. Reproduction fertility and development, 25, 1, 218 (2012)

8. **<u>Rodrigo Gómez-Martínez</u>**, Ana Sánchez, Marta Duch, José Antonio Plaza. *DRIE based technology for 3D silicon barcodes fabrication*. Sensor and Actuators B, 1, 1, 800 (2011). DOI: 10.1016/j.snb.2009.11.008

9. Elisabet Fernández- Rosas, Antoni Baldi, Elena Ibañez, Leonardo Barrios, Sergi Novo, Jaume Esteve, José Antonio Plaza, Marta Duch, **<u>Rodrigo Gómez-Martínez</u>**, Onofre Castell, Carme Nogués, César Fernández-Sánchez. *Chemical functionalization of polysilicon microparticles for single cell studies*. Langmuir, 27, 8302 (2011). DOI: 10.1021/1a200857x (2011).

10. Sergi Novo, Leonardo Barrios, Josep Santaló, **<u>Rodrigo Gómez-Martínez</u>**, Marta Duch, Jaume Esteve, José Antonio Plaza, Carme Nogués, Elena Ibánez. *A novel embryo identification system by direct tagging of mouse embryos using silicon-based barcodes*. Human Reproduction, 26, 1, 96 (2011). DOI: 10.1093/humrep/deq309

11. Elisabet Fernández-Rosas, **<u>Rodrigo Gómez-Martínez</u>**, Elena Ibañez, Leonardo Barrios, Marta Duch, Jaume Esteve, José Antonio Plaza, Carme Nogués. *Internalization and cytotoxicity analysis of silicon-based microparticles in macrophages and embryos.* Biomedical Microdevices, 12, 3, 371 (2010). DOI: 10.1007/s10544-009-9393-6.

12. **<u>Rodrigo Gómez-Martínez</u>**, Patricia Vázquez, Marta Duch, Alejandro Muriano, Daniel Pinacho, Nuria Sanvicens, Francisco Sánchez-Baeza, Patricia Boya, Enrique J. de la Rosa, Jaume Esteve, Teresa Suarez, José Antonio Plaza. *Intracellular silicon chips in living cells.* Small, 6, 4, 499 (2010). DOI: 10.1002/smll.200901041

13. Elisabet Fernández-Rosas, **<u>Rodrigo Gómez-Martínez</u>**, Elena Ibáñez, Leonardo Barrios, Marta Duch, Jaume Esteve, Carme Nogués, José Antonio Plaza, *Intracellular polysilicon barcodes for cell tracking*. Small, 5, 21, 2433 (2009). DOI: 10.1002/smll.200900733

14. **<u>Rodrigo Gómez-Martínez</u>**, Marta Duch, Ana Sanchez, José Antonio Plaza, J. Esteve. *Silicon based devices for intracellular applications*. IFMBE Proceedings, 25, 8, 365 (2009)

Appendix B: Frame of the work

Financial Support

This PhD thesis was financed by the Spanish Government through several national projects. The initial exploratory work was done in the frame of a 1-year Intramural (CSIC) project (INTRACELL). Next, this work was included in the frame of several consecutive projects (MINAHE 2, MINAHE 3, MINAHE 4 and MINAHE 5). The work related to the intracellular pressure sensor was funded by an EXPLORA project (ICCPRESS).

The involved projects were:

INTRACELL: Micro-/Nano-objects for the monitoring of intracellular parameters in living cells. 2005-2007. Reference: 200550F0241. Intramural, Consejo Superior de Investigaciones Científicas (CSIC). COORDINATOR: Prof. Jaume Esteve.

MINAHE 2: Micro/NanoHerramientas para el estudio de células vivas. 2006-2008. Reference: TEC2005-07996-C02-01. Ministerio de Ciencia e Innovación. COORDINATOR: Dr. José Antonio Plaza.

MINAHE 3: Micronanotools for the study, tag and actuation on living cells. 2009-2011. Reference: TEC2008-06883-C03-01. Ministerio de Ciencia e Innovación. COORDINATOR: Dr. José Antonio Plaza.

ICCPRESS: Is it possible to fabricate a mechanical nanosensor to measure intracellular pressure? 2010-2010. Reference: TEC2009-07687-E. Ministerio de Ciencia e Innovación. COORDINATOR: Dr. José Antonio Plaza.

MINAHE 4: MicroNanoTools for Life Sciences. 2012-2014. Reference: TEC2011-29140-C03-01. Ministerio de Ciencia e Innovación. COORDINATOR: Dr. José Antonio Plaza.

MINAHE 5: Micro- y NanoHerramientas en suspensión para aplicaciones en células vivas. Referencia: TEC2014-51940-C2-1-R. Ministerio de Economía y Competitividad. COORDINATOR: Dr. José Antonio Plaza.

Collaborators

These scientific projects were accomplished thanks to the collaboration of the group of Dr. José Antonio Plaza from Instituto de Microelectrónica de Barcelona (IMB-CNM, CSIC) with several multi-disciplinary partners:

1. The group of Dr. Teresa Suarez from 3D LAB Development, differentiation & Degeneration Group, Centro de Investigaciones Biológicas (CIB, CSIC).

2. The group of Dr. Carme Nogués. Departament de Biologia Cel·lular, Fisiologia i Immunologia, Universitat Autònoma de Barcelona (UAB).

3. The group of Lluïsa Pérez. Departament de Farmacologia i Química Terapèutica de la Universitat de Barcelona (UB).

4. The group of Dr. Francisco Sánchez-Baeza. Institute of Research Chemistry & Ambient of Barcelona (IIQAB, CSIC)

Scientific Services

To achieve the proposed objectives inside this doctoral thesis has been necessary to use large scale facilities, such as the Integrated Clean Room for Micro- and Nanofabrication (SB-CNM) located at the IMB-CNM (CSIC) for the chip manufacturing, and several scientific technical services for the chip inspection and measurements outside and inside living cells.

A complete list of the installations and services used during this thesis is shown below:

Chip fabrication

Integrated Clean Room for Micro- and Nanofabrication (SB-CNM) is a Large Scale Facility (ICTS) dedicated to the development and application of innovative technologies in the field of Microelectronics together with other emerging Micro/Nanotechnologies. It is embedded administratively in the Instituto de Microelectrónica de Barcelona, (IMB-CNM), a research centre belonging to the Spanish Council of Scientific Research (CSIC).

Chip characterization inside living cells

Advanced optical microscopy unit: Universitat de Barcelona (UB). Heads of the unit: Dr. Maria Calvo and Dr. Ana Bosch.

Confocal microscopy core unit: Spanish National Cancer Research Centre (CNIO). Head of the unit: Dr. Diego Megies.

Microscopy service unit: Universitat Autònoma de Barcelona (UAB). Head of the unit: Dr. Monica Roldán.

Confocal laser and multidimensional microscopy unit: Centro de Investigaciones Biológicas (CIB, CSIC). Technician of the unit: Mrs. María Teresa Seisdedos.

Confocal microscopes: Leica Microsystems S.L: Contact person: Mr. Juan Monteagudo.

Appendix C: Science Media, News Online and Press

- Petra S. Dittrich, "Microchips-in-a-cell", research Highlights Lab on a Chip, 10, 541-543, 2010.

- Dexter Johnson, "Nanoscale Processing Leads Scientists To Integrate Silicon Chips into Living Cells", IEEE Spectrum site, 22 March, 2010.

- Nanowerk's TOP TEN Spotlight: Future bio-nanotechnology will use computer chips inside living cells, 2010.

- Nanowerk's TOP TEN Spotlight: Silicon chips inserted into living cells can feel the pressure, 2013.

- A. Doerr, Nanobiotechnology: "Cells under pressure", Research Highlights, Nature Methods 10, 818, 2013.

- "The Inside of the scoop", Biomedical picture of the day, 24 August 2013.

- "Cell division of a HeLa cell with a sensor chip inside", Youtube 2013.

Appendix D: Fabry-Pérot interferometer

(A detail explanation about the Fabry-Pérot interferometer is out of scope of this thesis. Therefore, this appendix describes only a short text about its working principle.)

First, the Fabry-Pérot interferometer was described in 1899 by Fabry and Pérot [1]. A Fabry-Pérot interferometer consisted of two perfectly flat glass plates, spaced less than a coherence length apart, thereby forming an optical reflecting cavity. When a beam of light is incident on the outer surface of one of the transparent plates, there are multiple reflections at the plate surfaces [2]. At each reflections, however, a small fraction (1/10 or less) of incident beam escaped through the outer surface of the second plate. With the result, that a series of beams of diminishing amplitude, emerges on each side of the plate. The constructive interference of these many parallel beams of light produce very bright and remarkably sharp interference fringes [3]. If one of the partial reflecting transparent plates is a pressure-sensitive diaphragm, changes in external pressure will alter optical cavity depth. A change in optical cavity depth will cause a change in optical cavity reflectance, causing changes in the interference fringes.
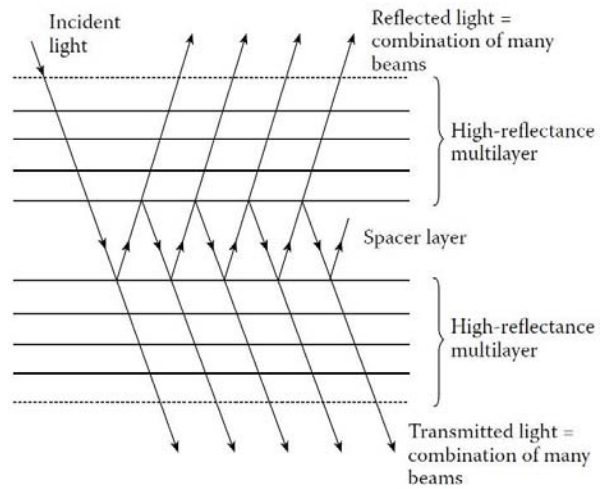
Figure C.1: A Fabry-Pérot filter. a) A Fabry-Pérot filter showing multiple reflections in

the spacer or cavity layer. b) Fabry-Pérot fringes.

Bibliography

[1] C. Fabry, A. Pérot. Theorie et applications d'une nouvelle méthod de spectroscopie interfrentielle Annales des Chimie et des Physique, Paris, 7th Series 16 115144 (1899)

[2] H. A. Macleod. Thin-Film Optical Filters. Ed. CRC Press (2010)

[3] M. Born E. Wolf. Principles of optics Ed. Cambridge U.P. (1999)

Appendix E: Reticulated Coverslip

A micro-patterned cover slip (MPCS) was design with an alphanumerical codification of defined areas, to facilitate the location of the cells and to provide a rapid and unmistakable notation for every cell analyzed.

To produce the MPCS for cell location, one photolithographic process was used in standard clean room conditions. Basically, Al (500 nm-thick) marks were deposited and patterned through HiPR-6512 positive photo resist, on a 500 mm thick Pyrex wafer (7740, Corning Inc.) to defined the different thick square marks using chemical etching process. The device was later passivated through the chemical vapor deposition (CVD) of a standard SiO_2 - Si_3N_4 (400 nm + 700 nm) passivation layer. Once the fabrication process was finished, individual MPCS were cut from the wafer using a standard microelectronic saw. The completed MPCS (9 x 9 mm) include square marks inside of 8 x 8 mm, with repeating units of small squares, which have dimensions of 1 x 1 mm. These small squares are arranged in 8 columns and 8 rows within the 8 x 8 mm mark (Figure D.1). Each row of small squares is labeled from A to H, and each column is labeled form 1 to 8 (top-left corner). Within each small square, cross marks are also patterned 0.25 mm apart, allowing 16 new sub-areas (Figure D.2). Each Al separation line pattern has 5 μm of wide. This fabrication process allows producing in each Pyrex wafer 80 different MPCS, (Figure D.3).

To record the positions, the inset in the grid alphanumerically defined (A1 to I8) is written at the beginning, and the sub-areas defined by the cross marks (a01-a16) are written later.
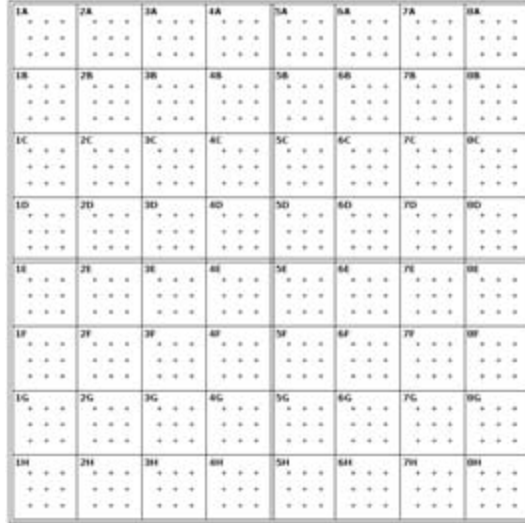
Figure D.1: Schematic of a micro-patterned cover slip. Design of micro-patterned cover slip, with an alphanumerical codification, and defined areas, to facilitate the location of the cells.
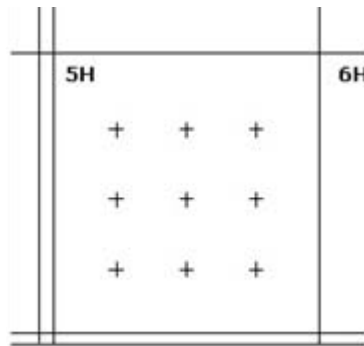
Figure D.2: Schematic of a sub - micro-patterned cover slip. Design of micro-patterned cover slip, with cross marks are also patterned 0.25 mm apart, allowing 16 new sub-areas.
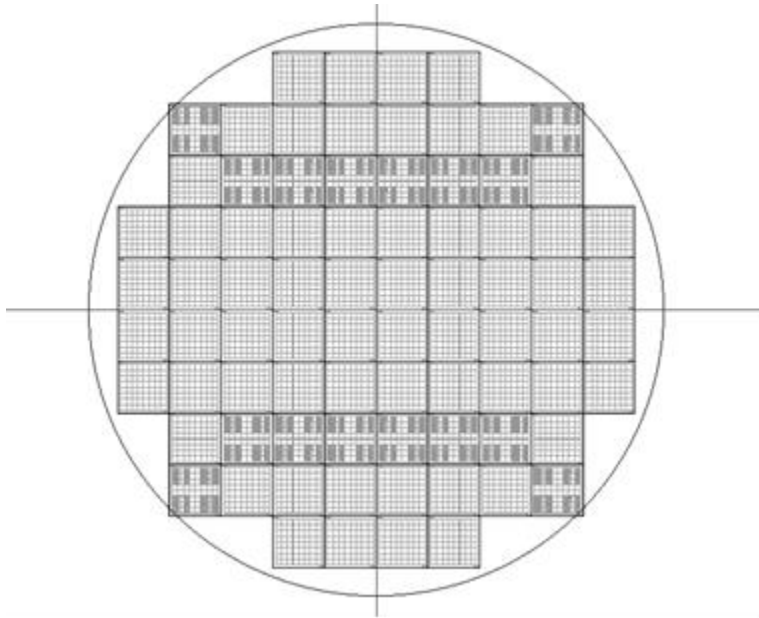
Figure D.3: Schematic of a MPCS wafer distribution. Design of MPCS masks wafer distribution.

Appendix F: List of Figures

Appendix G: List of tables and equations

Tables

Equations

Appendix H: Scientific publications of the author out of the scope of the thesis

List of publications of the author out of the scope of the thesis

1. Eva Baldrich, **Rodrigo Gómez**, Gemma Gabriel, Francesc Xavier Muñoz. *Magnetic Entrapment for Fast, Simple and Reversible Electrode Modification with Carbon Nanotubes. Application to Dopamine Detection*. Biosensors and Bioelectronics, 26, 5, 1876 (2011). DOI:10.1016/j.bios.2010.03.020.

2. Philippe Godignon, Inigo. Martin, Gemma Gabriel, **Rodrigo Gómez**, Marcel Placidi, Rosa Villa. *New generation of SiC based biodevices implemented on 4 wafers*. Materials Science, 645-648, 1097 (2010). DOI:10.4028/www.scientific.net/MSF.645-648.1097.

3. Gemma Gabriel, **Rodrigo Gómez**, Markus Bongard, Nuria Benito, Eduardo Fernández, Rosa Villa. *Easily made single-walled carbon nanotubes surface microelectrodes for neural application*. Bionsensors and Bioelectronics, 24, 1942 (2009). DOI: 10.1016/j.bios.2008.09.036.

4. Gemma Gabriel, **Rodrigo Gómez-Martínez**, Rosa Villa. *Single-walled carbon nanotubes deposited on surface electrodes to improve interface impedance*. Physiologycal Measurements, 29, S203 (2008). DOI: 10.1088/0967-3334/29/6/S18.

5. Gemma Gabriel, Ivan Erill, Jaume Caro, **Rodrigo Gómez**, Dolors Riera, Rosa Villa, Philippe Godignon, *Manufacturing and full characterization of silicon carbide-based multi-sensor micro-probes for biomedical applications*. Microelectronics Journal, 38, 3 (2007). DOI: 10.1016/j.mejo.2006.11.008.

6. Gemma Gabriel, **Rodrigo Gómez-Martínez**, Rosa Villa. *Interface impendance improvements with carbon naotubes*. ICEBI, IFMBE Proccedings, 17, 296 (2007). ISBN: 978-3-540-73840-4.

7. Rodrigo Gómez, Antoni Ivorra, Rosa Villa, Philippe Godignon, José Millán, Ivan Erill, Anna Sola, Georgina Hotter, Luís Palacios. *A SiC microdevice for the minimally invasive monitoring of ischemia in living tissues*. Biomedical Microdevices, 8, 1, 43 (2006). DOI: 10.1007/s10544-006-6381-y.

8. Ana Sola, Luis Palacios, Jose López Martí, Antoni Ivorra, **Rodrigo Gómez**, Nuria Noguera, Rosa Villa Jordi Aguiló, Georgina Hotter. *Multiparametric monitoring of ischemia/reperfusion in rat kidney:effect of ischemic preconditioning*. Transplantation, 75, 6, 744 (2003). DOI: 10.1097/01.TP.0000054683.72223.2D.

9. Antoni Ivorra, **Rodrigo Gómez**, Nuria Noguera, Rosa Villa, Ana Sola, Luis Palacios, Georgina Hotter, Jordi Aguiló. *Minimally invasive silicon probe for electrical impedance measurements in small animals.* Biosensors and Bioelectronics, 19, 4, 391 (2003). DOI: 10.1016/S0956-5663(03)00204-5.

10. Rodrigo Gómez, Nuria Noguera. Antoni Ivorra, Rosa Villa, Jordi Aguiló, Jose Millán, Jose López, Luis Palacios, Ana Sola, Georgina Hotter. *Instrumentation system for in vivo organ studies*. IEEE International Symposium on Semiconductor Manufacturing Conference, 1, 261 (2001).